Topics on Hadron Collider Physics

Topics on Hadron Collider Physics

A dissertation presented
by

Dilani S Kahawala

to
The Department of Physics
in partial fulfillment of the requirements
for the degree of
Doctor of Philosophy
in the subject of

Physics

Harvard University
Cambridge, Massachusetts
March 2013

Thesis advisor

Lisa Randall

Author

Dilani S Kahawala

Topics on Hadron Collider Physics

Abstract

In this dissertation we present four techniques that could be used at the Large Hadron Collider (LHC) to improve the efficiency with which collected data is utilized, and to help detect signals of physics beyond the Standard Model. We present an extension of the Qjets algorithm which allows us to exploit the different possibilities for reconstructing an event at the LHC to produce multiple interpretations for each event. For example, using this approach on a Higgs plus Z boson sample, with $h \to bb$ we find a 28% improvement in significance can be realized at the 8 TeV LHC. We also propose a measurement of the bottom quark forward-central asymmetry at the LHC in order to gain further insight into the Tevatron $t\bar{t}$ anomaly. Using a toy axigluon model we find that if the relevant new-physics couplings to the bottom quark are similar to those of the top, then the effects should be visible at the 2σ level in less than 10 fb^{-1} of 7 TeV LHC data. Finally we develop two techniques to measure fundamental quantum numbers of new particles at the LHC, with the goal of distinguishing between different theories beyond the Standard Model. In the first case we consider long lived colored particles and in the second case we consider bound states of new colored particles which annihilate into Standard Model particles.

Contents

Citations to Previously Published Work

Chapter 2 has been published as

> "Jet Sampling: Improving Event Reconstruction through Multiple Interpretations", Dilani Kahawala, David Krohn and Matthew D. Schwartz, `arXiv:1304.2394 [hep-ph]`.

Chapter 3 has been published as

> "Measuring the Bottom-Quark Forward-Central Asymmetry at the LHC", Dilani Kahawala, David Krohn and Matthew J. Strassler, JHEP **1201**, 069 (2012), `arXiv:1108.3301 [hep-ph]`.

Chapter 4 has been published as

> "Stable Colored Particles R-SUSY Relics or Not?", Matthew R. Buckley, Bertrand Echenard, Dilani Kahawala, and Lisa Randall, JHEP **1101**, 013 (2011), `arXiv:1008.2756 [hep-ph]`.

Finally, Chapter 5 has been published as

> "Distinguishing spins at the LHC using bound state signals", Dilani Kahawala and Yevgeny Kats, JHEP **1109**, 099 (2011), `arXiv:1103.3503 [hep-ph]`.

Excerpts from the papers above also appear in Chapter 1. Electronic preprints (shown in `typewriter font`) are available on the Internet at the following URL:

> `http://arXiv.org`

Acknowledgments

I feel incredibly privileged to have had the opportunity to work with and be mentored by my doctoral advisor Lisa Randall. Lisa guided me through my first research publication and taught me the importance of asking the right questions. She is always full of creative ideas and has a deep intuition about the field, which allows her to see where a certain idea could lead. I continue to be inspired by her brilliance and passion as a physicist, and her talent for sharing physics with the world.

I would like to thank Howard Georgi for his continuous support and guidance throughout my PhD. Howard gave me my first taste of research and much good advice. He was always generous with his time, always willing to share his incredible wealth of knowledge and patient with questions. I appreciated his ability to explain things in many different ways until I finally understood.

Matthew Schwartz taught me almost everything I know how to calculate. Even though at the time it seemed unbearably painful to calculate so many box diagrams, it certainly paid dividends when I started research. Matt always pushed for a more intuitive understanding of the underlying physics beyond equations, and this helped deepen my own understanding as we worked on our Qjets paper.

I would like to thank John Huth for providing valuable experimental insights on numerous occasions, both directly on my research and also during joint experiment-theory lunches.

Thank you to Melissa Franklin who always had time to listen and gave me practical advice over the past five years.

Thank you to the ever so wise David Krohn. David has been an amazing collaborator, good friend and mentor for the past couple of years and I benefited enormously from his experience and knowledge of collider physics. I could always ask David even the stupidest

of questions without feeling so, and often did! He showed me how not to reinvent the wheel and was always happy to help me debug code at 4am over Gchat.

I was financially supported throughout my PhD by the General Sir John Monash Fellowship. Thank you to Peter Binks who over the years took a keen interest in my progress, helped connect me with other incredible Australians, and provided valuable support and guidance as I thought about my next steps. The fellowship gave me the freedom to pursue the areas of physics that really interested me and gave me the opportunity to collaborate with many different physicists.

I am especially grateful to my other collaborators Yevgeny Kats, Matt Buckley, Matt Strassler and Bertrand Echenard. I would also like to thank my colleagues Brian Shuve, Risa Kawai, Yang-Ting Chien, Greg Kestin, Irene Bredberg, Suzanne Pittman, Ashwin Rastogi, and Ilya Feige for their support and good times. Thanks to Sheila Ferguson, Carol Davis, Nancy Partridge and Bill Walker for listening and helping everything go smoothly.

Without the support of my amazing parents and loving brother, I would not have made it this far. They helped me dream big, instilled in me the drive to excel and the perseverance to see something through to the end. I am so grateful for their courage and support as I left home and flew across the Pacific to pursue my dreams.

Finally, words cannot express how thankful I am to my husband Hemant for his incredible love and support. I feel so lucky that we were able to journey through graduate school together and take in everything that is amazing about Harvard, MIT and Cambridge. Your kindness, generosity, friendship and laughter made this journey a memorable one.

Dedicated to my best friend and husband Hemant Chaurasia,
to my amazing parents Jayanthi Perera and Piyadasa Kahawalage,
and the best brother ever, Mithun Kahawala.

Chapter 1

Introduction

The Standard Model (SM) of particle physics is a spectacularly successful theory that accurately predicts the interactions between twelve fundamental particles (six quarks and six leptons) and three fundamental forces (strong, weak and electromagnetic). It also includes the Higgs boson, which gives mass to all massive particles. Since its development in the early 1970s, the SM has withstood experimental testing to an extremely high degree of precision and over a wide range of energies. Hadron colliders have played a vital role in discovering many of the particles and phenomena predicted by the SM, from the discovery of W and Z bosons at the Super Proton Synchrotron (SPS) in 1983 to the top quark discovery at the Tevatron in 1995. After many years of anticipation, the Large Hadron Collider (LHC), the highest energy particle collider to date, finally commenced operations in November 2009. Equipped with four detectors ATLAS, CMS, ALICE and LHCb, and designed to be capable of reaching 14 TeV center of mass energy, the LHC promises to usher in a new era of insights and discoveries in particle physics.

Despite its resounding success as a model of particle physics, the SM has a number of

shortcomings which indicate that our understanding of the theory is incomplete. Some of the key problems include: the inability to unify gravity with the other three fundamental forces; the hierarchy between the Planck scale and the TeV scale Higgs mass; the absence of observed charge parity violation in the strong sector known as the strong CP problem; and the lack of a viable dark matter candidate. For a more complete review of the SM and its shortcomings see Ref. [1].

In fact, it was only in 2012 that we saw the first concrete experimental evidence for the existence of the Higgs boson. On July 4, 2012 the ATLAS and CMS [2, 3] collaborations announced that both experiments had seen evidence, exceeding five standard deviations (5σ) of the background prediction, of a new boson with properties akin to that of the SM Higgs boson. A key focus for both collaborations is to further narrow down the properties of this observed particle in order to conclusively say whether it is in fact the plain vanilla SM Higgs boson, or if in fact some new physics might be present.

In addition to searching for the Higgs, many physicists are hopeful that the LHC will also discover evidence of new physics beyond the SM. A number of theories beyond the Standard Model have been developed, the prominent candidates being Supersymmetry and Extra Dimensions, which attempt to assuage the problems with the SM by introducing new particles and interactions at higher energies [4, 5, 6].

The LHC will continue to search for new particles and interactions at higher energies than we have ever been able to attain at previous experiments. The hope is that it will lead to many new discoveries and provide a portal to improve our understanding of the SM. However, in addition to the high center of mass energies the collider is able to attain, as well as the state-of-the-art detectors with unprecedented precision, a hadron collider such

as the LHC faces a unique set of challenges. In particular, colliding protons rather than fundamental particles such as electrons and positrons, means that collisions result in complex event environments. Since it is the partons inside the proton that collide, determining the precise kinematics of each event is more complicated than at an electron-positron collider. In addition there may be interactions of other partons from the colliding protons (underlying event) and contamination from other protons in the bunch (pile-up).

A given event at the LHC can be contaminated by initial state radiation (ISR) from the incoming partons and final state radiation (FSR) where the outgoing partons emit soft and collinear radiation. In many new physics scenarios, new heavy particles will decay to a series of lighter states leading to jets of colored particles. Strongly interacting particles produced in collisions will radiate heavily as they travel through the detector and eventually hadronize. The task of reconstructing the interaction that lead to these final state hadrons is done by jet algorithms, which is non-trivial and often ambiguous. In order to isolate the signal events in such a complex environment, we need to have a thorough understanding of the SM background processes that can mimic signal-like events. In particular, the decay of top and anti-top quark pairs can often falsely appear as a signature of new physics.

In transitioning from the Tevatron era to the LHC era, we need to make some adjustments to the observables we use to look for evidence of new physics. The Tevatron collided protons with anti-protons, while the LHC collides protons with protons. We cannot simply consider LHC processes to be higher energy versions of the Tevatron processes. The initial states for many processes are different in the two colliders. While anti-quarks have a high probability of being found inside anti-protons, they are rare inside protons. While valence quark scattering tended to dominate at the Tevatron, sea quark and gluon scattering will dominate at the

LHC. This further means that observables relying on specific quark and anti-quark directions, such as forward-backward asymmetries at the Tevatron, need to be modified for a parity symmetric collider like the LHC.

If we were to see hints of a new physics signal at the LHC, the next challenge is to identify which theory beyond the SM accurately describes the new observation. There may be an entire class of models that predict similar signals. So it is crucially important to ascertain the properties of any newly observed particle, such as spin and charge under the SM gauge groups as accurately as possible. In order to proclaim the discovery of a new particle or to exclude a suspected signal at 5σ, months if not years of data need to be collected. Therefore, any technique that could improve the efficiency with which we use the data collected, to arrive at the required 5σ level faster, will be of immense benefit.

In this dissertation, we present four papers that develop techniques that could be used at the LHC to address three of the aforementioned issues: to improve the efficiency with which data is used by jet algorithms; to modify and refine observables used at the Tevatron for the LHC; and finally, techniques to help detect and classify signatures of physics beyond the Standard Model.

In Chapter 2 we present an extension of the Qjets algorithm, which was initially applied to jet substructure [7], applied to a whole event. The classification of events involving jets as signal-like or background-like can depend strongly on the jet algorithm used and its parameters. This is partly due to the fact that standard jet algorithms yield a single partition of the particles in an event into jets, even if no particular choice stands out from the others. As an alternative, we propose that one should consider multiple interpretations of each event, generalizing the Qjets procedure to event-level analysis. With multiple interpretations, an

event is no longer restricted to either satisfy cuts or not satisfy them – it can be assigned a weight between 0 and 1 based on how well it satisfies the cuts. These cut-weights can then be used to improve the discrimination power of an analysis or reduce the uncertainty on mass or cross-section measurements. For example, using this approach on a Higgs plus Z boson sample, with $H \to b\bar{b}$ we find an 28% improvement in significance can be realized at the 8 TeV LHC. Through a number of other examples, we show various ways in which having multiple interpretations can be useful on the event level.

In Chapter 3 we propose a measurement of the bottom quark forward-central asymmetry designed to look for hints of new physics in the b-sector at the LHC [8]. Measurements of the top quark forward-backward asymmetry performed at the Tevatron suggest that new-physics may be playing a role in $t\bar{t}$ production. To better understand the source of the asymmetry, recent proposals have called for a measurement of the bottom and charm forward-backward asymmetries at the Tevatron, using jets with embedded muons. Here we propose a corresponding measurement of the bottom quark forward-central asymmetry designed to look for similar effects in the b-sector at ATLAS and CMS. We construct a set of cuts designed to enhance sensitivity to this asymmetry, and test our analysis on a toy axigluon model representative of those used to explain the top asymmetry. We find that if the relevant new-physics couplings to the bottom quark are similar to those of the top, then the effects should be visible at the 2σ level in less than 10 fb^{-1} of 7 TeV LHC data. Such a measurement would be of general importance, and would provide valuable model-building input, serving to restrict the set of models put forward to explain the Tevatron $t\bar{t}$ anomaly. However, a relatively low trigger threshold on non-isolated muons inside hard jets must be maintained to allow for this measurement.

In Chapters 4 and 5 we develop techniques that could be used to distinguish particles from different scenarios beyond the Standard Model at the LHC [9, 10]. They key is to measure the fundamental quantum numbers of the new particles.

In Chapter 4 we focus on long lived colored particles (LLCPs) that the LHC might produce. All such particles would provide a spectacular, if somewhat unusual, signal at ATLAS and CMS. Produced in large numbers and leaving a characteristic signature throughout all layers of the detector, including the muon chamber, they could be straightforward to discover even with low luminosity. Though such LLCPs can be realized in many extensions of the Standard Model, most analyses of their phenomenology have focused only on R-hadrons. In order to distinguish among the possibilities, fundamental quantum numbers of the new states must be measured. In this chapter, we demonstrate how to identify the $SU(3)_C$ charge and spin of such new particles at the LHC.

Finally in Chapter 5 we show how the bound state signals can distinguish between two scenarios that have similar particle content and interactions but different spins, such as the minimal supersymmetric standard model (MSSM) and universal extra dimensions (UED). A pair of new colored particles produced near the threshold can form a bound state and then annihilate into standard model particles. We find, for example, that bound states of KK gluons (KK gluonia) have an order of magnitude larger cross sections than gluinonia and they may be detectable as resonances in the $b\bar{b}$, $t\bar{t}$ or $\gamma\gamma$ channels if the KK gluon is very light and sufficiently long-lived. KK gluonia can be distinguished from gluinonia by their much larger cross sections and distinct angular distributions. Similarly, KK quarkonia can be distinguished from squarkonia by the size of their diphoton cross section and by their dilepton signals. Since many of our results are largely determined by gauge interactions,

they will be useful for many other new physics scenarios as well.

Chapter 2

Improving Event Reconstruction through Multiple Jet Interpretations

2.1 Introduction

Almost every event recorded at the Large Hadron Collider contains some number of jets. Sometimes the jets are the objects of interest, as in a search for dijet resonances. Sometimes they are indications of contamination and a jet veto can be used to increase signal purity. Even in events that are predominantly electroweak some amount of jet activity is usually present. Techniques for analyzing jets, in particular, the substructure of jets, have been increasing in sophistication in recent years. Some recent reviews are [11, 12, 13, 14].

To use jets for any sort of analysis, one first needs a way to translate the hadronic activity in the event into a set of jets. At the LHC, this is done almost universally with sequential recombination algorithms. These algorithms, such as the anti-k_T [15], Cambridge/Aachen [16, 17], and k_T [18, 19] algorithms, assemble jets by merging particles in

a sequence determined by some fixed distance measure. The result of applying such an algorithm to an event is a tree containing a sequence of branchings. The jets resulting from running a jet algorithm represent the algorithm's best guess as to which particles should be associated with the fragmentation of the same hard parton. In this chapter (unlike in [7]) we will only be interested in which particles end up in which jet, not the structure of the clustering tree.

In the majority of cases, such as when there are a few, well-separated jets, the best guess interpretation from any algorithm provides an excellent representation of the event. However, for events with multiple and overlapping jets, the interpretations can differ greatly among algorithms, or even when the parameters (such as the jet size R) of a single algorithm are varied. Ideally, one would like to treat events which are sensitive to the jet algorithm or jet parameters differently from ones which are more robust to algorithmic variations. In this chapter, we propose a way to consider multiple interpretations of an event at once.

Intuitively it makes sense that considering multiple interpretations of an event should yield useful information. Indeed, probabilistic jet algorithms were first discussed long ago in relation to improving the behavior of seeded jet algorithms [20]. Other related approaches to jets include combining observables to improve discovery significance [21, 22, 23], comparing multiple interpretations of jet reconstruction with models of showering in signal and background processes [24, 25], scale-invariant jet tagging [26], and measuring the "fuzziness" of jet reconstruction [27]. Here we consider how multiple interpretations of each event can be used to turn single observables (e.g. dijet invariant mass) into distributions. This idea was proposed in [7] and called Qjets. In [7] a proof-of-concept application of Qjets was given which focused on tree-based jet substructure. It was shown that Qjets can improve

the statistical discriminating power in the search for boosted hadronically decaying objects. In this chapter, we apply the multiple-interpretations aspect of the Qjets approach to jet reconstruction over a full event.

The basic idea behind Qjets is to sample interpretations near what a traditional jet algorithm would give. During a clustering step, a traditional jet algorithm merges the two closest particles based on some distance measure. One possible way to sample interpretations around this standard interpretation is, rather than always merging the two closest particles, to merge two particles with some probability depending on how close they are. The result is a set of N interpretations of each event.

There are a number of ways one can process these N interpretations. In [7], the N trees constructed from the particles in a single jet were pruned [28]. Pruning throws out some particles based on the branching sequence in the tree. Since the pruned trees have different particles for each tree, the jet properties are different. For example, since N different jet masses result one can look at the width of the mass distribution for a single jet. This width, called volatility in [7], was shown to be a useful discriminant between signal and background jets in certain cases.

In this chapter, we apply the multiple interpretations idea of Qjets to an entire event, and we do not apply pruning (or any other grooming procedure). Instead, we exploit the fact that different clusterings will give jets with different 4-vectors. For example, if a particle is halfway between two jets, it might get clustered into each jet half the time. Or a particle which classical anti-k_T clusters with the beam now has some probability to be clustered into a jet. With multiple interpretations, particles can be associated with many different jets, in contrast to classical algorithms where each particle is always associated with exactly one jet.

The result of applying Qjets to an event is a set of N interpretations of that event. One way to process these interpretations is to apply some cuts to them, as one would in a classical analysis. For example, one can impose a dijet mass window cut or a p_T cut. While with a classical algorithm, an event would either pass or not pass the cuts, with Qjets, a fraction z of the interpretations pass. We call z the **cut-weight**. Events with z close to 1 are then very likely to be signal, while events with z close to zero are unlikely to be signal. Although one can try cutting directly on z (similar to cuts on volatility in [7]), it is better to use z to compute a statistical weight for a given event. That is, instead of throwing events out, each event is weighted by how signal-like it appears. Then one simply constructs the distribution of, say, the dijet invariant mass, with each event weighted by its z-value. The statistical fluctuations on this weighted invariant mass will be smaller (often much smaller) than if $z = 0$ or $z = 1$ are the only possibilities considered (as in a classical analysis). We will show that using weighted events in this way can provide significant improvements in the size of a signal divided by the characteristic background uncertainty, $S/\delta B$, for many event classes.

In this chapter we consider 4 processes: 1) $Z + H$ with $H \to b\bar{b}$, 2) a heavy scalar ϕ produced in association with a Z boson with $\phi \to$ dijets, 3) 1 TeV dijet resonance, and 4) a heavy scalar decaying to 2 other scalars which each decay to dijets. In cases where the event topology is simple and unambiguous, for example when there are two well separated jets, we find that standard algorithms perform quite well and the use of multiple interpretations only provides a marginal improvement. However, in more complex cases where events have jets with potentially overlapping boundaries, using the multiple interpretations can substantially improve significance over standard cut-based analyses. As an important example, we find a 28% improvement in $S/\delta B$ for $Z + H$ over its $Z + b\bar{b}$ irreducible background.

This chapter is structured as follows. In Sec. 2.2 we will present a modification of the anti-k_T algorithm to make it non-deterministic. Modifying the jet algorithm in this way generates a Monte-Carlo sampling of the distribution of interpretations around the best-guess interpretation. Some ways to visualize the effect of multiple interpretations are presented in Sec. 2.3 and 2.4. In Sec. 2.5 we derive a formula for the statistical significance using our method. Sec. 2.6 applies the algorithm to several samples of phenomenological interest. Some comments on the speed of the algorithm are given in Sec. 2.7. Conclusions are in Sec. 2.8.

2.2 Qanti-k_T: a non-deterministic anti-k_T algorithm

We begin by describing how the anti-k_T algorithm can be modified to provide multiple interpretations of an event. While one would ideally sample every possible reconstruction of an event, collider events typically contain a large number of final state particles so this is impractical. Instead we generate a representative sample of interpretations by using a Monte-Carlo integration type approach. A fastjet plugin with and implementation of this Qanti-k_T algorithm is available at http://jets.physics.harvard.edu/Qantikt.

The Qanti-k_T algorithm works as follows. The input is a set of 4-vectors representing each particle's 4-momenta. These can be the stable hadrons in an event, charged tracks coming from a primary interaction, calorimeter cells, topoclusters, or the output of a Monte Carlo.

1. First calculate the distances d_{ij} between each pair of 4-vectors and also the distances d_{iB} between each 4-vector and the beam. The metric used for the distance calculation

is that of anti-k_T, although the procedure can easily be modified to work with C/A or k_T. The anti-k_T distance measure is

$$d_{ij} = \min\left(p_{Ti}^{-2}, p_{Tj}^{-2}\right) \frac{\Delta R_{ij}^2}{R^2}, \tag{2.1}$$

and

$$d_{iB} = p_{Ti}^{-2}, \tag{2.2}$$

where $\Delta R_{ij} = \sqrt{(y_i - y_j)^2 + (\phi_i - \phi_j)^2}$ is the angular distance between a pair of 4-momenta i and j with y the rapidity and ϕ the azimuthal angle. R is a free parameter in the anti-k_T algorithm, representing the size of the final jets one is interested in.

2. A weight is then assigned to each pair:

$$\omega_{ij}^{(\alpha)} = \exp\left\{-\alpha \frac{(d_{ij} - d^{\min})}{d^{\min}}\right\}, \tag{2.3}$$

where $d^{\min}$ is the minimum distance over all pairs at this stage of the clustering and α is a real number called **rigidity** in [7].

3. A random number is used to choose a pair to merge. The probability of merging a given pair is

$$P_{ij}^{(\alpha)} = \frac{\omega_{ij}}{\sum_{i,j} \omega_{ij}} \tag{2.4}$$

4. Repeat until all particles have been merged into jets or a beam.

At its heart, the Qanti-k_T algorithm is still a sequential recombination algorithm. However, the weights and their Monte-Carlo sampling modify the order of the merging and change

which particles get clustered into each jet or the beam on each iteration. In a traditional sequential recombination algorithm the jets closest in distance are merged first. In Qanti-k_T, jet-jet or jet-beam distance is assigned a weight, controlled by a parameter α, which allows the recombination order to vary. For a given event we find it is typically sufficient to repeat the Qanti-k_T procedure a few tens of times at the same value of α for our results to stabilize[1]. The result can be thought of as a Monte-Carlo calculation of the distribution of interpretations around a best guess.

When $\alpha = 0$, all distances are given equal weighting, which means that particles far apart could be merged into the same jet early in the clustering. Somewhat surprisingly, despite the random clustering, in [7] it was found that Qanti-k_T can still distinguish signal from background even when $\alpha = 0$, although that will not be the case here. As α increases in value clusterings closer to those of anti-k_T have higher weights and are consequently more likely to be realized. One can think of α somewhat like $\frac{1}{\hbar}$. In analogy with with the $\hbar \to 0$ limit of quantum mechanics we term the $\alpha \to \infty$ limit the *classical limit*. In the classical limit the pair of particles closest in distance is always merged and the diversity of interpretations is lost.

In addition to α, the jet radius parameter R can also be varied. For finite α the final jets are no longer circles of radius R as they are in classical anti-k_T. Indeed, with Qanti-k_T, there is no longer even a precise notion of where the jets are. This can be seen in Fig. 2.1 below. As a result, there is less sensitivity to the precise choice of R when using Qanti-k_T than when using classical algorithms. This speaks to the general trends observed in [7]: with Qjets results depend much more weakly on the jet algorithm and algorithm parameters than

[1]In this chapter we will always run Qanti-k_T $N = 100$ times per event.

with classical jets.

It is worth pointing out that the Qanti-k_T algorithm is infrared and collinear (IRC) safe. IRC safety means that when an arbitrarily soft particle is added or a particle is split into two particles in the same direction, the results are unchanged. Qanti-k_T is IRC safe as long as $\alpha > 0$. To see this, first note that all sequential recombination algorithms are by their nature infrared safe – any infinitesimally soft emission will simply be clustered with harder radiation during the recombination process and will thus have no effect on the final outcome. For collinear splittings, one might worry that when non-determinism is added to the clustering, if a particle is split in two, the two halves might be clustered differently. However, note that $d_{ij} \propto (\Delta R)^2$ (see Eq. 2.1), and therefore d_{ij} between two particles which are exactly collinear will be exactly zero. When this happens, $d^{\min} = 0$ as well and so, for $\alpha > 0$, $P_{ij}^{\alpha} = 1$ for collinear particles and $P_{ij}^{\alpha} = 0$ otherwise. Thus, collinear particles will always be clustered before non-collinear ones, and collinear particles will always end up in the same jet.

2.3 Overlapping jets and jet area

Before applying Qanti-k_T to a signal/background discrimination task, we can explore how it differs from classical algorithms. An advantage of Qanti-k_T is that particles are not always clustered into the same jets. This is particularly useful in contexts where jets overlap. With overlapping jets, classical algorithms must assign each particle to exactly one jet. But Qanti-k_T can split the particles into each jet some fraction of the time.[2]

[2]A note on our sample composition: we generate our signal and background events using a combination of Madgraph v5.7 [29] and Pythia v6.4 [30]. All events were generated assuming a 8 TeV LHC. We group the visible output of Pythia into massless $\delta\eta \times \delta\phi = 0.1 \times 0.1$ massless cells with $|\eta| < 5$. Each type of

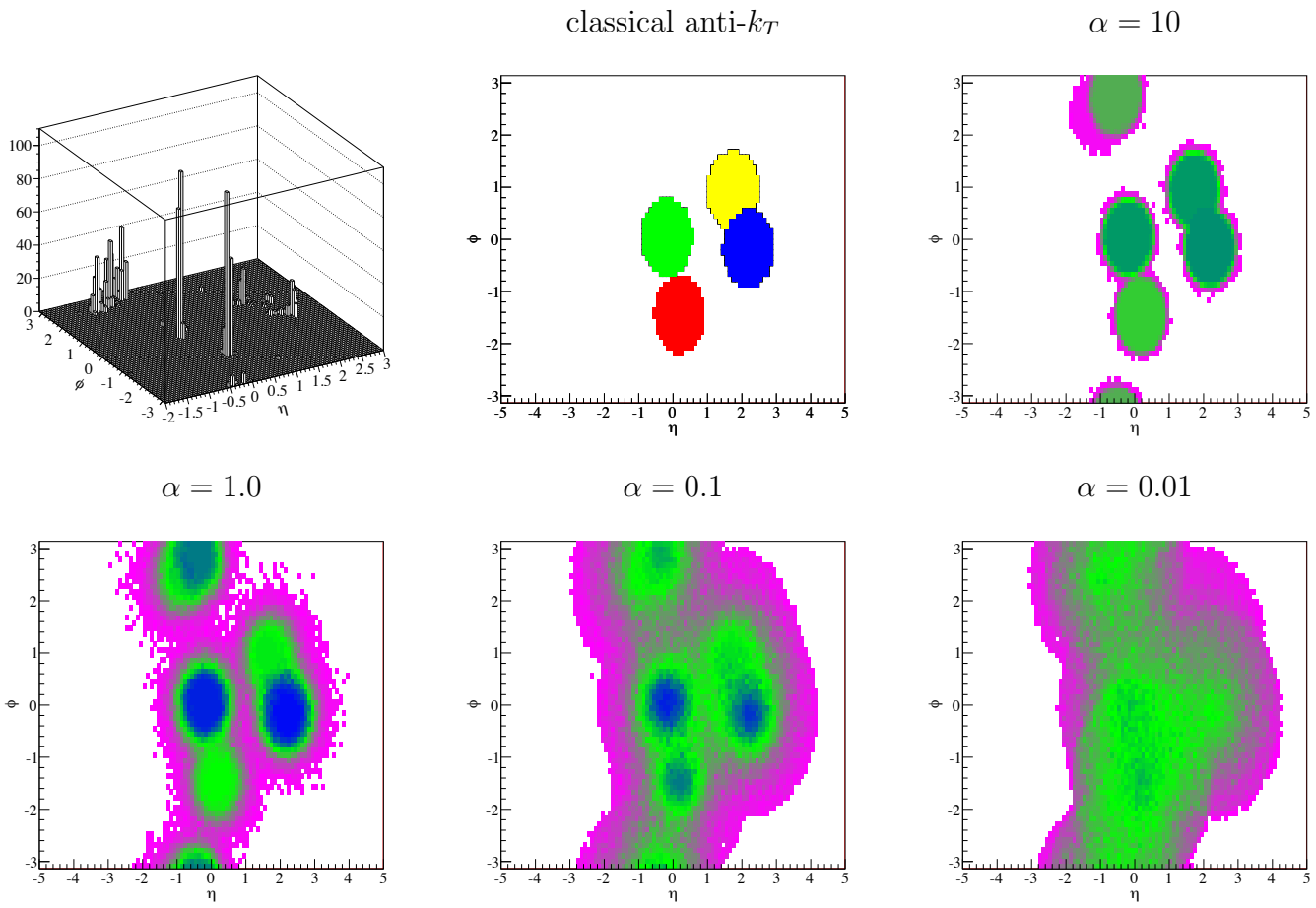

Figure 2.1: The top-left panel shows the $\eta \times \phi$ plot of a simulated $pp \to \phi\phi \to gggg$ event at the LHC, with $m_\phi = 500$ GeV. The top middle panel shows the jet areas associated with the four jets which best reconstruct the event using the classical anti-k_T algorithm (see Sec. 2.6.4). The colors show the detector elements where zero-energy ghost particles would get clustered into each jet. The remaining plots show the frequency with which a cell is clustered into one of the four jets which best reconstruct each event for different choices of α. Blue squares indicate a cell is nearly always included amongst the four hardest jets, green squares indicate that the cell is included roughly half the time, while pink indicates a cell is only rarely included. The same event is shown in all plots.

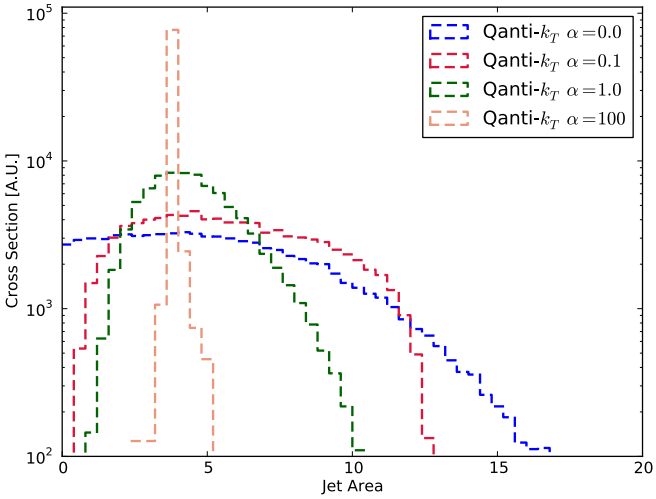

Figure 2.2: The jet area computed using Qanti-k_T for various choices of the rigidity parameter α. Shown is the area of the hardest jet in $\phi \to gg$ dijet events with $m_\phi = 1$ TeV using $R = 1.1$.

To see how Qanti-k_T handles overlapping jets, consider the four-jet event shown in Fig. 2.1. This event is $pp \to \phi\phi \to gggg$ at the parton level, a process examined in Sec. 2.6.4. In order to demonstrate that particles between jets can get clustered into different jets, we show what happens when ghost particles are added to the event. Ghost particles were introduced in [32] as a way to characterize the area of a detector to which a jet is sensitive. Ghost particles are zero energy particles scattered throughout the acceptance region. Since they have zero energy, they do not affect the location or 4-momentum of the final jets. The top-middle panel of 2.1 shows the areas associated with the four jets which best reconstruct the event using classical anti-k_T (see Sec. 2.6.4). This panel is similar to the bottom right panel of Fig. 1 of [15].

The remaining panels in Fig. 2.1 show the frequency with which individual cells are

event is analyzed with both Qanti-k_T and also standard anti-k_T for comparison. We use Fastjet v2.4.2 [31] to generate the standard anti-k_T results.

clustered into the four jets which best reconstruct the event using Qjets for various α. We see that for small values of α there is little well defined structure to the event, while for $\alpha = 0.1$ we begin to see jetty areas of activity with amorphous borders. Finally, for larger value of α we begin to resolve the standard anti-k_T circular jet shapes. Note in particular from the $\alpha = 10$ panel that there are five jets relevant in this event – there is no clear choice between which four should be used in the reconstruction. This is precisely the sort of ambiguity which the multiple-interpretations approach can efficiently exploit.

One can be more quantitative about the area clustered into each jet using the jet area proposed in [32]. In a classical algorithm, this is the area of the detector clustered into a given jet. With Qjets, the area varies for each clustering. Thus the jet area becomes a distribution. This distribution is shown in Fig. 2.2, averaged over many events for $R = 1.1$. Jet area using the classical anti-k_T algorithm would give a δ-function at area $= \pi R^2 = 3.8$. One can see this being approached at large α. For $\alpha = 1.0, 0.1$ or 0, the area is much broader. Thus, with Qanti-k_T, the jet area can be either larger or smaller than what comes from using classical anti-k_T.

2.4 Cut-weights

Once one generates N clusterings of each event using Qanti-k_T, the clusterings can be used to improve the statistical significance in an analysis. In the context of a search, combining multiple interpretations can be used to improve the $S/\delta B$ (the signal size divided by the characteristic background uncertainty) compared to a standard jet algorithm. Alternatively, the uncertainty on a mass, cross section, or branching ratio measurement from a given sample can be reduced. In this chapter, we focus on improving $S/\delta B$.

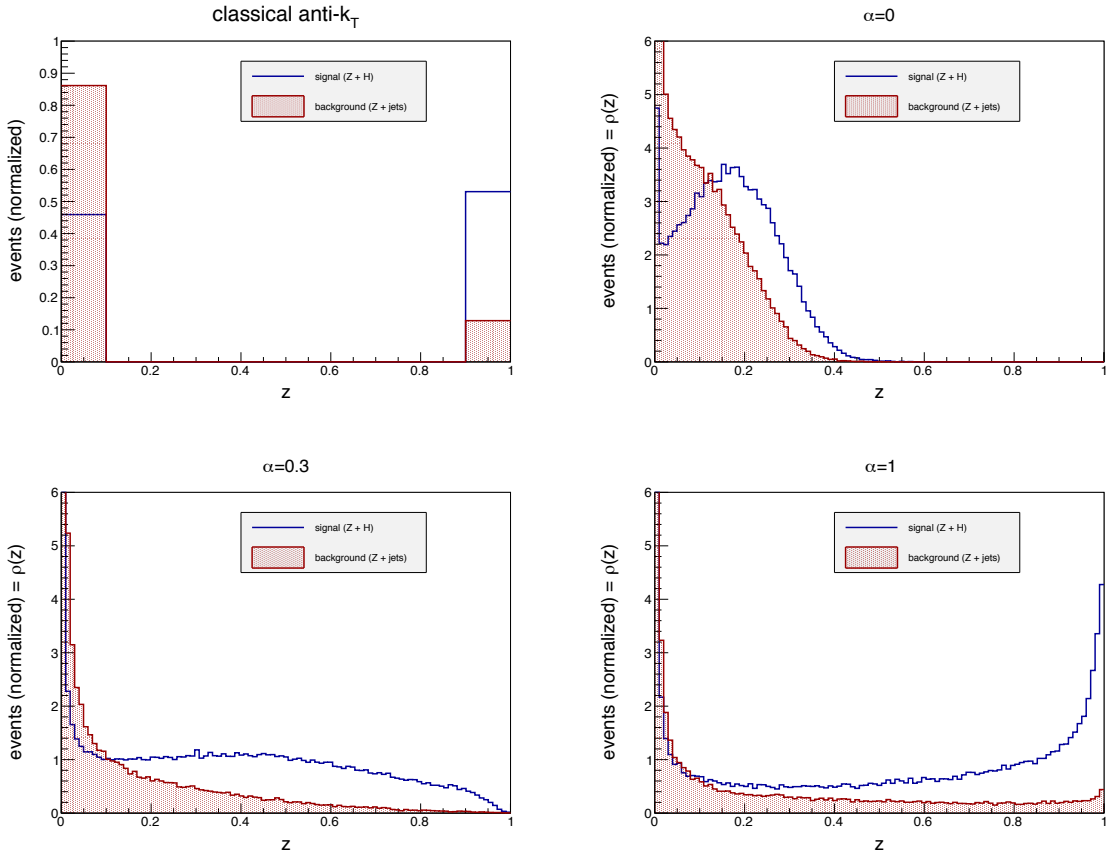

Figure 2.3: z is defined as the fraction of interpretations of an event satisfying a set of cuts. Shown is the distribution of z for signal ($H+Z$ events, hollow, blue) and background ($Z+b\bar{b}$ events, solid, red) for various α. The cuts used to calculate z are 110 GeV $< m_{JJ} <$ 140 GeV and $p_T > 25$ for each jet. Top-left shows the classical case, where an event either satisfies the cuts $z = 0$ or it does not. Distributions are normalized to area 1. These normalized distributions are the functions $\rho(z)$ discussed in Sec. 2.5.

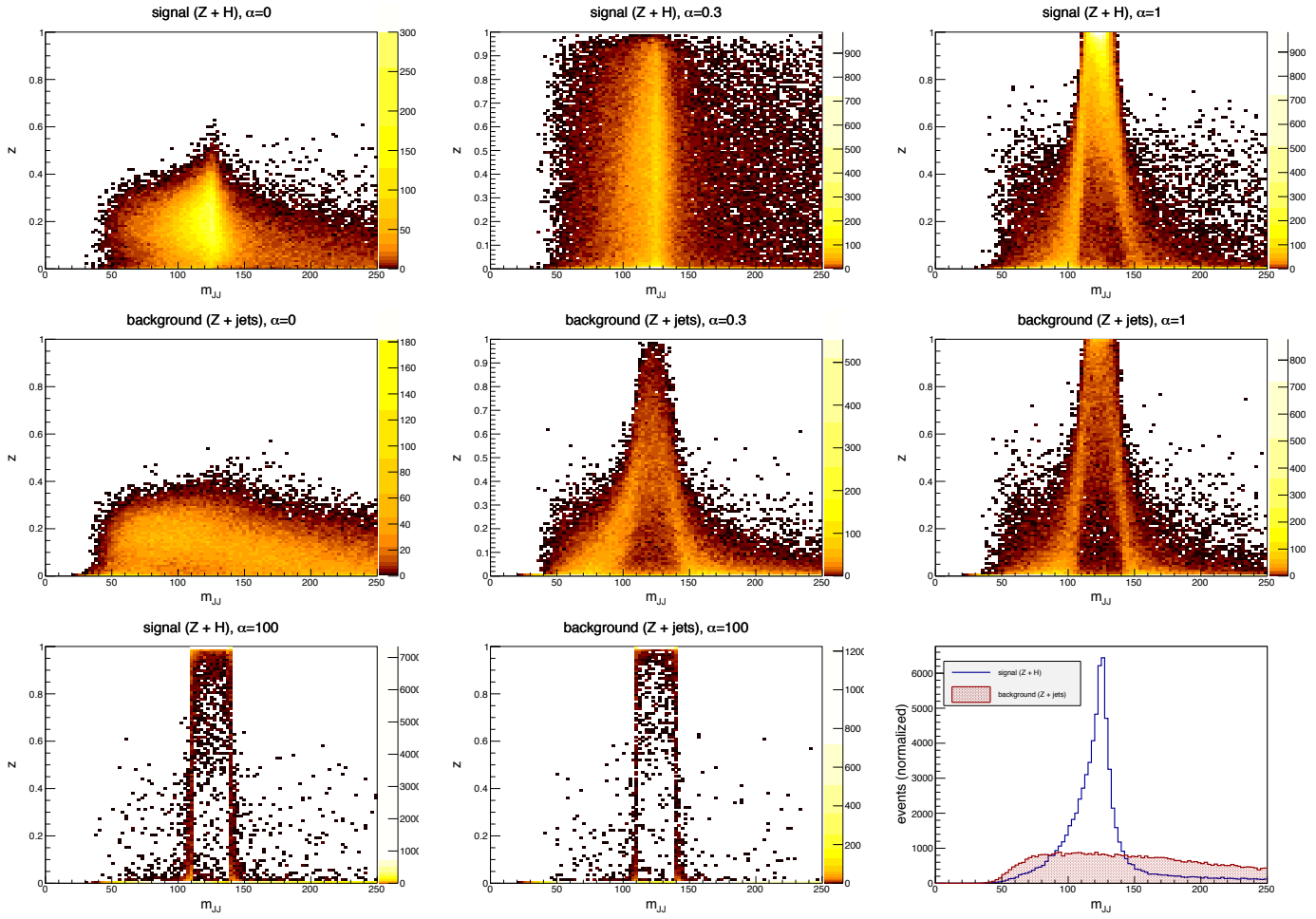

Figure 2.4: z is the fraction of interpretations of an event which satisfy the cuts, as in Fig 2.3. The 2D distribution of z as a function of the classical dijet mass m_{JJ} is shown for some values of α for signal and background. Every event gives a value of m_{JJ} and a value of $0 \leq z \leq 1$. Thus integrating over z reproduces the classical m_{JJ} distribution, as shown in the bottom right. In the classical limit ($\alpha \to \infty$), information from multiple interpretations is inaccessible.

Suppose one decides on a set of cuts which optimally distinguish signal from background for a particular classical analysis. For example, in searching for $H + Z$ events with $H \to b\bar{b}$ one might like to cut on the invariant mass of the $b\bar{b}$ pair. Whatever the cuts are, classically an event either passes those cuts or does not pass them. With Qanti-k_T, a fraction z which we call the **cut-weight**, of the events can pass the cuts.

To get a feel for what the cut-weight distributions look like, we show signal and background distributions of z in Fig. 2.3. Here, signal is $H + Z$ events with $H \to b\bar{b}$ and background is $Z + b\bar{b}$ events. We demand that $p_T^Z > 120$ GeV for all events, imagining Z decays to neutrinos and this is a missing transverse energy cut. The cuts by which z is determined are that the two hardest jets should have $p_T > 25$ GeV and that the dijet invariant mass of the two hardest jets is in the window 110 GeV $< m_{JJ} <$ 140 GeV.

In the classical limit ($\alpha = \infty$), we see that $z = 0$ or $z = 1$ only. That is, an event either satisfies the cuts or it does not. For smaller α, say $\alpha = 1$, there is a substantial fraction of the events for which only some of the clusterings satisfy the cuts. Note that more signal events pass the cuts than background events. For $\alpha = 0$ where the clustering is random, no more than half of the interpretations pass the cuts.

As another way to visualize the value added by cut-weights, we show in Fig. 2.4 how z changes for events with a given classical dijet invariant mass. In a classical analysis, one can look at the distribution of m_{JJ} for signal and background and put a cut to optimize significance. Such a cut corresponds to a vertical band in these plots. Because the distribution of z is different for signal and background events with the same value of m_{JJ} it will help to incorporate z into the analysis. Applying a 2 dimensional cut on m_{JJ} and z provides around a 6% improvement (for $\alpha = 0.1$) in $S/\sqrt{B}$ over a classical (vertical) cuts on the same event.

Combining m_{JJ} with z using both $\alpha = 1$ and $\alpha = 0.1$ using boosted decision trees gives around a 7% improvement. However, cutting on z is not ideal since one is still throwing out events instead of weighting the less signal-like events less. We discuss next how to compute the significance using weighted events.

2.5 Statistics

The fraction z of events passing a set of cuts provides a weight for each event based on how many interpretations of that event resemble signal according to some measure. Thus it is natural to use these weights directly in the calculation of the significance. In this section we discuss how this can be done. The procedure we describe here was used in [7] and is discussed in more detail in [33].

If one knew what the signal and background distributions should look like exactly, the optimal significance would be achieved by using something like a likelihood test. In practice, we never know *exactly* what signal and background should look like. Thus using likelihood ratios can be prone to picking up on pathological regions of simulations. Moreover, it can be extremely challenging to calculate the systematic uncertainty on likelihood-based significance estimates. Cuts provide a compromise where the simulation does not have to be perfect and the systematic uncertainty can be estimated more reliably. Multiple interpretations through the Qjets approach provides a method for combining some of the advantages of both the cut-based and likelihood-based approaches. By using the fraction of interpretations in a window as a cut, one knows explicitly what regions of phase space are contributing (as in a cut-based approach). However, since events that are more signal-like contribute more, the significance of an excess will be greater for a given luminosity than using a cut-based approach alone.

2.5.1 Significance

To quantity the improvement from our procedure we adopt as a measure the excess number of events measured S divided by the expected fluctuations in the background δB. That is,

$$\text{significance} = \frac{S}{\delta B} = \frac{N_{\text{observed}} - N^{\text{bkg}}_{\text{expected}}}{\delta N^{\text{bkg}}_{\text{expected}}} \tag{2.5}$$

For example, suppose we see $S = 100$ excess events in some channel which a Higgs boson could contribute to. If the background was only expected to fluctuate by $\delta B = 20$ events, then the significance is $S/\delta B = 5$, which conventionally characterizes a discovery. That is, in order to replicate the observed number of events, the background without signal would have had to have fluctuated by 5 times more than δB. To calculate the significance with data, one needs to know the mean and variance of $N^{\text{bkg}}_{\text{expected}}$.

A key feature of Qjets is that events are not characterized as signal or background (e.g. by passing some cuts or not passing them). Rather they are assigned a weight z between 0 and 1 based on how many interpretations of the event are signal-like (according to some measure). Thus the measured number of signal events S no longer has to be an integer. Moreover, the fluctuations in the background are now the fluctuations in a non-integer number.

The practical procedure we propose is very simple: count the number of events passing a set of cuts weighted by z. That is, define N_{observed} as the sum over z for each event (rather than counting the number of events with $z = 1$). In order to decide if this number is consistent with a background-only hypothesis, one needs to know the expected fluctuations in this weighted number. We now describe how the expected size of fluctuations can be easily computed. We first review how the expected value and variance of B are computed in a classical analysis and then describe how cut-weights can improve significance.

2.5.2 Classical cut-based significance

Suppose we are looking for a particular signal (like a Higgs boson) in a classical analysis and we design a set of cuts to optimize the discovery potential. Once the cuts are set, we can focus on the background expectation and fluctuations, since these will determine the significance of an observed excess. Let us say with a given luminosity that we expect N background events of a particular type to be produced. Let us say a fraction ϵ of these background events are expected to pass a set of cuts. We call ϵ the **reconstruction efficiency**. Thus, in the absence of signal, we expect $N\epsilon$ events. We would next like to know what the expected variance is around this mean. There are two contributions to the fluctuations about the mean: from the inherent quantum mechanical Poisson process which produces the events in the first place, and from the fact that any individual event has some probability of satisfying our cuts.

The production rate is governed by a Poisson distribution. If we expect N events, the probability of producing n events instead is

$$P(n|N) = \frac{e^{-n}n^N}{N!} \tag{2.6}$$

This Poisson distribution has mean N and standard deviation $\sigma = \sqrt{N}$. The variance is $\sigma^2 = N$.

Now consider the reconstruction efficiency. Say our background events pass our cuts a fraction ϵ of the time. For example, for the samples shown in Fig. 2.3, we can see from the top-left panel (the classical case) that $\epsilon_B = 0.12$ for background and $\epsilon_S = 0.55$ for signal. Suppose there is only signal. If n signal events are produced, what is the probability of

finding a events passing our cuts? It is not hard to see the this probability is given by a weighted binomial distribution:

$$B(a|n,\epsilon) = \binom{n}{a}\epsilon^a(1-\epsilon)^{n-a} \tag{2.7}$$

This distribution has mean ϵn and standard deviation

$$\sigma_n = \sqrt{n\epsilon(1-\epsilon)} \tag{2.8}$$

To describe the full process, where n events are observed from an expected N events and of that n, a events are reconstructed correctly, we combine the two probability distributions and sum over the intermediate variable n. For example, we can ask what is the probability of finding 5 events passing our cuts when we expect 100 to be produced? We have to sum over the probability of reconstructing 5 events from every possible value of the number of observed events, which can range from 5 to ∞. This can be expressed as:

$$P(a) = \sum_{n=a}^{\infty}\left[P(n|N)\cdot B(a|n,\epsilon)\right] \tag{2.9}$$

This distribution has mean ϵN, as expected, and variance $\sigma^2 = N\epsilon$. Thus the uncertainty in the number of background events measured is

$$\delta B = \sqrt{N_B\epsilon_B} \tag{2.10}$$

The significance is then $S/\delta B = N_S\epsilon_S/\sqrt{N_B\epsilon_B}$.

In summary, the uncertainty associated with the number of events gets a contribution

from the Poisson nature of the production process and another contribution from the uncertainty on whether an event will pass our cuts. When both uncertainties are combined the mean and variance of the expected number are both ϵN.

2.5.3 Weighted cuts with Qjets

A trivial observation which simplifies the uncertainty calculation for weighted events is that, since each event is independent, the probability that a of n events will pass a set of cuts is completely determined by the probability that one event will pass the cuts. This is true both for classical algorithms which produces weights $z = 0$ or 1 and algorithms which combine multiple interpretations, like the pruned Qjets algorithm used in [7] and Qanti-k_T described here. We start by rewriting the classical case calculation in terms of single event probabilities, then discuss how the calculation is modified for weighted events.

The cut-weight z denotes how signal-like a single event is: $z = 1$ is very much signal (by some measure) and $z = 0$ is very much background. We can then define a function $\rho(z)$ which gives the probability that an event passes the cuts. For the classical analysis, an event can only have $z = 1$ (signal) or $z = 0$ (background). Thus this probability function in the classical case is

$$\rho_{\text{class.}}(z) = (1 - \epsilon)\delta(z) + \epsilon\delta(z - 1) \tag{2.11}$$

which matches the classical anti-k_T panel of Fig. 2.3.

What is the probability for a single event to pass a set of cuts? We can compute this either using Eq. (2.7) with $a = 0, 1$ or with Eq. (2.11) integrating over z. The two methods

agree:

$$\langle z \rangle = \int dz\, z\, \rho_{\text{class.}}(z) = \epsilon = \sum_{a=0}^{1} aB(a|n=1,\epsilon) \tag{2.12}$$

Similarly, we find

$$\langle z^2 \rangle = \int dz\, z^2\, \rho_{\text{class.}}(z) = \epsilon = \sum_{a=0}^{1} a^2 B(a|n=1,\epsilon) \tag{2.13}$$

Thus if we know that exactly one event is produced, we find

$$\sigma^2_{1,\text{class}} = \langle z^2 \rangle - \langle z \rangle^2 = \epsilon(1-\epsilon) \tag{2.14}$$

as in Eq.(2.8) with $n = 1$.

To get the expected variance on the full distribution, we have to include the Poisson uncertainty which depends on the mean $\langle z \rangle = \epsilon$. By the central limit theorem, since the events are uncorrelated, the characteristic uncertainty on the distribution where N events are expected is

$$\delta_{\text{class}} = \sqrt{N\left(\sigma^2_{1,\text{class}} + \langle z \rangle^2\right)} = \sqrt{N\epsilon} \tag{2.15}$$

in agreement with Eq. (2.10).

With cut-weights $0 \leq z \leq 1$, would also like to know what the probability is that a events pass our cuts if n events were produced at the collider which was expected to produce N events. The new feature in the Qanti-k_T case is that a and z are not necessarily integers. With Qanti-k_T, each event is interpreted multiple times. For each event, a fraction z of the interpretations pass the cuts and a is the sum of the z values over all the measured events. In the Qanti-k_T case the function $\rho(z)$ now has meaning for $0 \leq z \leq 1$. Examples of $\rho(z)$

are shown for various α are shown in Fig. 2.3.

Although the different interpretations coming from Qjets for the same event are highly correlated, each event is uncorrelated with any other. Thus, as with the classical case, the probability of finding a events satisfying the cuts when n events are produced is completely determined by the probability that one event will satisfy the cuts. That is, we do not need to know what the generalization of $B(a|n,\epsilon)$ is in Eq. (2.7), only that it is determined completely by $\rho(z)$.

We calculate the uncertainty with weighted events exactly as we did in the classical case with $\rho(z)$ replacing $\rho_{\text{class.}}(z)$. That is, we calculate

$$\langle z \rangle_\rho = \int dz\, z\, \rho(z) \tag{2.16}$$

and

$$\sigma^2_{1,\rho} \equiv \left[\int dz\, z^2\, \rho(z) \right] - \langle z \rangle^2_\rho \tag{2.17}$$

Then if N events should have been produced, the expected number to be observed is

$$N_{\text{expected}} = N \langle z \rangle_\rho \tag{2.18}$$

The uncertainty on this number is

$$\delta_{\text{Qjets}} = \sqrt{N \left(\sigma^2_{1,\rho} + \langle z \rangle^2_\rho \right)} = \sqrt{N} \sqrt{\langle z^2 \rangle} \tag{2.19}$$

which is just Poisson fluctuations multiplying the root-mean-square (RMS) of the distribution.

In summary, to use weighted events, instead of counting an event as either satisfying a set of cuts ($z = 1$) or not satisfying them ($z = 0$), an event can fractionally satisfy them, giving a weight $0 \leq z \leq 1$. Then the number of observed events is the sum over these z values over all events. For a signal process, this number is written as $S = N_S \langle z \rangle_{\rho_S}$ where $\rho_S(z)$ is given by the cross section for getting a z value of a signal process, normalized to unit area and N_S is the total number of signal events considered. For background, $B = N_B \langle z \rangle_{\rho_B}$ The characteristic size of fluctuations of B is given, in the limit of large number of events where the central-limit theorem can be applied, by $\delta B = \sqrt{N_B \langle z^2 \rangle_{\rho_B}}$. So that

$$\text{significance} = \frac{N_S \langle z \rangle_{\rho_S}}{\sqrt{N_B \langle z^2 \rangle_{\rho_B}}} \tag{2.20}$$

To see how much cut-weights can help, one can take the ratio of this value to the cut-based significance. The overall number of signal and background events considered, N_S and N_B, conveniently drop out of such a ratio.

2.5.4 Reweighting

The procedure we have described can be applied for any way of computing weights. Using multiple interpretations to generate the weight z is natural and intuitive. As a simple generalization, one can consider transforming the weight by any function $t(z)$ to see if significance can be improved. The optimal function will be the one that produces an extremum of the functional

$$\text{significance}[t] \equiv \frac{\langle t \rangle_{\rho_S}}{\sqrt{\langle t^2 \rangle_{\rho_B}}} = \frac{\int_0^1 dz t(z) \rho_S(z)}{\sqrt{\int_0^1 dz [t(z)]^2 \rho_B(z)}} \tag{2.21}$$

The functional variation of the significance is

$$\frac{\delta \text{significance}[t]}{\delta t(z')} = \frac{\rho_S(z')}{\langle t^2 \rangle_{\rho_B}^{1/2}} - \frac{t(z')\rho_B(z')\langle t \rangle_{\rho_S}}{\langle t^2 \rangle_{\rho_B}^{3/2}} \tag{2.22}$$

This vanishes when

$$t(z) = \frac{\rho_S(z)}{\rho_B(z)} \tag{2.23}$$

up to an overall constant which has no effect on the significance enhancement.

To use these results in practice, suppose we are interested in how much luminosity it would take to see a certain signal over a certain background. We first compute the expected numbers N_S and N_B of signal and background events produced at the collider for a given set of cuts. Given these cuts, we can calculate $\rho_S(z)$ and $\rho_B(z)$, as in Fig. 2.3. Thus functions give us $\langle z \rangle_{\rho_S}$ and $\langle z^2 \rangle_{\rho_B}$ (as well as $\langle t \rangle_{\rho_S}$ and $\langle t^2 \rangle_{\rho_B}$ if we want to use reweighted events). We then calculate $S = N_{\text{expected}}^{\text{sig.}} = N_S \langle z \rangle_{\rho_S}$ and $\delta B = \sqrt{N_B \langle z^2 \rangle_{\rho_B}}$. The expected significance is given by $S/\delta B$. With data, one could just look for an excess over expected background. Then S would be replaced by $N_{\text{observed}} - N_{\text{expected}}^{\text{bkg}}$.

As a comparison of the cut-based, cut-weighted, and reweighed approaches, we give the expected significance for each method in Table 2.1 for the $Z + H$ signal and $Z + b\bar{b}$ background samples. Note that since $S/\delta B$ scales as $\sqrt{L}$ (the square root of the luminosity), an improvement in $S/\delta B$ of 28% means that one can make measurements with a significance comparable to standard anti-k_T using only $(\frac{1}{1.28})^2 = 61\%$ of the luminosity. On the other hand, since $S/\delta B$ is proportional to $N_S/\sqrt{N_B}$, for any ρ one can compare the significance for different algorithms and cuts independent of the expected cross section and luminosity.

Table 2.1: Comparison of the significance using the cut-based, cut-weighted, and reweighted methods. The m_{JJ} window used 110 GeV $< m_{JJ} <$ 140 GeV taken from and the significance of this cut is normalized to 1. The mass window has not been optimized (optimizing it on our samples leads to 104 GeV $< m_{JJ} <$ 136 GeV and gives a significance of 1.03). This same 110 GeV $< m_{JJ} <$ 140 GeV window is used to compute the weight functions $\rho(z)$ for signal and background. Cuts refers to the number $N_S/\sqrt{N_B}$ of events in a window, cutting on the $\rho_S(z)$ and $\rho_B(z)$ distributions as well as m_{JJ} in the Qanti-kT cases. "Cut-weighted" refs to using Eq. (2.20) and"cut-reweighted" refers to using Eq. (2.21) and (2.23). All numbers are for the same $Z + H$ sample (signal) and $Z + b\bar{b}$ sample (background), as described in Sec. 2.6.3.

observables	cuts	cut-weighted	cut-reweighted
m_{JJ}	1.00	–	–
$\alpha = 0$	1.00	0.79	0.82
$\alpha = 0.1$	1.01	1.19	1.24
$\alpha = 0.3$	1.00	1.22	1.28
$\alpha = 1.0$	1.02	1.18	1.24

2.6 Example applications

In this section we show how Qanti-k_T can be useful for a variety of searches. We will consider three signals, listed here in ascending order of complexity: (1) a resonance decaying into dijets, (2) a resonance produced in association with a vector boson (including the $H + Z$ example), and (3) pair production of two resonances. We will see that while Qanti-k_T does little to improve ordinary dijet reconstruction, the significance of more complex events can be improved by 50% over a classical analysis.

For each event class, we first process the signal and background events with classical anti-k_T at various different values of R. We then fix the value of R which optimizes the $S/\delta B$ ratio (which for classical anti-k_T is simply $N_S\epsilon_S/\sqrt{N_B\epsilon_B}$). We then use this value of R in Qanti-k_T and compute $S/\delta B$ for different values of rigidity (α). Qanti-k_T is useful to the extent that $S/\delta B$ is larger than $S/\delta B$ for the classical analysis. How $S/\delta B$ is computed in Qanti-k_T was discussed in the previous section. Results are summarized in Table 2.2.

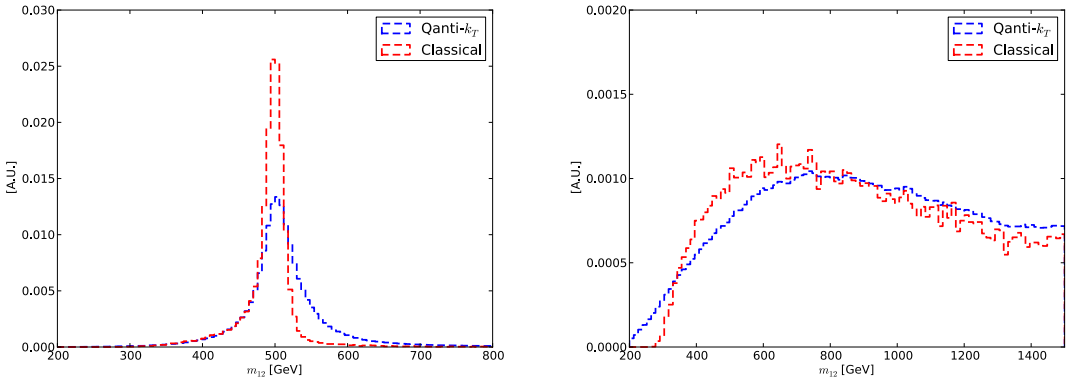

Figure 2.5: A comparison of the signal (left) and background (right) dijet invariant mass distributions using standard anti-k_T and Qanti-k_T for optimized parameters. Signal is $Z\phi \to \nu\bar{\nu}gg$ with $m_\phi = 500$ GeV and background is $Zgg \to \nu\bar{\nu}gg$. All events have $\not{E}_T > 800$ GeV and $p_T > 400$ GeV for each jet.

2.6.1 Simple resonance reconstruction

We consider first a dijet resonance decay to gluons. The signal process is $pp \to \phi \to gg$ with $m_\phi = 1$ TeV. The background is dijet production in the standard model. We consider the two hardest jets in each event, requiring both jets to satisfy $p_T(j) > 425$ GeV and the diet mass to be in the window 950 GeV $< m <$ 1050 GeV. For this process and these cuts, we find that $R = 1.1$ gives the best $S/\delta B$ ratio using classical anti-k_T

Running Qanti-k_T on these samples, we find at most a 3% improvement (see Table 2.2). That we find only a small improvement is perhaps not unexpected in this case. With hard well-separated dijets, any algorithm and most jet sizes should be able to pick out the dijets and get their invariant mass mostly correct. Since there is little ambiguity in the events' interpretation, there is little to gain from resampling with Qanti-k_T.

2.6.2 Boosted resonances in associated production

Next we consider the case where a neutral scalar is produced in association with a Z boson. Unlike in the pure dijet case considered above, when the Z boson and resonance have significant transverse momentum, the jets from the resonance decay will to be closer together and of unequal p_T. Thus, there will be more ambiguity about whether or not the jets pass the p_T cut. For systems with a larger boost there will an additional ambiguity due to overlap between the jets.

First we consider the process $pp \to Z\phi \to gg\nu\bar{\nu}$ where $m_\phi = 500$ GeV. The background is $pp \to Z +$ dijets. We require $\not{E}_T > 400$ GeV, that the two hardest jets satisfy $p_T(j) > 200$ GeV, and that the dijet invariant mass fall within the window 450 GeV $< m <$ 550 GeV. Here we find that the classical value of R that optimizes $S/\delta B$ is 0.95. Running Qanti-k_T on this sample, we find a 9% improvement in $S/\delta B$ at $\alpha = 1.0$.

That the improvement is larger in this case than without the boost is consistent with the intuition that Qanti-k_T helps more when the interpretation of an event is more ambiguous. For boosted resonances, the jet boundaries are close together. A classical algorithm, which only takes one interpretation of the event could easily assign radiation to the wrong jet. With 100 different interpretations of an event, some fraction of those interpretations will more correctly reconstruct the two jets than the classical algorithm

Considering the same 500 GeV scalar but going to higher boost, Qanti-k_T helps even more. We next require $\not{E}_T > 800$ GeV and $p_T > 400$ GeV for each of the jets. This selects the events where the jets are even closer together. Here the optimal R value is found to be 0.65. Using this value of R, we find that with $\alpha = 0.1$, Qanti-k_T produces a $S/\delta B$ 19% larger than in the classical case.

We show the distribution of m_{JJ} for signal and background for the classical and Qanti-k_T samples in Fig. 2.5. In the classical case, each event contributes a single value of m_{JJ}. For Qanti-k_T, each event contributes many (100 in our samples) values of m_{JJ}. Although the Qanti-k_T mass peak is broader for signal (so that S goes down) the improvement in the background stability (so that δB goes down) provides sufficient compensation so that $S/\delta B$ goes up overall.

2.6.3 Higgs +Z

The boosted resonance analysis can be applied to Higgs boson production. Although boosted Higgs production can be considered with jet substructure methods [34], these methods require the boost to be so large that the Higgs decay products merge into a single fat jet. For Qanti-k_T, the boost does not have to be so extreme. In fact, unlike substructure techniques, Qanti-k_T will never degrade significance (although it sometimes will not help much) as long as α is optimized, since $\alpha = \infty$ reduces to the classical case.

We consider $H + Z$ production where the Z decays to neutrinos and the Higgs decays to a b-quark pair ($ZH \to \nu\bar{\nu}b\bar{b}$). As background, we take $Z + b\bar{b}$ production without a Higgs. We require that events yield at least two jets with $p_T > 25$ GeV, $\not{E}_T > 120$ GeV, and that the invariant mass of the hardest two jets fall within the window 110 GeV $< m <$ 140 GeV. The optimal R value for the classical analysis in this case is 0.7. Taking $R = 0.7$ we find that with α is optimized with $\alpha = 0.3$ the $S/\delta B$ improves by 22% using the weighted-cuts approach and by 28% if we reweight by ρ_S/ρ_B as discussed in Sec. 2.5.4 (see also Table 2.1).

28% is a substantial improvement in significance for an $H \to b\bar{b}$ channel. Indeed, a classical multivariate approach involving a sinkful of kinematic and substructure variables [23]

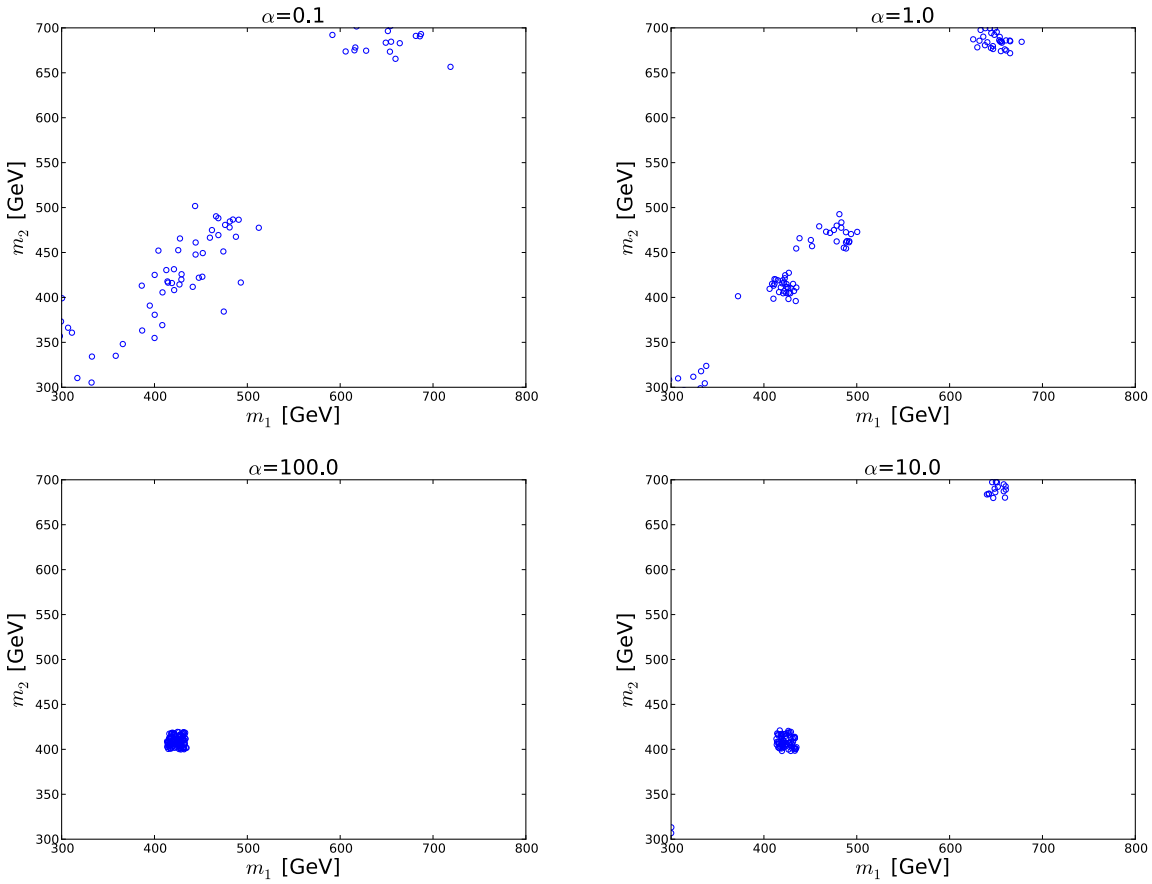

Figure 2.6: The two resonance masses in the $pp \to \phi\phi$ process found for 100 interpretations of a single signal event using Qjets. From top left going clockwise, $\alpha = 0.1$, $\alpha = 1$, $\alpha = 10$, and $\alpha = 100$. We see that while the $\alpha \to \infty$ interpretation of the event does not fall within the mass window, such an interpretation arises when α is relaxed to ~ 1 and below.

was only able to achieve improvements of significance of order 20%. Moreover, the p_T cut of 120 GeV (which can easily be lowered) is not as extreme as the 200 GeV cut proposed in [34], thus more signal events can enter the Qanti-k_T analysis than the boosted one. This at least suggests that the multiple-interpretations approach warrants more detailed study for Higgs searches.

2.6.4 Resonance pair reconstruction

Next, we consider four-jet events to test how well Qanti-k_T works in a more complex jet environment. We consider the process $pp \to \phi\phi$, $\phi \to gg$, where ϕ is again a neutral scalar with $m_\phi = 500$ GeV (see Ref. [35, 36] for similar analyses at ATLAS and CMS). The background in this case is four-jet production in QCD.

In analyzing the four-jet events, while the core Qanti-k_T algorithm remains unaltered we add a preselection step to speed up the analysis (cf. Sec. 2.7). In the preselection step we run both signal and background events through anti-k_T using Fastjet with $R = 0.5$. We then check to see if each of the four hardest jets in each event have $p_T > 120$ GeV. Only events passing this cut are passed through to our non-deterministic anti-k_T algorithm.

Each interpretation of each event using Qanti-k_T (or the single classical interpretation) gives a set of jets. Our goal is to select from these jets the four that yield two pairs which are close to each other in mass. In order to do this, we select the five hardest jets from the final set of jets, form all possible pairs, and calculate the invariant mass for each pair. For each two pairs a and b (representing the reconstructed scalars), we calculate the quantity $|m_a - m_b|/(m_a + m_b)$ to evaluate how close in mass the reconstructed scalars are. We choose the pairing that minimizes the mass difference between the two reconstructed scalars. Once the pairing is chosen, we further require that:

- The mass difference between the two reconstructed scalars is less than 20%: $|m_a - m_b|/(m_a + m_b) < 0.2$
- The average mass $(m_a + m_b)/2$ of the two reconstructed scalars fall within the window $450 - 550$ GeV.

- Each jet used to reconstruct the scalars must have $p_T > 120$ GeV

An example distribution of m_a vs m_b for a single event is shown in Fig. 2.6. We see that the classical analysis ($\alpha \sim 100$) does not find $m_a = m_b = 500$ GeV which would correspond to perfect reconstruction. The distribution of m_a and m_b for finite α shows that many masses can be sampled. More importantly, we see that some samplings come very close to the perfect reconstruction. This shows why Qanti-k_T will be helpful for this multijet sample.

This procedure is applied first to the classical analysis. We find that $R = 0.75$ maximizes $S/\delta B$ in the classical case. Using this value of R, the $S/\delta B$ improvements using Qanti-k_T on the same signal and background events at different values of the rigidity parameter α are shown in Table 2.2. We see that at $\alpha = 0.1$ there is a 49% improvement in $S/\delta B$ over the classical results. As with the previous cases, when α approaches higher values such of 10 and 100, the improvement declines as the algorithm begins to behave more like the classical algorithm. At very low values of α the performance of Qanti-k_T is poor. Again this is expected due to the highly random nature of the mergings at low α with little physical motivation

The large improvement (49%) in significance achievable with Qanti-k_T over the classical analysis is consistent with our expectation that Qanti-k_T helps more in more complicated event topologies. In this case, having four jets rather than two makes the jets more likely to overlap and Qanti-k_T is more likely to be helpful.

2.7 Speed

Unfortunately, adding non-determinism to a jet algorithm and running it 100 times can slow down an analysis significantly. You might expect that running something 100 times

Table 2.2: The improvement in $S/\delta B$ compared to standard anti-k_T for various processes using different values of α, the rigidity parameter. $pp \to \phi + Z$(A/B) denote the $\phi + Z$ processes with a missing energy cuts of 400 and 800 GeV, respectively. The value of R used in both standard anti-k_T and Qanti-k_T is the one which optimizes the standard anti-k_T results. The largest improvements are shown in **bold**.

Sample	R	Improvement in $S/\delta B$ (%)					
		anti-k_T	$\alpha = 0$	$\alpha = 0.01$	$\alpha = 0.1$	$\alpha = 1$	$\alpha = 100$
$pp \to \phi$	1.10	1.0	0.14	0.77	0.89	**1.03**	1.01
$pp \to \phi + Z$(A)	0.95	1.0	0.64	0.99	1.07	**1.09**	1.01
$pp \to \phi + Z$(B)	0.65	1.0	0.58	0.98	**1.19**	1.10	1.01
$pp \to h + Z$	0.7	1.0	0.79	0.99	**1.19**	1.18	1.01
$pp \to \phi + \phi$	0.75	1.0	0.75	1.43	**1.49**	1.40	1.01

(with no optimization) should take at worst 100 times the amount of time it takes to run it once. But actually, our algorithm can be even slower. The reason is that one must recompute $\omega_{ij}^{(\alpha)}$ at each stage in the clustering using a new $d^{\min}$ (see Eq. 2.3), whereas ordinary anti-k_T need only compute the smallest distance at each step. Because of this extra information required, we cannot exploit without modification the computational geometry techniques [37] which makes fastjet fast. The result is that it can take tens of seconds per CPU to run 100 iterations on a event with several hundred particles. This is more of an inconvenience than a problem at the current time. Nevertheless, it would be nice to speed Qanti-k_T up.

While our unoptimized implementation (available at http://jets.physics.harvard.edu/Qantikt) is fast enough for practical use there are a few methods one can employ to speed it up. These include:

- **Preselection**: To avoid unnecessary computation it can be helpful to first require all events pass a loose set of cuts using classical anti-k_T jet before running anti-k_T non-deterministically. This can significantly reduce the number of events processed. For instance, if one is interested in a computation of dijet invariant mass for all events with satisfying $p_T \geq 100$ GeV one might first apply a preselection cut requiring all events

have classical anti-k_T jets which satisfy $p_T \geq 75$ GeV.

- **Limited mergings**: Rather than computing the distance between each pair of four-momenta one can make the physically motivated assumption that a pair of particles further apart than some large distance (say, $\Delta R \geq 2.0$) are unlikely to be part of the same jet. Such pairings can be excluded from the analysis to improve the algorithm execution time.

- **Preclustering**: The runtime scales as $n^2 \ln n$ for n the number of particles to cluster, so its performance is quite sensitive to the number of initial particles. An easy way to reduce the number of particles used as input to the algorithm is to first cluster them into larger micro jets or into a coarser grid. For instance, if one finds that jets of $\delta\phi \times \delta\eta = 0.1 \times 0.1$ yield an algorithm which is too slow, one can merge these into $\delta\phi \times \delta\eta = 0.2 \times 0.2$ cells to realize a $O(16\times)$ speedup.

- **Optimization**: Since much of the distance information is reused from iteration to iteration, there is plenty of potential to speed up the analysis by not recomputing these distances each iteration. More generally, smarter programming should speed up the algorithm significantly, as in fastjet [37].

- **Modification**: Our non-deterministic anti-k_T algorithm is in a sense the simplest way to apply Qjets at the event level. One can easily conceive of other methods which might be better suited to speed-up. A promising approach which just clusters once and then varies the jet size R is discussed in [38].

2.8 Conclusion

In this chapter, we have presented a fundamentally new way to think about events with jets. Traditional algorithms, such as anti-k_T, give a single interpretation of an event. This interpretation can be thought of as a best guess at the assignment of particles into jets. These jets are meant to represent which particles came from the showering and fragmentation of which hard particle. In many events, however, there can be significant ambiguities in which particle belongs to which jet. These ambiguities show up, for example, in how different jet algorithms or jet sizes can give vastly different results for infrared safe observables. The problem is that each algorithm gives a single best guess no matter what – ambiguous events and unambiguous events are treated the same way, and all information about the ambiguity is lost. In other words, an event which is clearly signal-like by some measure is given the same influence over the results as an event which is marginally signal-like (in the sense that it would no longer be signal-like under a small change of parameters).

The idea behind Qjets, which we have used here on the the event level, is that the ambiguity provides useful information about an event. By making a jet algorithm non-deterministic, we can compute the distribution of interpretations around the classical interpretation via Monte-Carlo sampling. When a non-deterministic jet algorithm (for example the Qanti-k_T algorithm we present here) is run 100 times on an event the event 100 different interpretations result. The larger the variation in these interpretations, the more ambiguous an event is. We introduce a parameter α, called rigidity after a similar parameter in [7], which interpolates between classical anti-k_T ($\alpha = \infty$) and purely random clustering ($\alpha = 0$).

There are many ways that an ensemble of interpretations can be used. The simplest way is to construct a Q-observable such as the variance of some classical observable (like

the jet mass) over the interpretations. An example of this approach is the volatility variable introduced in [7]. One can then cut on this variance to improve significance. However, since almost all events are signal-like to some extent, it makes more sense to include all the events in the analysis, with a weight based on the fraction interpretations passing a set of cuts. We derive a formula for the significance using weighted events which can be used to incorporate information from all the interpretations of all the events, rather than cutting some events out all together.

We applied Qanti-k_T to a number of types of events. We find that unambiguous processes, like those which produce hard and well-separated jets, do not benefit much from this procedure. However, for more complicated processes, such as those with softer or overlapping jets, the significance can be improved significantly. In a toy example, we showed that pair production of dijet resonances one can realize a 49% improvement in $S/\delta B$.

Using weighted events from multiple interpretations has the potential to improve substantially searches for the Higgs boson and measurements of its properties. We found that for $pp \to ZH \to \nu\bar{\nu}b\bar{b}$ events at the 8 TeV LHC with $p_T^Z > 120$ GeV, one can realize an 28% improvement in significance over an equivalent classical analysis. We chose this p_T fairly arbitrarily. With a p_T cut less than 120 GeV and we still expect Qanti-k_T to improve significance, although perhaps not by as much. That is, the methodology of using multiple interpretations not restricted to the highly boosted regime, as are other approaches to finding the Higgs in this channel [34]. For other Higgs associated production channels (such as $pp \to WH$ and $pp \to t\bar{t}H$) with $H \to b\bar{b}$, we expect the Qjets framework to be similarly helpful.

The Qanti-k_T algorithm introduced in this chapter be used whenever ordinary anti-k_T

is employed. While more complex event topologies tend to benefit more, Qanti-k_T will at least never make an analysis worse. Indeed, since for $\alpha = \infty$, Qanti-k_T reduces to ordinary anti-k_T, as long as one scans over α, no harm can come (other than wasting time). It is natural to consider applying Qanti-k_T or some variation within the Qjets framework to challenging processes, such as top-tagging. When tops are very boosted, it is likely that substructure methods will work better [39] (although merging Qjets with substructure is also promising), however, in the intermediate regime [40] with moderate boost Qjets could help a lot. It would also be interested to see if Qjets can help with color flow [41, 42], quark and gluon discrimination [43, 44], ISR tagging [45] or in any situation where ambiguities in reconstruction are problematic.

Chapter 3

Measuring the Bottom-Quark Forward-Central Asymmetry at the LHC

3.1 Introduction

Analyses by the CDF [46, 47, 48] and D0 [49, 50] collaborations suggest that the top forward-backward asymmetry is much larger than predicted by the Standard Model (SM). This asymmetry, which essentially measures the extent to which the top in $t\bar{t}$ production has a preference to be aligned with the initial state quark (rather than anti-quark) is only a few percent within the SM, yet has been measured to be $O(10\%)$ in inclusive $t\bar{t}$ samples, and even $O(40\%)$ at high $m_{t\bar{t}}$. The latest results from CDF further demonstrate that the large asymmetry manifests itself at the 3σ level in both the semi- and fully-leptonic $t\bar{t}$ decay channels, making naive systematic/statistical effects a less likely explanation for the effect.

While recent results from D0 [50] disagree somewhat with those of CDF in several areas (most importantly in the behavior of A_{FB} at large invariant mass), and the LHC has yet to observe evidence for any similar new-physics effects [51, 52], this asymmetry remains one of the most compelling experimental anomalies.

Indeed, as the top asymmetry continues to resist a more conventional explanation, many models of new-physics have been put forth to explain the anomaly [53, 54, 55, 56, 57, 58, 59, 60, 61, 62, 63, 64, 65, 66, 67, 68, 69, 70, 71, 72, 73, 74, 75, 76, 77, 78, 79, 80, 81, 82, 83, 84, 85, 86, 87], see Ref. [88] for a review. These models typically introduce new heavy intermediate particles to generate the top asymmetry via interference with the SM, and differ principally in (1) whether they are s, t, or u-channel, (2) in the spin/color of the new degrees of freedom, and (3) in their couplings to the first and third generation quarks. While it is true that many of these models seem to be in tension with other measurements (especially the $t\bar{t}$ differential cross section and searches for same-sign tops at the LHC [89]), such considerations can be subtle [90, 91] and various models may still be able to reproduce the $t\bar{t}$ asymmetry while maintaining consistency with other measured properties of the top. Thus, to make progress in understanding the origin of the top asymmetry it is helpful to keep an open mind toward new models and subject them to further experimental scrutiny. Many analyses have already been proposed with this aim, including an LHC measurement of the top-quark forward-central asymmetry [92, 93, 94, 95, 96], studies making use of the polarization/spin-correlation in the $t\bar{t}$ system [97, 98, 99, 100, 101, 102, 103, 104, 105], and more specialized analysis designed to look for the signatures of particular models [106, 107, 108, 109, 110].

Since the flavor structure of the various models differs widely, it is important to measure similar asymmetries for other quarks. To wit, if the asymmetry in $t\bar{t}$ is indeed due to the

effects of new physics, then one must ask if these only apply to the top-sector, or if they affect the entire third generation of fermions. Models of t/u-channel physics, for example, tend to affect only the right-handed top (or, in some cases, the entire up-type sector), using a flavor off-diagonal interaction to couple it to a first generation u or d. In contrast, the simplest axi-gluon models couple new-physics with opposite signs to the left and right handed tops, and so necessarily include new couplings to the bottom sector.

It has been pointed out recently [111, 53] that the data sets at the Tevatron are large enough to allow interesting measurements of the forward-backward asymmetries of both bottom and charm quarks in the same kinematic regime in which the top asymmetry is observed by CDF. This can be done with a dijet sample, using the charge asymmetries of muons embedded in high-p_T jets. The muon charge asymmetry is correlated with the charge asymmetries of the main sources of muons, namely c and b quark decays. The forward-backward asymmetry prior to heavy-flavor tagging is dominated [111] by a combination of the $c\bar{c}$ and $b\bar{b}$ asymmetry, and separating bottom from charm can be done using heavy-flavor tagging and kinematics. This analysis could help discern the different signatures of the various classes of models, especially when used in concert with some of the other tools referenced above.

In the current chapter we consider a similar measurement at the LHC. We will limit ourselves to the bottom quark asymmetry. This is because the dilution of the asymmetries from symmetric backgrounds is much larger at the LHC than at the Tevatron, making charm asymmetries extremely difficult to detect.[1]

[1]With an asymmetry comparable to that seen in $t\bar{t}$ samples, the observed raw asymmetry prior to heavy-flavor tagging would be of order 2–3% at the Tevatron [111]. But at the LHC it would be a factor of 10 smaller, presumably too low for beating systematic errors. Only with heavy-flavor tagging can the observed asymmetries at the LHC reach the percent level and above, but tagging removes most of the charm sample,

Clearly, in contrast to the Tevatron and its beams of opposite charge, one cannot as simply measure a forward-backward asymmetry at a parity-symmetric collider like the LHC, whose beams are both of protons. But one can instead make use of the fact that in quark-antiquark collisions in a proton-proton machine, the motion of the parton center-of-mass frame relative to the lab frame is correlated with the direction of the incoming quark. Thus one may define a "forward-central" asymmetry, looking at whether b quarks tend to be at higher rapidity $|y|$ on average than $\bar{b}$ antiquarks. A corresponding observable is employed by most analyses which propose to measure the $t\bar{t}$ asymmetry at the LHC, e.g. Ref. [92, 93, 94, 95].

As in [111, 53], following [112], we will use the charge of a muon embedded in a jet to determine whether the parent of the jet is more likely to be a b or a $\bar{b}$. The muon also provides us with an object for triggering. We will also use b tagging and kinematic cuts to reduce backgrounds. As we will see, the measurement is difficult, although potentially feasible. For an underlying asymmetry of the size needed to explain the CDF $t\bar{t}$ anomaly, we are only able to obtain an observable asymmetry of order 2% or less, which is several times smaller than the corresponding forward-backward asymmetry at the Tevatron, yet we expect such an asymmetry to be visible above the 2σ level in 10 fb^{-1}. We note that an asymmetry of the size expected in the Standard Model should be unobservable for the foreseeable future. The Tevatron data set may well be an easier place to make the measurement. However, we have certainly not exhausted all the options for improving the signal-to-background ratio at the LHC, and we feel our result should be viewed as encouraging, though in need of improvement by more sophisticated means.

This chapter is structured as follows. In Sec. 3.2 we define the forward-central asymmetry

leaving sensitivity only to $b\bar{b}$ physics.

carefully. Later, in Sec. 3.3, we will describe a set of cuts designed to optimize the discriminating power of this quantity in the kinematic region relevant for the top asymmetry. *We emphasize that the signal region lies precariously close to the trigger thresholds, and some consideration of trigger strategy must be made in the near future if one is to ensure that the data relevant for this measurement is actually recorded.* Introducing a signal comparable to that observed at the Tevatron (using a conservative axigluon toy model) we will show that a 7 TeV LHC can resolve an asymmetry in b-quark production at more than 2σ in 10 fb^{-1}. While this level of statistical significance is not sufficient to claim the discovery of new phenomena, it would provide helpful model-building input, allowing ATLAS and CMS data to restrict the set of models which have been put forward to explain the $t\bar{t}$ anomaly. We comment on various experimentally relevant issues and the prospects for an LHCb measurement of the asymmetry in Sec. 3.4. We conclude in Sec. 3.5.

3.2 Observable

There are two natural forward-backward asymmetries to consider at a proton-antiproton machine, as applied to $b\bar{b}$ production. The first is to define forward and backward in the lab frame

$$A_{FB}^{b\bar{b},\text{lab}} = \frac{N(qy > 0) - N(qy < 0)}{N(qy > 0) + N(qy < 0)}, \tag{3.1}$$

where $q = 1$ (-1) for the $\bar{b}$ (b) that generates the jet containing the observed muon, and y is its rapidity[2]. Here $y \to +\infty$ $(-\infty)$ is the direction of motion of the proton (antiproton). But the event-by-event boost of the hard-scattering system tends to wash out this variable,

[2]One could construct a similar analysis employing pseudo-rapidity (η) instead of rapidity(y). As we are considering objects for which $m \ll p_T$, the results obtained would be largely the same.

so it is better to consider forward and backward defined in the hard-scattering rest frame

$$A_{FB}^{b\bar{b}} = \frac{N(q\Delta y > 0) - N(q\Delta y < 0)}{N(q\Delta y > 0) + N(q\Delta y < 0)}, \tag{3.2}$$

where Δy is the signed rapidity difference between the b and the $\bar{b}$ (*i.e.*, the rapidity difference between the two jets signed by the muon charge.)

At a proton-proton machine such as the LHC, symmetric under $y \to -y$, these forward-backward asymmetries will necessarily be zero. Instead we must turn to a forward-central asymmetry, which we define as:

$$A_{FC}^{b\bar{b}} = \frac{N(q\Delta|y| > 0) - N(q\Delta|y| < 0)}{N(q\Delta|y| > 0) + N(q\Delta|y| < 0)}, \tag{3.3}$$

where now $\Delta|y| = |y(b)| - |y(\bar{b})|$ is defined as the rapidity difference between the rapidity of the b and the $\bar{b}$.[3]

If we consider a $q\bar{q}$-initiated scattering process in a pp system, the direction of the boost of the hard-scattering system along the beam direction will tend to reflect the direction of the initial state quark. This effect is illustrated in Fig. 3.3.

It is instructive to consider the behavior of Eqs. (3.2) and (3.3) under various reflection symmetries to determine their susceptibility to shifts from experimental errors. The forward-backward asymmetry measured at the Tevatron, for instance, flips sign ($A_{FB}^{b\bar{b}} \to -A_{FB}^{b\bar{b}}$) if either $y \to -y$ or $q \to -q$. This tells us if there were no asymmetry to begin with, one would not be induced via a distortion in the efficiency to measure one charge over the other

[3]We note that a differential distribution of the asymmetry, e.g. $dA_{FC}^{b\bar{b}}/d\Delta|y|$ or $dA_{FC}^{b\bar{b}}/dy_{jj}$ (see Eq. 3.4) may provide an even more powerful discriminant, although for simplicity we will not consider these here.

as long as both sides of the detector saw the same distortion. That is, the only way to find a spuriously non-zero value in $A_{FB}^{b\bar{b}}$ would be to introduce a distortion in the charge efficiencies which was not invariant under $y \to -y$. The situation at the LHC is more subtle as $A_{FC}^{b\bar{b}} \to +A_{FC}^{b\bar{b}}$ under $y \to -y$, but one still has $A_{FC}^{b\bar{b}} \to -A_{FC}^{b\bar{b}}$ under $q \to -q$, which tells us that to the extent the detection efficiencies for muons and antimuons are equal, at any given rapidity, it is still the case that no asymmetry can be generated if none exists. We therefore emphasize that while every effort should be made to correct for detector and trigger effects to obtain a reliable measurement, the forward-central asymmetry of Eq. (3.3) is fairly robust against systematic shifts from rapidity-dependent efficiencies.

Of course, the asymmetry (or limit on an asymmetry) observed in data must be converted into an asymmetry (or limit) in the underlying $q\bar{q} \to b\bar{b}$ process. This translation will require careful modeling of the muon efficiency as a function of y. But this last is also true for the Tevatron measurement, which involves an integral over y, so there too one must account for the y-dependent detection efficiencies.

3.3 LHC Analysis

As in [111, 53], our strategy is to consider dijet events in which one of the two leading jets has an embedded muon, and to use the muon's charge as an approximate surrogate for the charge of the parent b quark [112]. The resulting forward-central asymmetry in charged non-isolated muons is diluted by many effects, to be discussed below, but its value does correlate with the forward-central asymmetry in $q\bar{q} \to b\bar{b}$ events we wish to measure.

Let us first define our event sample. We will assume that a trigger exists that can easily accommodate a single non-isolated muon of 25 GeV within an event with at least one jet of

Table 3.1: Cuts used to select events and to increase the signal size. We denote the i-th hardest jet as j_i. The effect of the cuts can be seen in Table 3.2.

Selection cuts	**Jets**: We require at least two jets with $\|y(j)\| < 2.4$, and further demand $p_T(j_1) > 150$ GeV and $p_T(j_2) > 100$ GeV. **Muon:** There must be a μ close to j_1 or j_2 satisfying $\Delta R(j,\mu) < 1$, $p_T(\mu) > 25$ GeV, and $\|y(\mu)\| < 2.4$ **Flavor tag:** Finally, we require that the jet *without* the nearby muon is b-tagged.
Forward cut	$\|\frac{y(j_1)+y(j_2)}{2}\| > 0.5$
Mass cut	$m(j_1 + j_2) > 450$ GeV

150 GeV and H_T of at least 250 GeV.[4] We will see this accords with the requirements of the measurement. Significantly higher thresholds might put the measurement out of reach. Within this sample we demand the jets be di-jet-like[5] and veto events with an isolated lepton.

To put ourselves in the same mass region as is probed by the measurements of the $t\bar{t}$ asymmetry, we will focus on dijet events where the hardest jet's p_T is greater than 150 GeV and the second hardest's is greater than 100 GeV. As we will later demand a muon in one jet and a b-tag on the other, we require that both jets lie within $|y| < 2.4$ so they are within the tracking system. Later we will see that an additional cut requiring $m_{jj} > 450$ GeV will help us to further increase the signal to background ratio, although it will not help increase the statistical significance of the results.

The charge of the muon does not provide a fully reliable measure of the initiating quark's

[4]We note that the cross section for events passing this particular trigger stream is roughly 1 nb at a 7 TeV LHC, and so could be easily accommodated in $L \sim 10^{33}\text{cm}^{-2}\text{s}^{-1}$ running.

[5]Events that differ strongly from dijet structure — for instance, those in which the two leading jets are not fairly back-to-back or have MET that does not point roughly in the direction of one of the leading jets — should be vetoed. However these vetoes should be loose and chosen with some care to avoid making theoretical calculations of backgrounds unstable.

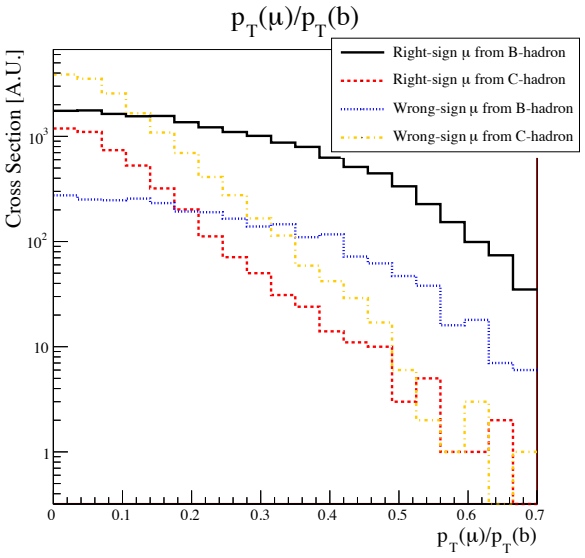

Figure 3.1: The fractional p_T carried by a muon produced from the hadrons of a b-jet with $p_T > 150$ GeV where we have distinguished right-sign muons ($b/\bar{b} \leftrightarrow \mu^-/\mu^+$) from wrong-sign muons($b/\bar{b} \leftrightarrow \mu^+/\mu^-$).

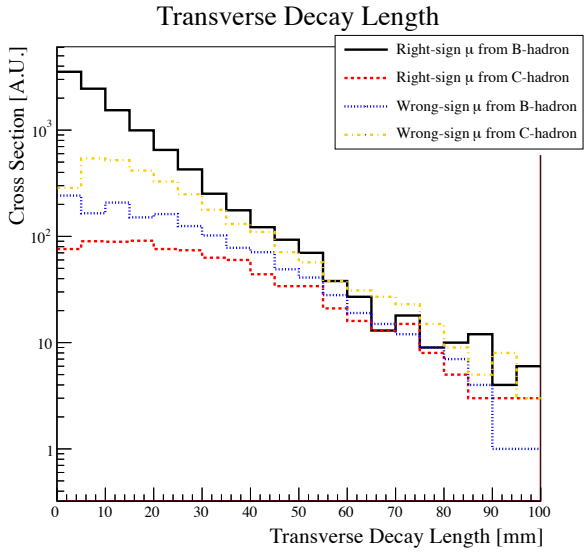

Figure 3.2: The transverse decay length of the secondary vertex which gives rise to the muon. Here we have required b-jets with $p_T > 150$ GeV and $p_T(\mu) > 25$ GeV.

charge, due to a combination of effects. The largest of these, at least when the muon carries a low fraction of the jet's p_T, comes from the decay of a b-quark into a c, whose subsequent decay produces a wrong-signed muon. Another cause of wrong signed events is from neutral B-meson oscillations which switch constituent b's to $\bar{b}$'s, and vice-versa. To reduce the concentration of wrong-signed events, it is helpful, for jets with p_T of order 150 GeV, to take the muon inside the jet to have p_T above 25 GeV. This is illustrated in Fig. 3.1, where we show the relative fraction of the jet p_T carried by the muon for b-jets with $p_T > 150$ GeV. As emphasized above, we are assuming here that 25 GeV is compatible with an available trigger pathway. This assumption appears to be correct at current luminosities but may not necessarily remain so throughout the 2011-2012 run.

Only a fraction of the selected events will contain a $b\bar{b}$ final state, with other contributions from $c\bar{c}$ pairs, gluons that split to heavy flavor, and events with a single b or c. We significantly reduce the unwanted contributions by demanding that among the two hardest jets, the jet that does not contain the muon is b-tagged.[6] This is our "initial selection". Already, as we will see, there is sensitivity to an asymmetry comparable to that seen in the $t\bar{t}$ system. But the initial sample is not very pure, and the observed asymmetry would be very small, less than one percent. To increase the size of the observed asymmetry, with limited effect on the sensivity, we impose additional cuts.

In our initial selection sample, the symmetric process $gg \to b\bar{b}$ dominates over the process we hope to probe: $q\bar{q} \to b\bar{b}$. We can attempt to mitigate this dilution by using the fact that, at fixed H_T, the partonic center-of-mass frame in gg events tends to be at lower $|y|$ than in

[6]Tagging the jet containing the muon would not assist, since the relatively hard non-isolated muon is already indicative of a b jet. However, see the discussion section below.

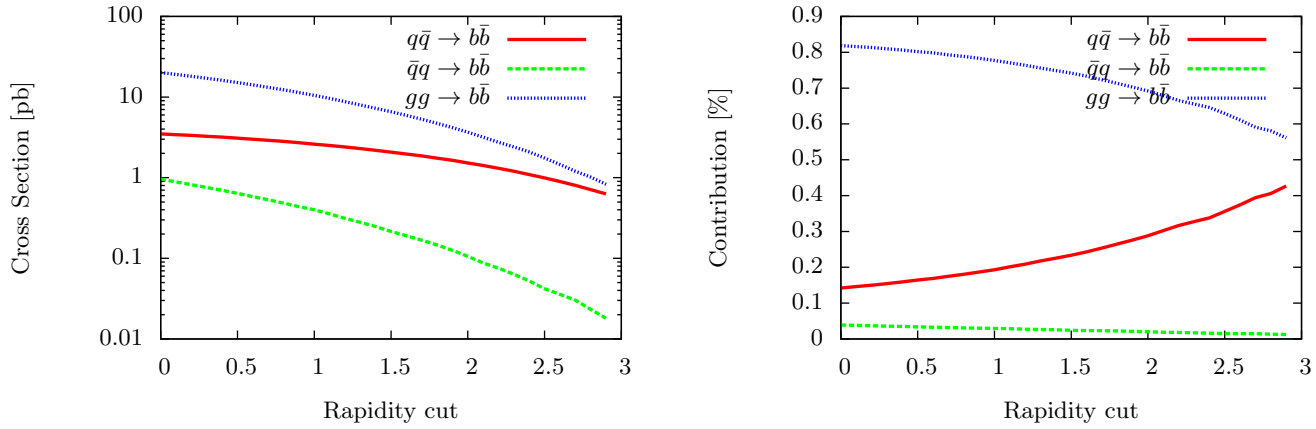

Figure 3.3: Left: The cross-section for $b\bar{b}$ production as a function of the minimum rapidity cut on $y_{jj} = [y(j_1) + y(j_2)]/2$ for various initial states subject to the 150 GeV p_T cut used in the analysis. For the $q\bar{q}$ initial state the quark moves in the direction of the center-of-mass as measured in the laboratory, while for the $\bar{q}q$ state the anti-quark moves in this direction. Right: The relative contribution from each initial state to the $b\bar{b}$ sample as a function of the minimum rapidity cut.

$q\bar{q}$ events. We define the average rapidity of the dijet system to be

$$y_{jj} = \frac{y(j_1) + y(j_2)}{2} \tag{3.4}$$

and apply a cut $|y_{jj}| > y_{\min} = 0.5$ requiring that the system be relatively forward. The effects of such a cut can be seen in Fig. 3.3 where we show how such a cut increases the relative contribution of 'right-orientation' $q\bar{q} \to b\bar{b}$ events — ones where the quark is moving in the same center-of-mass direction as the lab-frame $b\bar{b}$ system — while decreasing both the symmetric ($gg \to b\bar{b}$) and 'wrong-orientation' $\bar{q}q \to b\bar{b}$ (where the anti-quark moves in the same direction as the scattering system) backgrounds. For the sake of simplicity we will only employ a sharp cut on $|y_{jj}|$, but a more powerful analysis could make use of a continuous discriminant to achieve a higher significance.

Furthermore, as we wish to measure the extent to which any new physics giving rise to the top asymmetry might be affecting the bottom sector, the best place to look for it is probably in the same kinematic region where the top anomaly is observed by CDF, namely at $t\bar{t}$ invariant mass above 450 GeV. We will therefore focus on events with a similar requirement that $m_{jj} > 450$ GeV. (Recent results from D0 might lead one to rethink this step, but in any case, as we will see, this cut is useful but not essential.) This also reduces backgrounds more than signal.

Our cuts are summarized in Table I. To quantify our results we introduce an asymmetric $b\bar{b}$ signal that is comparable, in the appropriate invariant-mass range, to that seen in $t\bar{t}$ at the Tevatron. We do this in a way that we believe is conservative. In particular, we use a toy model similar to the minimal two site axigluon model described in Ref. [53]. We choose the axigluon mass to be $M_{G'} = 1041$ GeV and the width to be $\Gamma(G') = 200$ GeV; we set its vector-like coupling to zero, and set its axial coupling equal in strength to the QCD coupling.[7] Using these parameters we find a rest-frame parton-level asymmetry in acceptable agreement with that observed in the top system at both CDF and D0: 8% for invariant mass less than 450 GeV and 30% for invariant masses above 450 GeV. To avoid assumptions about what occurs above the reach of the Tevatron, we only consider events (the significant majority, in any case) with $m_{jj} < 800$ GeV. This is well below the axigluon pole, which avoids sensitivity to the model-dependent resonance structure of the axigluon. Note that although our toy model may itself be excluded by 2011 LHC data, we are only using aspects of the model that are largely model-independent. For instance, a different toy model with a larger axigluon mass and coupling would give a similar signal to the choice

[7]The sign of the coupling of the axial gluon to the first generation is opposite to that of the coupling to the third generation.

made here for $m_{jj} < 800$ GeV. Any additional contributions to the asymmetry above 800 GeV will only make new-physics effects more prominent.

Before we proceed we describe our Monte-Carlo analysis tools: we use `Madgraph v.4.4.60` [113] to generate our parton-level $gg \to b\bar{b}$ and $q\bar{q} \to b\bar{b}$ samples, which are then showered in `Pythia v.6.4.24` [30]. Both of these generators are used with their default PDF distributions: CTEQ [114] 6L1 and 5L, respectively. Our calculations ignore the next to leading-order asymmetry in b-production present in the SM, although we expect[8] this to be subdominant compared to the new-physics effects we consider, and would at most yield a small linear shift in our results. The other processes which constitute our background[9] are generated and showered in Pythia. After generation, all events are clustered into jets between $-5 < \eta < 5$ by `Fastjet v.2.4.2` [116, 37] using the anti-k_T algorithm [15] with $R = 0.7$. We will assume a b-tagging efficiency of 50%, a c-fake rate of 10%, and a light-jet fake rate of 0.3% [117].[10]

It is instructive to study the composition of processes contributing to the non $q\bar{q}/gg \to b\bar{b}$ background (i.e., what goes into the "other background" row in Table 3.2). The largest component of these events comes from the production of events with real b-quarks, the rate for which we find to be roughly comparable to that of $gg \to b\bar{b}$ processes. Of these, approximately 60% come from flavor excitation processes and the rest come from gluon splitting in the parton shower. The next largest contribution comes from processes in which

[8]From Ref. [115] we estimate that the asymmetry in b production at the Tevatron is $\mathcal{O}(6\%)$ at high energies, to be compared to the $O(30\%)$ one might expect from new-physics effects.

[9]The backgrounds for our study, aside from the symmetric $gg \to b\bar{b}$ process which we generate with Madgraph, include process with light-jets, processes with charm jets, gluon-splitting processes (e.g. $g \to b\bar{b}$) and flavor-excitation processes ($bx \to bx$).

[10]More precisely, we scan inside a jet for a b- or c-containing hadron, and tag with the above efficiencies if one is found.

Table 3.2: The rates of various contributing processes, the forward-central asymmetry and and the statistical significance after selection, rapidity and invariant mass cuts (the cuts are presented in Table 3.1). We denote by $q\bar{q} \to b\bar{b}$ the 'right-orientation' $q\bar{q}$ intial state, and by $\bar{q}q \to b\bar{b}$ the 'wrong-orientation' state. Our 'other background' contribution includes processes of flavor excitation and gluon splitting, as well as fake b's from charm and light flavor. The results account for a tagging efficiency of 50%/10%/0.3% for b/c/light-flavor jets. The significance is measured as $1/\sqrt{N}$ assuming $L = 10$ fb^{-1}.

	Selection	$y_{jj} > 1/2$	$m_{jj} > 450$
$\sigma_{q\bar{q}\to b\bar{b}}$ (pb)	1.1	0.9	0.3
$\sigma_{\bar{q}q\to b\bar{b}}$ (pb)	0.3	0.1	0.0
$\sigma_{gg\to b\bar{b}}$ (pb)	7.1	4.0	0.9
other background	10.0	5.7	1.6
σ_{total}(pb)	18.6	10.7	2.7
$A_{FC}^{b\bar{b}}$(%)	0.6	0.9	1.6
significance (σ)	2.5	2.8	2.6

a c fakes a b. The rate for this process, before accounting for the efficiency of a c to fake a b, is roughly twice the rate for $gg \to b\bar{b}$ (again, before tagging efficiencies). Finally, the raw rate for processes yielding a muon in one jet but no c/b-hadrons in the other is usually ten to twenty times the rate for $gg \to b\bar{b}$ production, but once one applies the 0.3% efficiency for light QCD to fake a b-jet, this process makes the smallest contribution of those considered. Now, since many of our jets are at high p_T and high y, this may be a low estimate on the light QCD mistag rate. However, the rate is so small that our result is not very sensitive to the mistag rate, which could be as large as a few percent without having a qualitative impact on our conclusions.

Our results showing the behavior of $A_{FC}^{b\bar{b}}$ as various cuts are imposed are presented in Table 3.2. Beginning with the initial selection cuts we first apply a cut on y_{jj} which increases the observed asymmetry by $\sim 50\%$, and next apply a cut on m_{jj} to increase the observed asymmetry by another $\sim 80\%$. While both of these cuts have a minimal impact

on the statistical significance of the measured asymmetry, the increase in its absolute size is comforting as it reduces the impact of systematic errors. A sensitivity of more than 2σ is possible with about 10 fb^{-1} at 7 TeV.

3.4 Discussion

Let us first make a brief theoretical comment before turning to the more serious experimental issues. In presenting the estimates of the previous section we have aimed to remain relatively conservative. Our toy model yields a somewhat small asymmetry compared to the CDF results, and if new physics is indeed present it may generate larger effects than we considered and would therefore manifest itself sooner. We have not accounted properly for K factors, but they tend to be larger than 1 for QCD di-jet processes. Accounting for them is unlikely to change the signal-to-background ratio very much though the statistical significance we found may slightly improve (though admittedly the improvement is likely to be cancelled by experimental inefficiencies.) We have no reason to expect unusually large K factors given that we have not introduced restrictive cuts on phase space. Also we should emphasize that a change in the relative rates of the different contributing processes will not induce a new source of asymmetry.

We believe that dominant sources of theoretical uncertainty affecting the analysis we propose are probably the uncertainties on (a) the values of the NLO K-factors, which will affect all of the production rates, (b) the gluon, c, and b PDFs, which are important in the backgrounds, and (c) the process of gluon splitting to $c\bar{c}$ and $b\bar{b}$ within a jet, which is also important for the backgrounds. The uncertainty on the Standard Model prediction for $A_{FC}^{b\bar{b}}$ is likely unimportant. We further note that there are a number of data-driven handles

that might be useful for determining backgrounds, including observables such as (a) the probability for a jet to contain two b-tags or multiple muons (both same- and opposite-sign), (b) the embedded muon p_T and k_T spectra (where k_T is measured with respect to the jet axis), and (c) tracking/vertexing information on b/c hadrons within jets.

A serious concern that we cannot address here involves the trigger. It is not clear to us that the cuts required for the analysis are compatible with the triggers that will be used in accumulating 10 fb^{-1} of data. Again, the ingredients of the analysis are simple: a dijet event with the leading (sub-leading) jet carrying 150 (100) GeV of p_T, one of the two jets containing a muon with 25 GeV of p_T and the other b-tagged. A non-isolated-muon-plus-H_T trigger might be a suitable pathway, perhaps supplemented at higher trigger levels by requiring at least one of the two jets to contain displaced tracks. Requiring the muon track in particular to be slightly displaced is another possibility, but comes at the high cost of reduced statistics and possible challenges for trigger-acceptance determination. We must leave these important details to our experimental colleagues.

There is potentially additional room for the experiments to improve upon the analysis we have presented. The most obvious step would be to include electronic decays in addition to the muons used here, but since electrons come with a higher trigger threshold it is not clear this would add much sensitivity. Another potential source of improvement[11] could come from using the displacement distance of displaced vertices to reduce the dilution of the underlying asymmetry from neutral B meson oscillations. If the ATLAS or CMS vertexing systems could with sufficiently high efficiency measure the displacement of the secondary vertex which produces the μ, this would allow separation of samples in which the B meson

[11]We thank Gustaaf Brooijmans for bringing this to our attention.

has had time to oscillate (i.e. samples with a large displacement) from samples in which the decay time is short compared to the oscillation period. These samples would have different dilution factors and could be weighted differently to improve sensitivity. While we have not investigated such advanced techniques in our analysis, we present in Fig. 3.2 a comparison of the transverse decay length for different sources of the muon, illustrating this effect.

Finally, we comment that while our analysis was designed with one of the LHC's all-purpose detectors in mind (i.e. ATLAS and CMS), it is worthwhile to consider the reach of LHCb as we are interested in a precision measurement of b-jets in the forward region. The main distinguishing feature of LHCb is its precision tracker and vertexing system, which allows for a precise reconstruction of hadron level decays. If this could be used to probe the decays of the b-hadrons then it could allow for a substantial reduction in the wrong-sign μ backgrounds and may open up other channels for use in signing the b. However, such a measurement would be challenging as the rates for $b\bar{b}$ production become quite small once one restricts both bs to lie in the forward region. At parton level we find the $b\bar{b}$ rate to be ~ 0.5 pb, yielding an asymmetry of $\sim 3\%$ when requiring only $p_T(b/\bar{b}) > 150$ GeV and $2 < y(b/\bar{b}) < 5$ (the rapidity range for LHCb), with the rate dropping precipitously as cuts on m_{jj} are further applied. Further challenges may also come from employing LHCb to study high-p_T jets that we require, as the detector was primarily designed to study softer objects in a relatively clean environment.

The situation changes somewhat at a 14 TeV LHC, where the parton level rate for $b\bar{b}$ production subject to the above cuts rises to 12 pb, yielding an asymmetry of $\sim 5\%$ before accounting for other sources of background (i.e. gluon splitting, flavor excitation, and b-fakes). Here LHCb might be able to measure the asymmetry in b-production, although

to properly evaluate its potential one would need to perform a more detailed study of its capabilities than we would feel comfortable making. We therefore feel that although it appears that such a measurement would be quite difficult, a more detailed study of LHCb's reach in this channel is probably warranted.

3.5 Conclusions

The CDF and D0 collaborations have both observed an anomalously large asymmetry in $t\bar{t}$ production. While some discrepancies between the two experiments remain to be resolved, the evidence for a large asymmetry seems robust, and if the excess is due to SM effects they must be quite subtle. Many beyond the SM explanations have been put forward to explain the asymmetry, offering various treatments of the many potential quark couplings to new-physics. Previously, Refs. [111, 53] proposed that Tevatron data at CDF and D0 could be used to probe these interactions for bottom and charm quarks. Here we have argued that, through a forward-central asymmetry, the CMS and ATLAS experiments at the LHC are sensitive in the immediate future to whether new-physics interactions generating the asymmetry in $t\bar{t}$ production also affect the bottom quark.

Our results indicate that, with around 10 fb^{-1} of 7 TeV LHC data, the general purpose LHC detectors can probe such new interactions with a sensitivity greater than 2σ. While less sensitive than a Tevatron search with the same amount of data, and while insufficient to discover new physics, such a measurement would still provide useful model-building guidance. However, whether this is feasible depends crucially upon whether the selection cuts required for the measurement are compatible with the trigger menu for the corresponding integrated luminosity. Given the importance of determining whether there are unexpected asymmetries

affecting bottom quark production, we hope that the ATLAS and CMS experiments will investigate this issue carefully, and consider adjusting trigger thresholds if adjustments are indeed necessary.

Chapter 4

Stable Colored Particles R-SUSY Relics or Not?

4.1 Introduction

After decades of anticipation and preparation, the Large Hadron Collider will shortly open the door to TeV-scale physics. This energy range is of great theoretical interest, as it has long been suspected of holding the answers to electroweak symmetry breaking, and the associated naturalness problem [118, 119, 120, 121]. From technicolor [119, 120, 122], to supersymmetry [123] and extra dimensions [124, 125, 126, 127, 128, 129, 130] a great deal of effort has gone into discovering possible solutions to these problems, and determining the associated collider signatures. However, we don't yet know what will appear at the weak scale and we want to be open to the broadest range of possibilities. It is critical to also consider the experimental signatures of other scenarios for new TeV-scale physics, ones that may not easily fit into the known solutions for the various problems of the Standard Model

(SM).

In this chapter, we propose methods to measure both the spin and $SU(3)_C$ color charge of strongly interacting massive particles that are stable on detector timescales. Though most of the detailed analyses have focused on (meta-)stable gluinos or squarks, supersymmetric R-hadrons are just one realization of strongly interacting, stable particle. We will take the most general possible viewpoint, and ask simply about the quantum numbers of the colored state, independent of the model in which it might originate. Examples abound in the literature, including universal extra dimensions [131, 132, 133, 134] that can mimic many features of SUSY models; unusual spectra, such as charged lightest KK-odd modes [135, 136], are also possible and may be a strongly interacting state. More exotic models have also been proposed that would include (meta-)stable colored particles: KK-towers of X and Y grand unified gauge bosons in warped extra-dimensions with GUT-parity [137, 138, 139, 140], long-lived leptoquarks [141], 4^{th} generation quarks [142, 143], mirror fermions [144, 145], perhaps in vector-like generations [146, 147], or related to symmetries stabilizing the dark sector [148]. For a larger list of possible models and particle candidates, see Ref. [149]. In this chapter, we will use "long-lived-colored particle" or 'LLCP' as a generic name for any new stable colored particle.

All these models generate similar signatures in the detector. Many are produced with very large cross-sections, making discovery in early running a possibility. As they are both strongly interacting and stable, they will pass through the entire detector. If the particle hadronizes into charged states, it will deposit energy in the central tracker, electronic and hadronic calorimeters, and be visible in the muon chambers [150, 149]. Thus, such particles will present a striking signature at the LHC, initially appearing as "heavy muons" in events with no

missing p_T (assuming both LLCPs hadronize into charged objects) that would be extremely difficult to replicate by a SM background. Additionally, as will be discussed in greater detail, the LLCPs often undergo nuclear interactions in the detector which rehadronize the particle and allow for the charge to switch sign. This can result in another unique signature, though specialized tracking procedures may be necessary to take full advantage of this. Finally, an alternative search strategy is to look for stopped tracks in the detector volume [151]. Such searches have been carried out at D0 [152], CMS [153], and ATLAS [154].

With discovery a relatively straightforward issue, in this chapter we concern ourselves with the problem of identifying the underlying quantum numbers of the new state. If we are to determine whether a stable $SU(3)_C$-charged particle is truly a gluino, a squark, a UED gluon KK=1 mode, or some other expression of new physics, it will be necessary to measure the LLCP mass, spin, and charge under the SM gauge groups.

Of these, mass is a straightforward measurement: time of flight information will be sufficient to determine the mass to good accuracy [155]. In this work we demonstrate techniques for measuring both the spin and $SU(3)_C$ charge of LLCPs. In Section 4.2, we demonstrate the former measurement; we will show that spin can be determined from the polar angle differential cross-section in LLCP pair-production events. Unlike most proposed new physics events, pair production of LLCPs have almost no missing energy, so this distribution can be reconstructed without ambiguity. Even with the presence of t-channel diagrams, which cause forward peaks in the distribution for all possible spin assignments, sufficient differences remain in the distributions, which allow identification of this critical quantity.

In Section 4.3, we demonstrate techniques to identify, with some limitations, the color charge of new stable particles. In particular, we show that it is possible to distinguish the

production of a stable pair of particles in octet representations of $SU(3)_C$ (*e.g.* gluinos) from production of particle-antiparticle pair in triplet/anti-triplet representations (*e.g.* stops). This method relies on the fundamental asymmetry present in the detectors: they are built from baryons, rather than anti-baryons. As a result, the hadronization of a triplet of $SU(3)_C$ follows a very different path from that of an anti-triplet, leading to a measurable difference in energy deposition.

Perhaps the best known realization of such particles is in supersymmetry, where in some schemes gluinos or squarks can be the lightest (or next to lightest) supersymmetric particle [156, 157, 158, 159, 160]. In this case, the strongly interacting particles are stabilized by an unbroken (or weakly broken if the particles are only meta-stable [161, 162]), R-symmetry. As such, they have become known as R-hadrons [163, 164]. Searches for such particles have been performed at ALEPH [165], CDF [166], and LEP2 [167], and exclude particles with mass less than about $200 - 250$ GeV, depending on the theoretical assumptions made. Searches are planned at both ATLAS [168] and CMS.

The physics in the early Universe may provide significant constraints if these strongly interacting particles are truly stable (or at least have a lifetime much longer than the age of the Universe). Both direct searches for dark matter and searches for anomalously heavy seawater [169] preclude dark matter from having $SU(3)_C$ charge. This places strong limits on the mass of any new stable colored particle; gluinos, for example, can evade cosmological bounds only if their masses are less than about a TeV [156], and seawater tests may lower the allowed mass to ~ 100 GeV.

Of course, at the LHC, a particle needs only live longer than a few dozen nanoseconds to be seen as 'stable.' In this case, the constraints are relaxed and depend on lifetime. Again

specializing to the case of long-lived gluinos, Ref. [170] finds that the SM's successful prediction of nuclear abundances from Big Bang Nucleosynthesis excludes lifetimes greater than 100 seconds (see Ref. [171] for a more-in-depth discussion of hadronic decays in this epoch). Lifetimes up to 10^{13} seconds are excluded, as they would distort the cosmic microwave background, while lifetimes on the order of the age of the Universe are ruled out by observations of the diffuse gamma ray background by EGRET [172]. From this, we conclude that any new colored particles at the LHC must either decay within 100 seconds, or have a lifetime significantly longer than the age of the Universe. We consider such possibilities below.

4.2 LLCP Spin Measurements

Measuring the spin of new particles at the TeV-scale has long been recognized as a critically important task in identifying the underlying theory. While the total cross section may be used as a spin measurement, we are interested in a more reliable and less indirect method. Techniques developed for supersymmetric particles or similar physics (*e.g.* [173, 174, 175, 176, 177, 178, 179, 180, 181, 182]), are not applicable to stable particles. However, we can rely on simpler methods, since the event is fully reconstructible. In particular, measurement of the angular distribution via the differential cross-section with respect to the polar angle θ^* in the center of mass (c.o.m.) frame is sufficient to determine the spin of pair-produced particles. Though the presence in some models of t-channel production tends to produce forward peaks at large values of $|\cos\theta^*|$, enough information remains to make spin measurement possible.

We consider several possible cases: the production of massive triplet/anti-triplet fermions and scalars, as well as octet vectors. The minimal models add only the LLCPs themselves,

in which case new physics Lagrangians are just

$$L_{\text{scalar}} = (D_\mu Q_S)(D^\mu Q_S)^* - M^2 Q_S^* Q_S \tag{4.1}$$

$$L_{\text{spinor}} = i\bar{Q}_F \not{D} Q_F - M\bar{Q}_F Q_F \tag{4.2}$$

$$L_{\text{vector}} = G_{\mu\nu}G^{\mu\nu} - M^2 Q_{V,\mu} Q_V^\mu \tag{4.3}$$

An example of Q_S includes a supersymmetric quark, while the fermion Q_F can be a 4^{th} generation quark, but more generally any triplet fermion representation of Standard Model quantum mnumbers. The octet vectors are realized as $KK = 1$ gluons in UED, though here we have integrated out the $KK = 1$ quarks.

However, in most complete extensions of the SM that contain potential LLCPs, additional new states that can couple to the LLCPs, quarks and/or gluons. We therefore include the addfitional cases of up-type squark R-hadrons with gluino intermediaries, UED up-type $KK = 1$ quarks with heavier $KK = 1$ gluon intermediaries, and $KK = 1$ gluons with heavier up-type $KK = 1$ quark intermediaries.

In all of the models, presence of t-channel diagrams create forward peaks in the $|\cos\theta^*|$ distribution. It is generally held that such distortions make spin determination difficult (see, for example [175]). However, while the scalar and spinor distributions do develop similar peaks at large values of $|\cos\theta^*|$, we show that enough qualitative differences remain to distinguish the various scenarios [183]. However, particular choices of intermediary masses can confuse the issue and make the differential cross sections appear to be degenerate.

The analytic formula for the pair production in proton-proton collisions in each case are straightforward to derive. The relevant Feynman diagrams for quark-antiquark and gluon

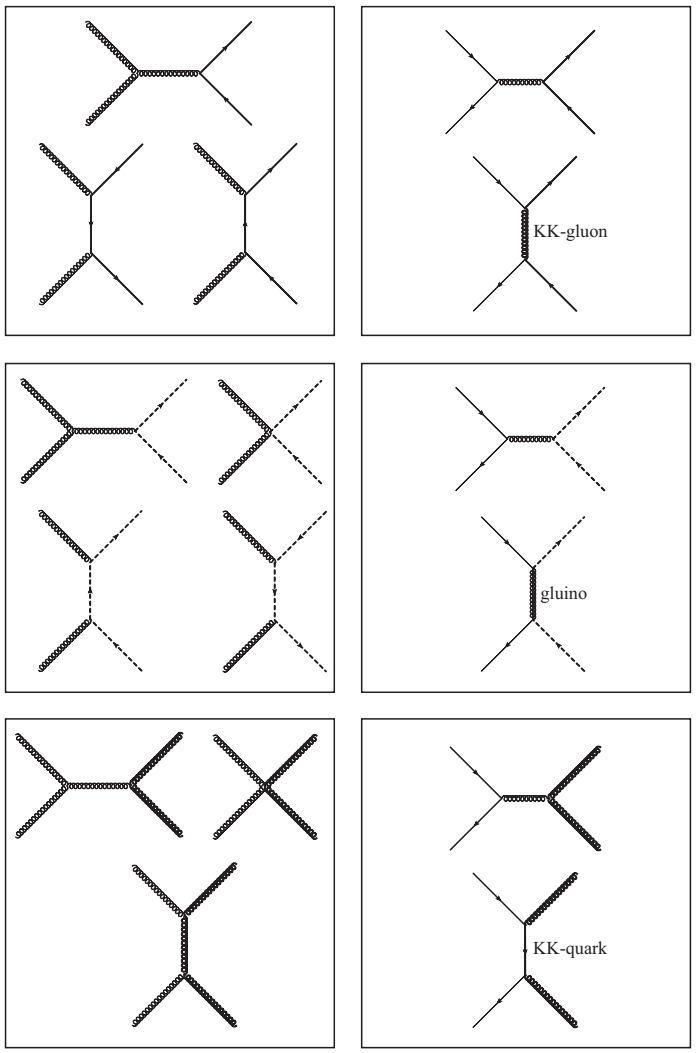

Figure 4.1: Feynman diagrams for the production of spinor (top), scalar (middle), and vector (bottom) LLCPs. Left panels show the diagrams proceeding from gluon initial states, while the quark-antiquark diagrams are on the right. The diagrams requiring the presence of additional heavy states (KK-gluons, -quarks, or gluinos) are labeled.

initial states are shown in Fig. 4.1. For each model, the differential cross-section is convolved with the parton distribution functions (p.d.f.s) using the CTEQ5 p.d.f. [184].

In Fig. 4.2, we show the differential cross-sections after convolution before any acceptance cuts assuming a LHC center of mass energy of $\sqrt{s} = 10$ TeV and a LLCP mass of 500 GeV. For models that have a heavy intermediary (*i.e.* squarks with a heavy gluino, KK-quarks with a heavy KK-gluon, and KK-gluons with a heavy KK-quark), we choose two masses of the heavy state: 700 GeV and 1000 GeV. When no intermediaries are present (or are very heavy), all three spin assignments have significantly different differential cross sections, and so can be distinguished with relative ease. However, in the case of 700 GeV intermediaries, the differential cross sections of fermions and vectors are similar, making discrimination very difficult. In all cases, the cross-sections is normalized to 1.

We next impose the cut $|\eta| < 2.1$ to ensure that both LLCPs end up inside the barrel regions of the ATLAS and CMS detectors, and a cut of $\beta > 0.6$, which is necessary for the heavy muon trigger to identify the correct bunch crossing [168]. Although these cuts tend to remove events at large $|\cos\theta^*|$ (t-channel production diagrams generate forward peaks close to the beam-line) they do not greatly affect our ability to discriminate spin, as the differential cross-section at small values of $|\cos\theta^*|$ has more resolving power. It should be noted that future work by the experiments on the "heavy muon" triggers may allow the η acceptance to be increased, perhaps up to $|\eta| < 2.5$.

Note that the $|\cos\theta^*|$ distribution itself will not be affected by hadronization, as this energy scale $\sim \Lambda_{\rm QCD}$ is much less than the momenta of the particles themselves (~ 100 GeV). As we are considering exclusive LLCP pair production, our sample does not contain additional hard jets – due to radiation of high-p_T gluons for example – which would have sufficient

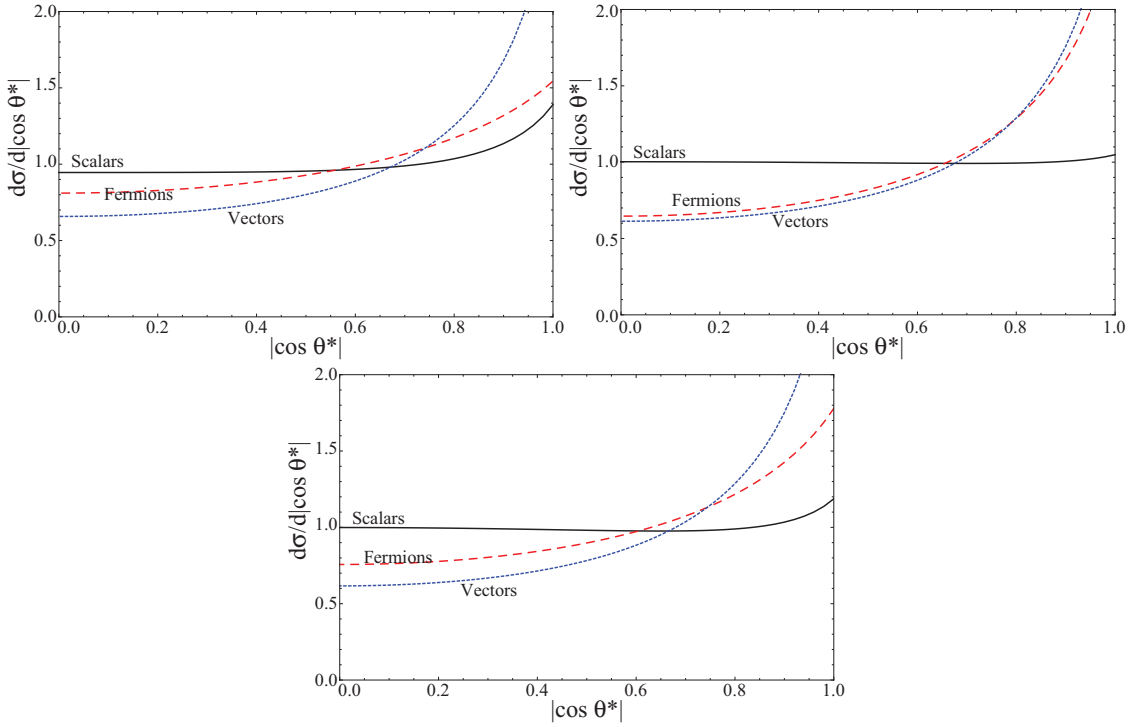

Figure 4.2: The normalized differential cross-sections $\sigma^{-1} d\sigma/d|\cos\theta^*|$ for pair production of 500 GeV LLCPs in pp collisions at $\sqrt{s} = 10$ TeV. No cut on the pseudo-rapidity or velocity β of each LLCP is applied. Left: minimal scalars, fermions and vectors, as introduced in Eqs. (4.1)-(4.3). Right and Center: up-type squarks with gluino intermediaries, up-type $KK = 1$ quarks with $KK = 1$ gluon intermediaries. The intermediary mass is 700 GeV for the upper right, and 1000 GeV for the lower center plot.

Table 4.1: Total cross-section assuming $\sqrt{s} = 10$ TeV and LLCP mass of 500 GeV after $|\eta| < 2.1$ and $\beta > 0.6$ cuts. Heavy intermediary particles are chosen to be 700 GeV or 1000 GeV (see text).

Model	Cross-section (fb) after cuts
Minimal scalars	18
Minimal spinors	130
Minimal vectors	1.3×10^4
Up squarks with 700 GeV gluinos	29
$KK = 1$ up quarks with 700 GeV $KK = 1$ gluons	340
$KK = 1$ gluons with 700 GeV $KK = 1$ quarks	1.2×10^4
Up squarks with 1000 GeV gluinos	24
$KK = 1$ up quarks with 1000 GeV $KK = 1$ gluons	210
$KK = 1$ gluons with 1000 GeV $KK = 1$ quarks	1.3×10^4

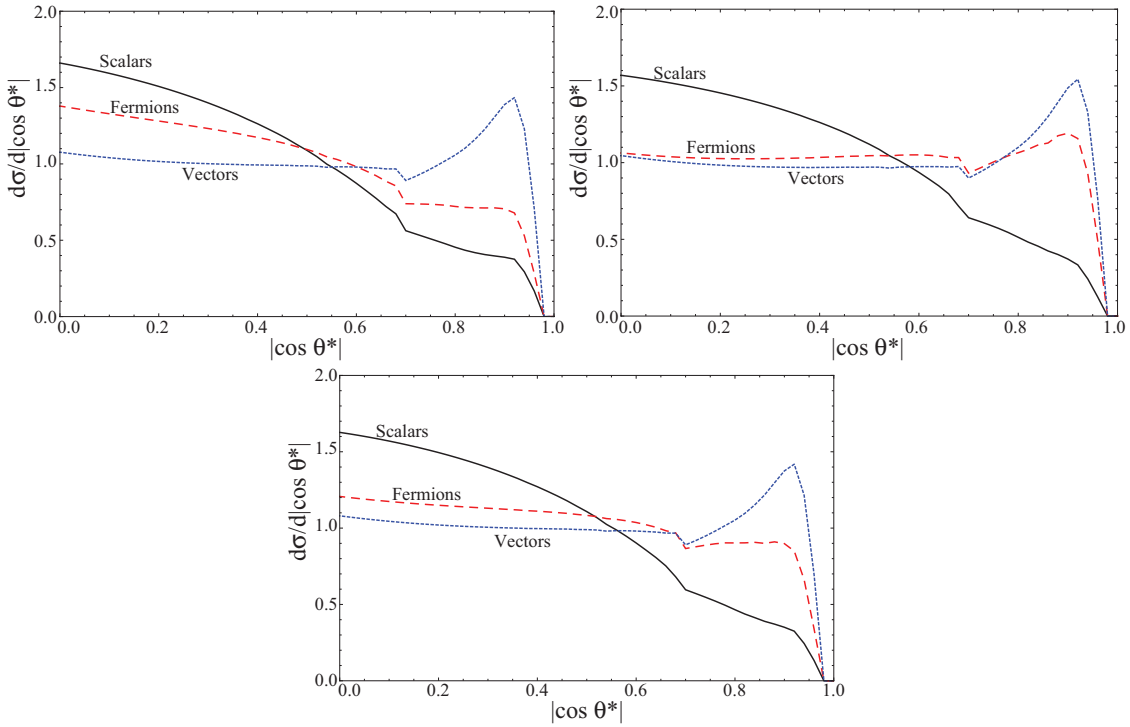

Figure 4.3: The normalized differential cross-section $\sigma^{-1} d\sigma/d|\cos\theta^*|$ for pair production of 500 GeV LLCPs in pp collisions at $\sqrt{s} = 10$ TeV, requiring that both LLCPs are produced in the pseudo-rapidity range $|\eta| < 2.1$ and have $\beta > 0.6$. Left: minimal scalars, fermions and vectors, as introduced in Eqs. (4.1)-(4.3). Right and Center: up-type squarks with gluino intermediaries, up-type $KK = 1$ quarks with $KK = 1$ gluon intermediaries. The intermediary mass is 700 GeV for the upper right, and 1000 GeV for the lower center plot. Numerical instabilities from the application of the c.o.m. η cuts distort the curves around $|\cos\theta^*| = 0.7$.

energy to significantly affect the differential cross section.

Requiring both LLCPs to be produced with $|\eta| < 2.1$ and $\beta > 0.6$, we present the resulting total cross sections in Table 4.1 and the differential cross sections are displayed in Fig. 4.3. In most cases, the various models have significantly different distributions. We note that if we do a more model-dependent analysis and allow intermediate states of varying mass, the fermion and vector cases will be degenerate for certain parameter choices. Of course, as the intermediary mass increases, the spectrum will revert to the 'minimal' case,

where the differential cross sections differ significantly. We estimate that distinguishing these differential cross sections may require ~ 5 bins in $|\cos\theta^*|$ with ~ 1000 events per bin. Lacking a full detector simulation, we estimate the efficiencies for production and detection of a charged-LLCP pair as $O(0.1)$. Combined with our assumption of 5000 binned events, the production cross-sections (which are very large in the fermion and vector cases, Table 4.1) imply that a spin measurement should be possible with integrated luminosity of $O(1\text{fb}^{-1})$ for the vector case, $O(100\text{fb}^{-1})$ for the fermions, and $O(1000\text{fb}^{-1})$ in the scalar case.

4.3 LLCP Color Charge Measurement

In addition to spin determination, we would want to know the color charge of LLCPs as this provides key insights into the particle's identity and the associated underlying theory. Although some information could in principle be determined by measuring the total cross-section, we are again interested in a more direct handle on this quantum number. In this section, we demonstrate a method to distinguish particles in a triplet/anti-triplet ($\mathbf{3}/\bar{\mathbf{3}}$) representation of $SU(3)_C$ from particles in an octet ($\mathbf{8}$). Further work is required to extend this method to representations other than the fundamental and adjoint.

The key element of this technique is the inherent asymmetry of detectors, built as they are of matter rather than antimatter. During its transit of the detector, an LLCP will undergo several nuclear interactions with the detector material, each of which has a significant probability of causing the LLCP to rehadronize by exchanging light colored particles with the nucleon [185]. This introduces an asymmetry between LLCPs in a $\mathbf{3}$ representation versus ones in $\bar{\mathbf{3}}$: the former is interacting with many particles in the same representation as itself, while the latter sees essentially no light anti-quarks with which to hadronize. That means

that after passing through the experiment the final mix of hadronized states for triplet states would significantly differ from that of antitriplets. As we shall show, the preferred state of triplet LLCPs is an LLCP-baryon, that of an antitriplet LLCP is a meson.

The scattering of an LLCP with matter proceeds through the interaction of the light quark/gluon content with the target nucleus, as the probability of interaction between a heavy parton (the LLCP) and a quark at rest is proportional to the inverse square of the parton mass. In this context, the massive particle can be pictured as a stable non-interacting heavy parton, surrounded by a cloud of light quarks/gluons that scatter with the detector material. The cloud carries only a fraction of the total energy, and the mass of the nucleon is comparable to the total energy in the center of mass frame for the scattering. Interactions of LLCP-mesons that undergo a baryon number exchange (ending with the proton or neutron being destroyed) are kinematically favored over events that do not have such an exchange [186]. Briefly, this is because the rest mass of the nucleon is about the same as the total available energy in the scattering. As a result, having a nucleon in the final state consumes nearly all of the available energy. For example, the phase space for a LLCP-meson + nucleon scattering to go into a LLCP-baryon + pions is much larger than for a LLCP-meson to LLCP-meson event. An LLCP-meson will therefore preferentially undergo a baryon-exchange scattering with a nucleon, resulting in an LLCP-baryon and a shower of light mesons.

Once an LLCP-baryon is produced, the phase space to scatter back into an LLCP-meson is very small, as this requires the creation of a SM baryon which is heavy compared to the available energy in the scattering. On the other hand, an anti-triplet meson cannot undergo (anti-)baryon exchange to convert into an LLCP-anti-baryon; and if hadronized as a $\overline{(LLCP)}_3\bar{q}\bar{q}$, the preferred scattering is into a $\overline{(LLCP)}_3 q$-meson, destroying the nucleon in

the process. This result is fairly robust and depends purely on phase space arguments and the relatively small mass splitting between LLCP-baryons and LLCP-mesons.

In a similar fashion to the re-hadronization process, energy deposition in the detector differs between triplet and anti-triplet LLCPs. In a greatly simplified model, the "black disk approximation," each light quark or gluon in the bound state contributes 12 mb to the nuclear scattering cross-section [187]. Ignoring electromagnetic interactions, the LLCP triplet $(LLCP)_3$, hadronized as it is with two light quarks, on average scatters twice as often as the $\overline{(LLCP)}_3$-meson, and thus deposits twice as much energy. On the other hand, both octet LLCPs are produced in the same representation and so a pair of them will leave, on average, equal amounts of energy. Assuming that LLCPs will be pair produced at the LHC (since this is typically the case in theories containing such particles, this assumption is not overly restrictive), one can straightforwardly probe the color quantum number of the LLCP by looking for an asymmetry between energy deposition of the two tracks in the hadronic calorimeter.

The black disk approximation is useful for illustrative purposes, but is obviously insufficient for detailed calculations. In Ref. [188], a more sophisticated scattering model based on Regge phenomenology and low-energy hadron-hadron data was developed. As expected, the LLCP-baryon scattering cross-section is about twice as large as that of LLCP-mesons, owning to the additional light quark. The cross-section of LLCP-anti-baryons, due to a dominant annihilation process with baryons at low energies, is also larger than that of LLCP-baryons. Similarly, the $(LLCP)_3$-meson have a larger cross-section than $\overline{(LLCP)}_3$-meson, since baryon-exchange processes are only permitted for LLCPs containing light antiquarks. The $(LLCP)_8$-meson and $(LLCP)_8$-gluon cross-sections are taken to be the sum

of the $(LLCP)_3$ and $\overline{(LLCP)}_3$-meson, while that of $(LLCP)_8$-baryon is 50% larger than the corresponding $(LLCP)_3$-baryon cross-section. We use the GEANT4 [189] implementation of this model as described in Refs. [185, 190]. This also includes electromagnetic energy losses through ionization, in addition to energy loss through nuclear scattering. As both LLCP-baryons and LLCP-mesons can be electrically charged, we expect that the presence of electromagnetic deposits will serve to shift both energy deposition curves to higher values.

We illustrate our idea using particles in the triplet/anti-triplet representation with charge $\pm 2/3$ (*e.g.* top squarks: $(LLCP)_3 = \tilde{t}, \overline{(LLCP)}_3 = \bar{\tilde{t}}$) and neutral particles in the octet representation (*e.g.* gluinos: $(LLCP)_8 = \tilde{g}$). The charged triplets can form LLCP-mesons with charge +1 ($(LLCP)_3\bar{d}$), zero ($(LLCP)_3\bar{u}$ and $\overline{(LLCP)}_3 u$) or −1 ($\overline{(LLCP)}_3 d$), as well as charged LLCP-baryons (LLCP-anti-baryons), the lightest being $(LLCP)_3 ud$ ($\overline{(LLCP)}_3 \bar{u}\bar{d}$). Higher spin LLCP-baryons (LLCP-anti-baryons) are expected to decay to the ground state before interacting with the detector. The mass spectrum adopted is similar to the one used in Refs. [191, 186], in which the lightest LLCP-baryon is ~ 0.3 GeV heavier than the massive particle, and the lightest LLCP-meson is ~ 0.7 GeV heavier. These results are consistent with calculations using different approaches [192, 193, 194, 195, 196]. The two neutral mesons may allow the triplet LLCP-hadron to mix into the anti-triplet. This might occur via chargino/W exchange in SUSY models. Since the level of mixing is model dependent, we consider two limiting cases: no mixing and maximal mixing, in which a neutral state has a 50% probability in oscillating to its anti-particle. This corresponds to infinite and zero oscillation lengths, respectively. The lightest hadrons formed by the neutral octet include LLCP-mesons with charge +1 ($(LLCP)_8 u\bar{d}$), zero ($(LLCP)_8 q\bar{q}$ with $q = u, d$) or −1 ($(LLCP)_8 \bar{u}d$), the LLCP-glueball ($(LLCP)_8 g$) and the LLCP-baryon ($(LLCP)_8 uds$). Although their spectrum is

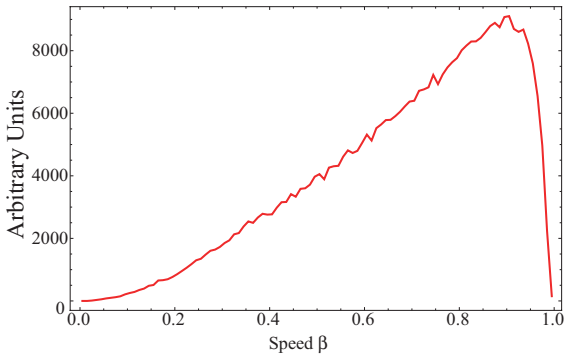

Figure 4.4: The initial velocity distributions of the LLCPs. These distributions are obtained from MadGraph [113] simulations of pair-produced 500 GeV particles at the LHC with $\sqrt{s} = 10$ TeV. This quantity depends mainly on the production kinematics, with only minor differences between the various spin models considered in Section 4.2. We require $\beta > 0.6$ to simulate the heavy muon trigger as planned by ATLAS [168].

not as well understood as the $(LLCP)_3$ examples, it is expected that the $(LLCP)_8$-mesons ($(LLCP)_8 q\bar{q}, q = u, d$, $(LLCP)_8 u\bar{d}$, *etc*) will be closely degenerate, and similar in mass to the lightest LLCP-baryon: $(LLCP)_8 uds$ (see Ref. [190] and references therein).

The passage of LLCPs through matter is analyzed by firing LLCP beams initially composed of 100% of either $(LLCP)_3\bar{d}$-mesons, $\overline{(LLCP)}_3 d$-mesons, $(LLCP)_3 ud$-baryons, $\overline{(LLCP)}_3 \bar{u}\bar{d}$-anti-baryons, $(LLCP)_8 u\bar{d}$ or $(LLCP)_8 \bar{u}d$-mesons into a block of iron two meters thick (the approximate depth of material constituting the central detectors at ATLAS and CMS). Only charged initial states are considered as LLCPs that hadronize into neutral objects will leave a signal in the calorimeter only and might be difficult to identify. The initial β distributions of the LLCPs are taken to be that of 500 GeV particles pair produced at the LHC with $\sqrt{s} = 10$ TeV, as shown in Fig. 4.4. To simulate the effect of the heavy muon trigger [168], we apply a cut of $\beta > 0.6$ on this distribution.

The number of nuclear scatterings for different LLCP beams are displayed in Fig. 4.5. As expected, the beam of $\overline{(LLCP)}_3 d$-mesons has significantly fewer interactions than the beams

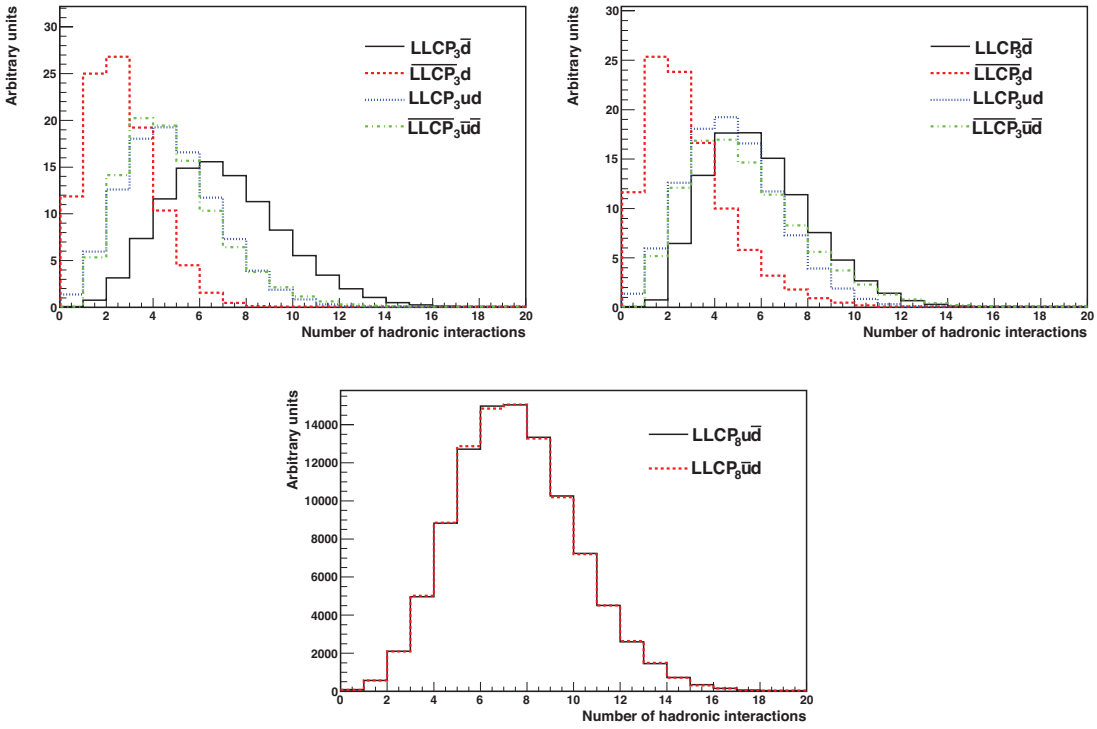

Figure 4.5: The number of hadronic interactions for beams of LLCPs traversing two meters of iron, including the effects of rehadronization after a scattering. The labeling indicates the initial composition of the beam. Top-left panel has no mixing for the neutral LLCP-mesons states, while the top-right panel include maximal mixing.

of $(LLCP)_3\bar{d}$-mesons, $(LLCP)_3$-baryons or $(LLCP)_8$-hadrons. Since $\overline{(LLCP)}_3 d$ contains an $\overline{(LLCP)}_3$, it cannot rehadronize as a LLCP-baryon, whereas $(LLCP)_3\bar{d}$ contains $(LLCP)_3$, which tends to rehadonize as a $(LLCP)_3$-baryon with a larger nuclear cross-section. The mixing affects mainly $(LLCP)_3\bar{d}$-mesons, since they have a larger probability of rehadronizing to a neutral state compared to $\overline{(LLCP)}_3 d$, while $(LLCP)_3$-baryons do not undergo significant rehadronization through the detector. Annihilation of $(LLCP)_3$-anti-baryons produces roughly equal amount of charged and neutral $\overline{(LLCP)}_3$-mesons, reducing the sensitivity to mixing.

In Fig. 4.6, we show the composition of the beams as they pass through the iron, with and without mixing between $(LLCP)_3$ and $\overline{(LLCP)}_3$. As expected, the beam of $(LLCP)_3$-mesons quickly rehadronizes into baryons, while the $\overline{(LLCP)}_3$-mesons remains stable. Mixing in the neutral meson allows the $\overline{(LLCP)}_3$ beams to develop a small component of LLCP-baryons, but this contribution remains subdominant. We also note that a non-negligible fraction of LLCP-hadrons can undergo charge flips, moving from a positively charged state to a negative one, both in the triplet and octet representations.

While this provides a signature that is unique to LLCPs, it will certainly complicate track fitting procedures and might be missed in the early running of the LHC. The beam rehadonization simulations indicate that many events will not undergo such sign flips. As these events are not plagued by as many tracking issues, it is these events that we concentrate on in this chapter.

The total energy deposited in the detector for several charged LLCPs is shown in Fig. 4.7 and exhibits a similar asymmetry. The $(LLCP)_3$-hadrons leave on average more energy than the $\overline{(LLCP)}_3$-hadrons, regardless of the initial hadronization. As outlined above, the mixing affects mainly $(LLCP)_3\bar{d}$-mesons, broadening the corresponding distribution. But even with maximal mixing, a significant difference remains. On the other hand, charged $(LLCP)_8$-mesons have similar hadronization schemes and deposit almost equal amount of energy. In pair-production events, the ratio of energy deposited by each track will thus be close to unity, while in triplet/anti-triplet production, a clear asymmetry will be present.

As there is some uncertainty in the hadronic cross section of LLCPs, in Fig. 4.8 we plot the total energy loss through two meters of iron of LLCPs with maximal mixing when the hadronic cross section is allowed to vary by $\pm 50\%$. The electromagnetic cross section

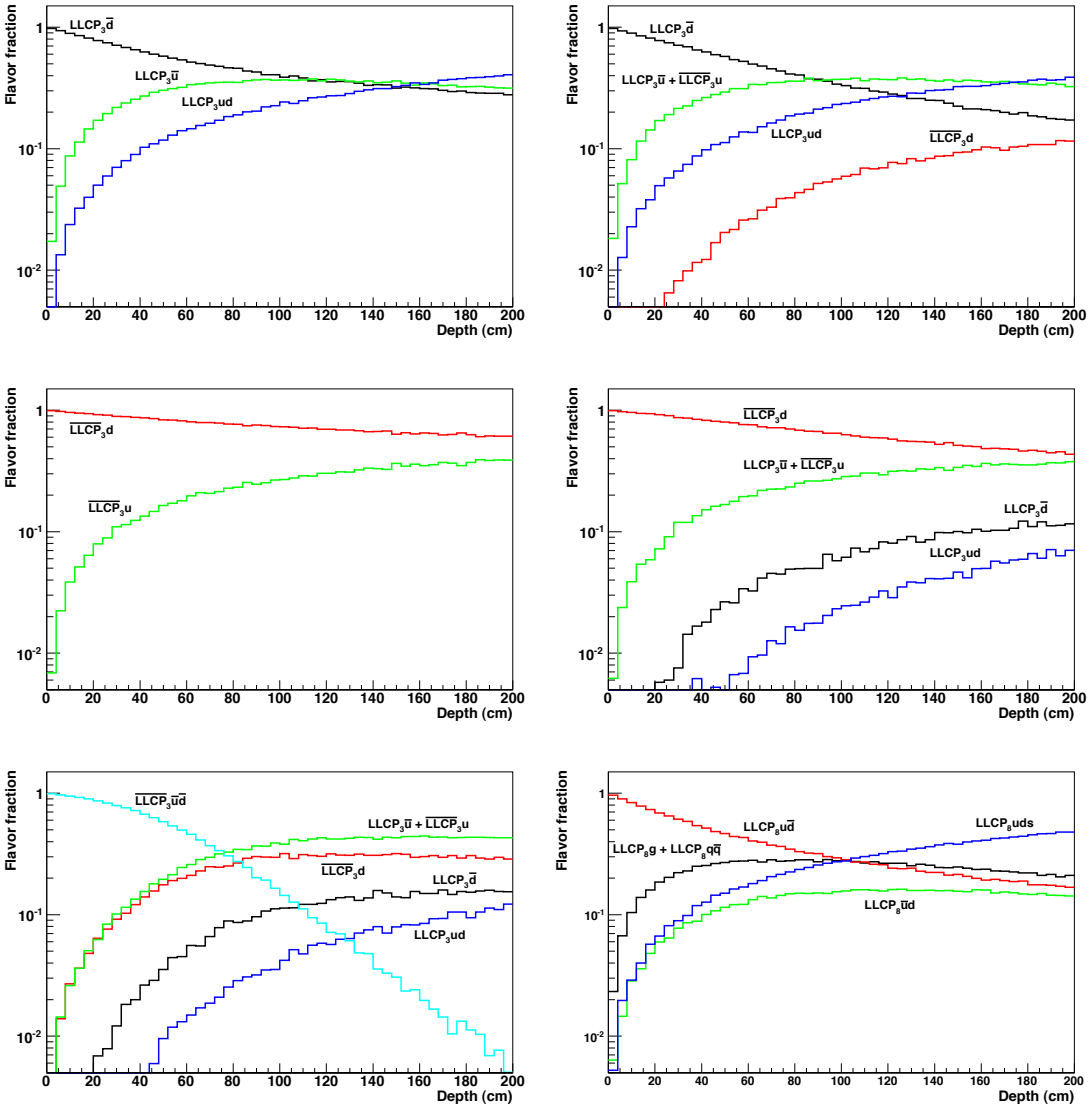

Figure 4.6: The composition of each LLCP beam as a function of distance traveled through iron, assuming an initial beam composed of a pure $(LLCP)_3\bar{d}$ with zero mixing (top left), $(LLCP)_3\bar{d}$ with maximal mixing (top right), $\overline{(LLCP)}_3d$ with zero mixing (middle left), $\overline{(LLCP)}_3d$ with maximal mixing (middle right), $\overline{(LLCP)}_3\bar{u}\bar{d}$-anti-baryons (bottom left), and $(LLCP)_8u\bar{d}$-mesons (bottom right). Note that $(LLCP)_3$-baryons are not shown; as the preferred state for hadronization, they do not undergo significant rehadronization through the detector.

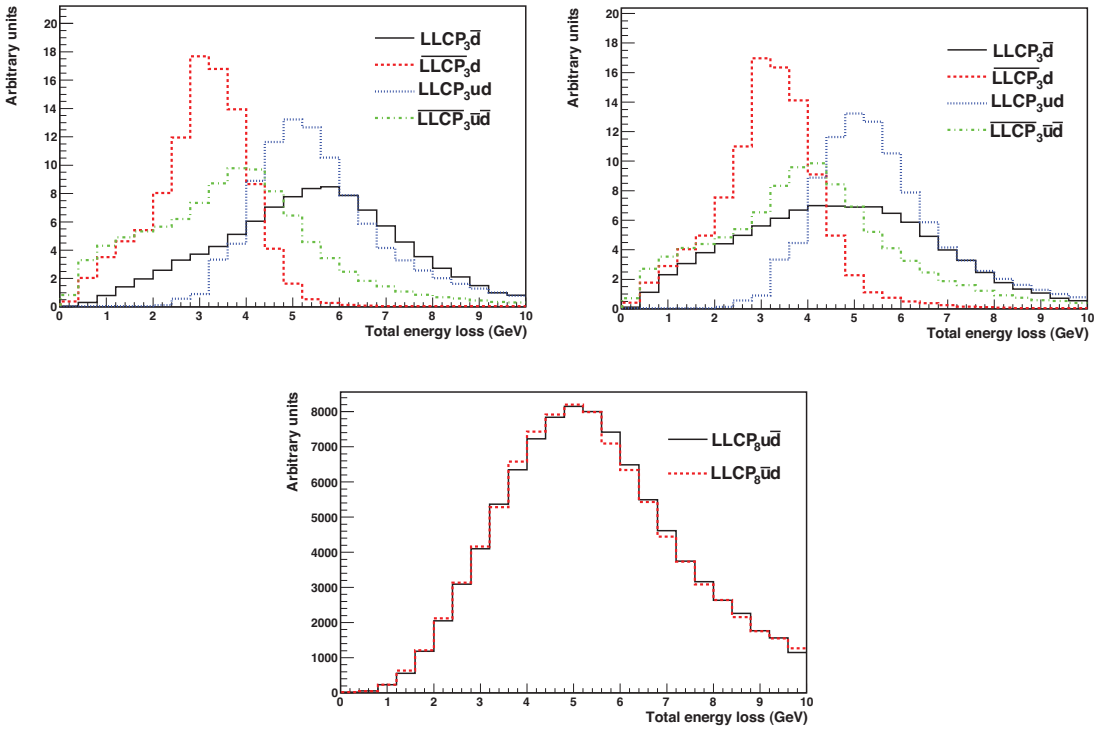

Figure 4.7: Total energy loss through two meters of iron of LLCP beams initially composed of pure $(LLCP)_3$ and $\overline{(LLCP)}_3$ states assuming no mixing (top left) or maximal mixing (top right). The octet states are shown in the lower panel. Labeling indicates the initial composition of each beam.

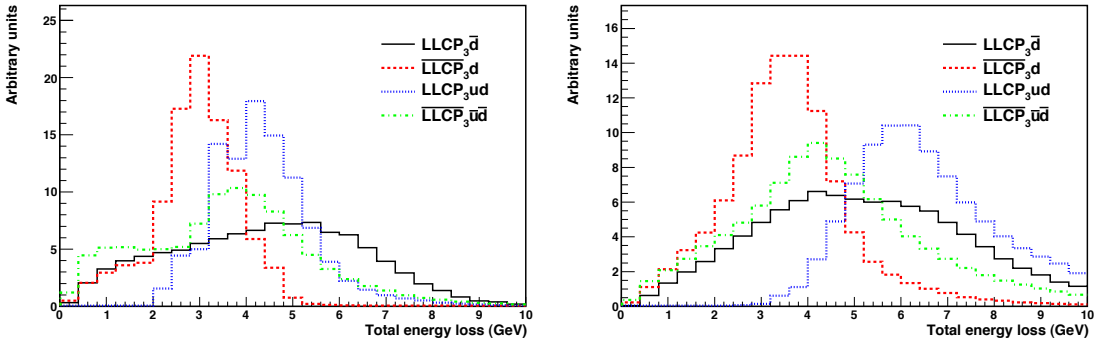

Figure 4.8: Total energy loss through two meters of iron of LLCP beams initially composed of pure $(LLCP)_3$ and $\overline{(LLCP)_3}$ states assuming maximal mixing and a cross section that is 50% larger (left) and 50% smaller (right) than the model implemented in [185, 190].

is held constant. As can be seen, even when the hadronic contribution is decreased by half, the $\overline{(LLCP)_3}$ anti-baryons still deposit considerably less energy than the $(LLCP)_3$-baryons. From this, we conclude that our color charge measurement is robust with regards to uncertainties in the hadronic cross section.

4.4 Conclusions

LLCPs provide an easily recognizable, unique signature at the LHC experiments. The presence of heavy, charged particles with low β in the muon chamber is a signal that would be difficult to replicate in the SM. Furthermore, as demonstrated in Fig. 4.6, rehadronization in the detector can allow charge flips, which would constitute a smoking gun of LLCP-hadron production. We should nonetheless keep in mind that only a fraction of states will undergo charge flips. With large luminosity (varying between $1 - 1000$ fb^{-1} depending on the spin of the LLCP), a significant number of events will be accessible by standard track-fitting and analysis techniques. It is these events that we have considered in this analysis of spin and

color measurements.

Strongly interacting, stable particles are by no means unique to supersymmetric theories. If discovered, measurements of their fundamental properties: mass, spin, and charge, will be essential to unraveling the degeneracy among possible states. In this chapter we demonstrated two experimentally viable measurements to determine the spin and color charge of LLCPs.

To measure spin, we take advantage of the fact that events involving the pair creation of charged LLCPs can be fully reconstructed. As many hadronized states are neutral states, we do not expect every event to contain two visible tracks. However, as seen in Table 4.1, the production cross sections are, in most cases, large enough so that hadronization into neutral states should not qualitatively reduce the experimental sensitivity.

From the two charged tracks, we can reconstruct the center of mass frame of each event, and the polar opening angle of the pair production. In Section 4.2, we demonstrated that the differential cross section with respect to this angle contains sufficient information to determine the spin of the LLCPs. There is some degeneracy between spin states when heavier intermediaries (*i.e.* gluinos or KK modes) are included. However, in order for these states to significantly affect the measurement, they must be fairly light, and so they should be detectable at the LHC, for example in LLCP plus missing E_T channel.

The measurement of the color charge takes advantage of the rehadronization of the LLCPs inside the detectors. As protons and neutrons contain very few $SU(3)_C$-anti-triplets compared to triplets, there is an asymmetry in how an LLCP in a **3** representation will rehadronize compared to a $\bar{\mathbf{3}}$. This asymmetry causes the triplet to preferentially hadronize into a baryon, while its anti-partner tends to hadronize into a meson. As the mesons undergo

nuclear scatterings less often than the LLCP-baryons, the difference between the **3** and the $\bar{\mathbf{3}}$ can be experimentally accessed. Using a GEANT4 implementation of the scattering of LLCPs with iron nuclei, we have shown that this asymmetry should be measurable via the energy deposited in the ATLAS and CMS calorimeters. In comparison, octet pairs of LLCPs will not have statistically significant differences between the two tracks, as they will tend to hadronize identically.

It is our expectation that we will be able to distinguish chiral from vector representations, as we have demonstrated with the specific examples of chiral **3** and vector **8** representations. Determining which representation within each set (*e.g.* **3** from **6**) will require a more detailed investigation of the energy deposition patterns and a better understanding of the hadronization schemes of representations beyond the adjoint and fundamental. Such a study is beyond the scope of this chapter.

Chapter 5

Distinguishing spins at the LHC using bound state signals

5.1 Introduction

Studying the new particles that will be produced at the LHC will likely be a non-trivial task. In many scenarios the particles of the new sector are charged under a new parity that makes the lightest such particle a dark matter candidate. The new particles will then predominantly be produced in pairs, giving multiple decay products some of which will be undetectable (including at least two dark matter particles). The reconstruction of such events with many objects and missing energy in the final states will be complicated and often ambiguous. It may therefore be useful to also look at signals arising from the near-threshold formation and annihilation of QCD bound states of the new particles. The bound states behave as resonances which annihilate primarily into just two particles (or jets) and no missing energy, so the analysis and the interpretation of the signal are much more straight-

forward than in the more conventional channels. In particular, detecting the peak in the invariant mass distribution of any of the possible annihilation channels provides a direct measurement of the particle mass. The disadvantages of the bound state signals are their relatively small cross sections and the fact that the dominant annihilation mode is into dijets (which have large QCD background), with only small branching ratios for annihilation into cleaner signals such as $\gamma\gamma$. However, whenever the bound state signals are observable, they can provide an entirely independent method for characterizing or verifying the properties of the new particles.

In this chapter we study how the spins of the new particles are reflected in the properties of their bound states and the resulting signals at the LHC. As an example, we compare the bound states of the level-1 Kaluza-Klein (KK) modes in the universal extra dimensions model (UED) with bound states of the superpartners in the minimal supersymmetric extension of the standard model (MSSM). In both scenarios, the new particles are charged in the same way under the standard model gauge groups, and the masses of the particles are to a large extent free parameters. The fundamental difference between the two scenarios is the spin of the new particles. The KK modes in UED have the same spins as the standard model particles (which are the zero modes), while the spins of the superpartners in MSSM are different. However, the collider signatures of the decay products of a pair of level-1 KK modes of UED and a pair of analogous MSSM superpartners are unfortunately very similar and it is often challenging to determine the spin [176, 197, 174, 198, 199, 200, 177, 201, 202, 203, 204, 205, 206]. It is therefore interesting to study whether and when the bound state annihilation signals can give information about the spin.

While much is known about bound states of the MSSM particles (see [207] and references

therein), the bound states in UED models have not been explored, with the exception of bound states of KK quarks in the context of a lepton collider [208, 209]. Here we will study the various possible bound states of colored particles of UED in the context of the LHC and compare them to the corresponding bound states in the MSSM. We will see as we go along that once the spin of the particle is specified many of the results are largely model-independent since they are determined by gauge interactions. Thus our comparisons between particles of different spins (in the same color representation) will hold even more generally.

We start in section 5.2 by discussing the UED model in the context of our study and reviewing the general formalism for bound state computations. In sections 5.3–5.5 we present the production cross sections, branching ratios and angular distributions for the various bound states and compare signals obtained from UED and MSSM. In section 5.6 we simulate the bound state signals and the relevant backgrounds in the dijet, $b\bar{b}$, $t\bar{t}$, $\gamma\gamma$ and e^+e^- channels and estimate the LHC reach for the various cases. We summarize our conclusions in section 5.7.

5.2 Setup

5.2.1 Particle spectrum of UED

In the simplest UED scenario [131] (for a review, see [210]), all the standard model fields are propagating in a single extra dimension of size $R \sim \text{TeV}^{-1}$. The right- and left-handed standard model fermions are represented by separate fields in 5 dimensions, and each has two chiralities when reduced to 4 dimensions. To restrict each fermion zero-mode to a single chirality, the extra dimension is assumed to be an $S^1/\mathbb{Z}_2$ orbifold. The zero modes of the

unwanted chiralities of the fermions and the 5th components of the gauge fields are then projected out by declaring them to be odd under the $\mathbb{Z}_2$ orbifold symmetry. The KK modes of the right- and left-handed quarks will be denoted by $q_R^\star$ and $q_L^\star$, or collectively by $q^\star$. We will refer to $q_R^\star$ and $q_L^\star$ as right- and left-handed KK quarks, even though each one of them is a full Dirac fermion. (Similarly, we will refer to the MSSM partners of the right- and left-handed quarks, as right- and left-handed squarks.) All the standard model interactions are contained in the bulk Lagrangian. Since in 5 dimensions the gauge, Yukawa and quartic-Higgs couplings have negative mass dimension, this is an effective theory with a UV cutoff Λ which is assumed to be above the compactification scale: $\Lambda > 1/R$.

In the 4-dimensional description, the theory contains towers of KK modes for each standard model particle, with the mass of the n-th mode given (at tree level) by

$$m_n^2 = \frac{n^2}{R^2} + m_0^2 \tag{5.2.1}$$

where m_0 is the mass of the zero mode (that is the standard model particle itself). As a result, all the KK modes at a particular level n are approximately degenerate, with masses ordered like in the standard model. Loop corrections shift the masses [211, 133], and the resulting spectrum of the first KK level has the KK gluon as the heaviest particle, followed by the KK quarks, and then the KK excitations of the electroweak gauge bosons, the Higgs, and the leptons. The lightest KK particle (LKP), which is typically one of the neutral KK gauge bosons, is a dark matter candidate [212, 213]. At tree level, the LKP is stable because of momentum conservation in the extra dimension. When loops are taken into account it remains stable because the theory retains KK parity under which odd-n modes are charged. The KK parity also prevents tree-level contributions to the electroweak observables, thus

allowing a compactification scale $1/R$ as low as a few hundred GeV. For our purposes it is important that due to KK parity the level-1 KK particles will be produced in pairs, and thus they can form bound states.

In general, the theory also includes boundary terms (on the orbifold fixed points) whose coefficients are free parameters. The boundary terms can be assumed to be symmetric under the interchange of the two orbifold fixed points, and then the theory still preserves KK parity. However, the mass spectrum of the KK modes can be affected dramatically. Even if boundary terms are absent at a particular scale, they are generated by the renormalization group running [214, 211, 133], and the resulting corrections to the masses are of the order of the loop corrections. The spectra of [211, 133] described above were obtained with the simplifying assumption that the coefficients of the boundary terms vanish at a specific cutoff scale. However, as has been shown in [215] for the case of the gauge kinetic term, even when the coefficient of the boundary term is not much larger than the expectation from naïve dimensional analysis, there is a large effect on the spectrum of the KK modes. Similarly, the effects of boundary kinetic and mass terms for a massive scalar field have been analyzed in [216], where the results were applied to the electroweak sector and it was found that the identity of the LKP was sensitive to the boundary terms.

In both UED and MSSM, annihilation may or may not be the dominant decay mode of the various bound states, depending on the intrinsic decay rates of the constituent particles, which in turn depend on the mass spectrum of the model. Since the theoretical and experimental constraints on the possible mass spectra are a question that is decoupled from the bound state analysis, we will leave it out of the scope of this chapter. We will assume that the bound states decay predominantly by annihilation, but the reader should remember

that if the constituent particles are not sufficiently long-lived, the cross sections will need to be multiplied by appropriate branching ratios based on the annihilation rates that we compute here and the model-dependent single-particle decay rates. Note, however, that annihilation branching ratios close to 1 are not implausible. In particular, in the MSSM there exist various motivated scenarios in which this happens to be true for the gluinonium [207] or the stoponium [217]. Or looking at this from a different perspective, the observation or non-observation of bound state signals can give us certain information about the spectrum of the model.

In UED, the spectrum of the level-1 KK modes plays a crucial role in determining which of them are sufficiently long-lived for their bound states to decay by annihilation rather than by the decays of the constituent particles. If the assumption of [211, 133] that the boundary terms vanish at the UV cutoff were true, the KK gluon would have strong two-body decays into a KK quark and an antiquark, and the KK quarks could decay electroweakly into a KK electroweak gauge boson and a quark. In this case, similarly to what happens in much of the parameter space of the MSSM [207], the branching ratios for annihilation will be small. However, we believe (although without constructing explicit examples) that the presence of boundary terms can change the spectrum in ways that would make these decays kinematically forbidden for some of the particles.

For example, if the KK gluon $g^\star$ becomes lighter than the KK quarks $q^\star$, its 2-body decays will be replaced by 3-body decays into a KK electroweak gauge boson, a quark and an antiquark through diagrams involving an off-shell KK quark, a process suppressed by the electroweak coupling and the KK quark mass. This is analogous to the decay of the gluino into a neutralino, quark and antiquark in MSSM scenarios with squarks heavier than the

gluino, which easily makes the gluino sufficiently stable for our purposes [207]. Similarly to the case of the gluino, there is no need for an unnaturally large gap between the KK gluon and KK quark masses in order for the annihilation to dominate. For example, suppose that the dominant decay process is $g^\star \to q\bar{q}B^\star$, where $B^\star$ is the KK hypercharge gauge boson. Then the rate is

$$\Gamma_{g^\star} \simeq \frac{11}{45\pi}\,\alpha_s\,\frac{\alpha}{\cos^2\theta_W}\left(1-\frac{m_{B^\star}}{m_{g^\star}}\right)^5\left(\frac{m_{g^\star}}{m_{q^\star}}\right)^4 m_{g^\star} \sim 10^{-4}\left(1-\frac{m_{B^\star}}{m_{g^\star}}\right)^5\left(\frac{m_{g^\star}}{m_{q^\star}}\right)^4 m_{g^\star} \tag{5.2.2}$$

where for simplicity we assumed $m_{q^\star} \gg m_{g^\star} \approx m_{B^\star}$.[1] On the other hand, the bound state annihilation rates are

$$\Gamma_{\text{annih}} \sim \alpha_s^5\, m_{g^\star} \sim 10^{-5}\, m_{g^\star} \tag{5.2.3}$$

which can easily dominate over $2\Gamma_{g^\star}$, especially when we include the numerical prefactors that appear in the exact expressions for Γ_{annih} (see appendix A.1), which are as large as $O\,(100)$ for color-singlet bound states, primarily due to multiple powers of color factors.

The collider signatures of the 3-body decays of the KK gluon or gluino have been studied in [202] in an attempt to distinguish between UED and MSSM. One of the goals of the present chapter is to find out to what extent detecting the annihilation decays of KK gluonia (which are bound states of two KK gluons) compared to gluinonia (bound states of two gluinos) can provide an additional method for distinguishing between UED and MSSM and determining the properties of the underlying particles. While gluinonia have been studied extensively in the literature, our paper is the first study of KK gluonia.

Another object of our study is KK-quarkonia, which are KK quark-KK antiquark bound

[1]The assumption $m_{q^\star} \gg m_{g^\star}$ is not essential for the validity of this estimate. We have checked that for $m_{q^\star} = 2m_{g^\star}$, for example, the exact result differs from (5.2.2) by less than a factor of 2.

states. These have been studied in [208, 209] in the context of their production and detection at a lepton collider. It was found that the spectrum of [211, 133] does allow the KK quarks to be sufficiently stable for forming KK-quarkonia, but not for the annihilation decays to dominate over the single KK quark decays.[2] Including boundary terms can probably change these results in either direction, and we are particularly interested in the situation in which some of the KK quarks are more long-lived so that the branching ratio for annihilation is enhanced.

Other than that, it is useful to note that many of our results are largely determined by gauge interactions alone and depend only on the properties of the binding particles rather than the full spectrum of the model and are therefore valid much more generally than just for MSSM or UED. It is therefore useful to study all the possible bound states in these models, even if some of the binding particles are not sufficiently stable in generic MSSM or UED scenarios. With this motivation in mind, our study covers all the possible bound states of pair-produced colored particles in MSSM and UED.

5.2.2 Bound state formalism

Assuming that the masses of the pair of particles satisfy $m_1, m_2 \gg \Lambda_{\rm QCD}$, their dynamics can be described by the single-gluon exchange potential with the Coulomb-like form

$$V(r) = -C\frac{\overline{\alpha}_s}{r} \tag{5.2.4}$$

[2]It was claimed in [208] that KK top quarks can be very stable so that their annihilation decays dominate, but this was incorrect, as explained in [218].

Table 5.1: Pair production processes and the color representations of the pair. Two color-octets can form an octet with either a symmetric ($\propto d^{abc}$, denoted $\mathbf{8_S}$) or antisymmetric ($\propto f^{abc}$, $\mathbf{8_A}$) wave function. The Clebsch-Gordan coefficients for all the color decompositions can be found in [219]. We have not explicitly listed processes obtained by replacing particles by antiparticles.

UED	MSSM	binding	non-binding
$gg \to g^\star g^\star$	$gg \to \tilde{g}\tilde{g}$	$\mathbf{1}, \mathbf{8_S}, \mathbf{8_A}$	$\mathbf{10}, \overline{\mathbf{10}}, \mathbf{27}$
$q\overline{q} \to g^\star g^\star$	$q\overline{q} \to \tilde{g}\tilde{g}$	$\mathbf{1}, \mathbf{8_S}, \mathbf{8_A}$	
$gg \to q^\star \overline{q^\star}$	$gg \to \tilde{q}\tilde{q}^*$	$\mathbf{1}$	$\mathbf{8}$
$q\overline{q} \to q^\star \overline{q^\star}$	$q\overline{q} \to \tilde{q}\tilde{q}^*$	$\mathbf{1}$	$\mathbf{8}$
$qq \to q^\star q^\star$	$qq \to \tilde{q}\tilde{q}$	$\overline{\mathbf{3}}$	$\mathbf{6}$
$qg \to q^\star g^\star$	$qg \to \tilde{q}\tilde{g}$	$\mathbf{3}, \overline{\mathbf{6}}$	$\mathbf{15}$

Table 5.2: Bound states in UED and MSSM, their color representations and the strength of their potential (5.2.4). The possible spins of these bound states will be discussed later.

UED	MSSM	SU(3)	C
$(g^\star g^\star)$	$(\tilde{g}\tilde{g})$	$\mathbf{1}$	3
		$\mathbf{8}$	3/2
$(q^\star \overline{q^\star})$	$(\tilde{q}\tilde{q}^*)$	$\mathbf{1}$	4/3
$(q^\star q^\star), (\overline{q^\star}\,\overline{q^\star})$	$(\tilde{q}\tilde{q}), (\tilde{q}^*\tilde{q}^*)$	$\overline{\mathbf{3}}, \mathbf{3}$	2/3
$(q^\star g^\star), (\overline{q^\star} g^\star)$	$(\tilde{q}\tilde{g}), (\tilde{q}^*\tilde{g})$	$\mathbf{3}, \overline{\mathbf{3}}$	3/2
		$\overline{\mathbf{6}}, \mathbf{6}$	1/2

where $\overline{\alpha}_s$ denotes the strong coupling constant evaluated self-consistently at the scale of the inverse Bohr radius $a_0^{-1} = C\overline{\alpha}_s\mu$, where $\mu \equiv m_1 m_2/(m_1 + m_2)$ (while the plain α_s will be reserved for its value at the scale of m_1 and m_2) and

$$C = \frac{1}{2}\left(C_1 + C_2 - C_{(12)}\right) \tag{5.2.5}$$

where C_1 and C_2 are the quadratic Casimirs of the color representations of the two particles and $C_{(12)}$ of the bound state. For bound states considered in this chapter, the values of $\overline{\alpha}_s$

are between 0.11 and 0.15, so using (5.2.4) should be a good approximation, even though subleading corrections may have sizeable effects and it would be desirable to compute them, along with higher-order corrections to the production and annihilation processes, in a future work. Table 5.1 lists all the possible pair production processes in UED and MSSM and specifies in each case which of the color representations of the pair have an attractive potential and which do not, based on the sign of C. The values of C for all the attractive configurations are given in table 5.2. In cases where the bound states are colored, they will further hadronize with ordinary quarks or gluons to become color-neutral (if they are sufficiently long-lived for this to happen). However, these processes will be happening at much larger distance scales than both the production and annihilation of the bound states and we therefore ignore their effects.

One can get the matrix elements for bound state production and annihilation by representing the bound state as a superposition of states of two free particles with momenta distributed according to the bound state wavefunction $\psi(\mathbf{r})$. For an S-wave bound state, neglecting the dependence of the short-distance process on the momenta, it can be easily shown that the matrix element between the bound state and the particles from which the pair is produced is given by [220, 221]

$$\mathcal{M}_{\text{bound}} = \frac{\psi(\mathbf{0})}{\sqrt{2\mu}}\,\mathcal{M}_0 \tag{5.2.6}$$

where $\mathcal{M}_0$ is the matrix element describing the production of the free constituent particles at threshold and μ is their reduced mass. The cross section will then be proportional to

$$|\psi(\mathbf{0})|^2 = \frac{C^3\overline{\alpha}_s^3(2\mu)^3}{8\pi}. \tag{5.2.7}$$

More specifically, the bound state production cross section can be written in terms of the near-threshold production cross section of the pair of particles $\hat{\sigma}_0(\hat{s})$ as[3]

$$\hat{\sigma}_{\text{bound}}(\hat{s}) = \frac{8\pi}{2\mu} \frac{\hat{\sigma}_0(\hat{s})}{\beta(\hat{s})} |\psi(\mathbf{0})|^2 \, 2\pi \, \delta(\hat{s} - M^2) \tag{5.2.8}$$

where $M \simeq m_1 + m_2$ is the mass of the bound state and

$$\beta(\hat{s}) \equiv \sqrt{\frac{2\mu}{(M/2)^2} \left(\sqrt{\hat{s}} - m_1 - m_2\right)} \tag{5.2.9}$$

is the factor that makes the continuum production cross section $\hat{\sigma}_0(\hat{s})$ vanish at threshold. For $m_1 = m_2$, β is the velocity of each particle in the center-of-mass frame.

The annihilation rate of the bound state into two mass-m_0 particles is

$$\Gamma = \frac{|\psi(\mathbf{0})|^2}{64\pi \, m_1 m_2} \sqrt{1 - \frac{m_0^2}{(M/2)^2}} \int_0^\pi d\theta \, \sin\theta \sum |\mathcal{M}_0(\theta)|^2 \tag{5.2.10}$$

$$\left(\begin{array}{c} \times \dfrac{1}{2} \\ \end{array} \begin{array}{c} \text{for identical} \\ \text{bound particles} \end{array} \right) \left(\begin{array}{c} \times \dfrac{1}{2} \\ \end{array} \begin{array}{c} \text{for identical} \\ \text{final particles} \end{array} \right) \tag{5.2.11}$$

where $\mathcal{M}_0(\theta)$ is the matrix element between the pair of particles that form the bound state (with a particular spin and color representation) and the annihilation products, for any polarization and color state of the bound state, and the sum is over the colors and polarizations of the products.

[3]While (5.2.6)–(5.2.7) assume the binding particles to be distinct, the relation (5.2.8), with $|\psi(\mathbf{0})|^2$ given by (5.2.7), is valid also if they are identical. Later, in (5.2.11), $|\psi(\mathbf{0})|^2$ again refers to the expression (5.2.7) even in case of identical particles.

Table 5.3: KK gluonia ($g^\star g^\star$) (UED) and gluinonia ($\tilde{g}\tilde{g}$) (MSSM) and their possible couplings to gluons and quarks. Here $G^{\mu\nu}$ is the gluon field strength and $\tilde{G}^{\mu\nu} = \frac{1}{2}\epsilon^{\mu\nu\rho\sigma}G_{\rho\sigma}$; q denotes any quark flavor, while t refers to the top quark whose mass we do not neglect. In part of the spin-1 cases, the coupling is not to the bound state operator V_μ but to its derivative $\partial_\mu V_\nu$.

	color	J^{PC}	can couple to
$(g^\star g^\star)$	$\mathbf{1}, \mathbf{8_S}$	0^{++}	$G^{\rho\sigma}G_{\rho\sigma}$, $\bar{t}t$
	$\mathbf{8_A}$	1^{+-}	$\epsilon^{\mu\nu\rho\sigma} i\bar{t}\left[\gamma_\rho, \gamma_\sigma\right] t$
	$\mathbf{1}, \mathbf{8_S}$	2^{++}	$G^{\rho\mu}G_{\rho\nu}$, $G^{\rho\sigma}D_\mu D_\nu G_{\rho\sigma}$, $i\bar{q}\gamma^\mu D_\nu q$
$(\tilde{g}\tilde{g})$	$\mathbf{1}, \mathbf{8_S}$	0^{-+}	$G^{\rho\sigma}\tilde{G}_{\rho\sigma}$, $i\bar{t}\gamma^5 t$
	$\mathbf{8_A}$	1^{--}	$\bar{q}\gamma^\mu q$, $i\bar{t}\left[\gamma^\mu, \gamma^\nu\right] t$

5.3 KK gluonia vs. gluinonia

In this section we will study bound states of pairs of color octets: KK gluons $g^\star$ (spin 1) in UED and gluinos $\tilde{g}$ (spin 1/2) in MSSM. Later in this section we will also look at bound states of spin 0 color octets.

It is useful to classify the various possible bound states in the model according to their spin J, color representation, parity P, charge conjugation C, and the transformation under the chiral $U(1)$ symmetry of the quarks. This allows one to immediately determine the possible production and annihilation channels and describe the corresponding processes using effective interaction vertices involving the bound state and Standard Model fields. These effective vertices can then be used to simulate the bound state processes in an event generator. The coefficients of the vertices can be determined by matching to the relevant Feynman diagrams of the free pair of particles (times the wavefunction at the origin and the other factors).

In table 5.3 we list the allowed KK gluonia and gluinonia (taking the spin-statistics theorem into account) and the effective vertices through which each of them can couple to gluon or quark bilinears. The possible couplings to a pair of photons (for color-singlets) are

like the couplings to a pair of gluons.

To determine the charge conjugation properties of the color-octet bound states, it is useful to know that the action of charge conjugation C on a non-abelian gauge field V_μ^a is [222, 223, 224]

$$T^a V_\mu^a \to -\left(T^a\right)^{\mathrm{T}} V_\mu^a \tag{5.3.12}$$

where T^a are the generators of gauge transformations. The minus sign here can be described by saying that gluons have $C = -1$ (this is similar to the photon which transforms as $A_\mu \to -A_\mu$, thus having $C = -1$ in a more straightforward sense). Analogous transformation rules apply to KK gluons and gluinos. In the same sense, we find that $C = +1$ for $\mathbf{8_S}$ KK gluonia and gluinonia and $C = -1$ for $\mathbf{8_A}$ KK gluonia and gluinonia.[4]

From table 5.3 we see that the scalar KK gluonia and pseudoscalar gluinonia can be produced only by gluon fusion (but can annihilate also to $t\bar{t}$). The spin-1 KK gluonium cannot be produced at all from gluons or massless quarks while the vector gluinonium can be produced from quarks. The tensor KK gluonium couples to both gluons and quarks. We have checked that the explicit results that we will now present, based on diagrams in figures 5.1 and 5.2, indeed match these effective vertices. The tensor KK gluonium happens to couple to gluons only through $G^{\rho\mu}G_{\rho\nu}$ but not $G^{\rho\sigma}D_\mu D_\nu G_{\rho\sigma}$.

The parton-level bound state production cross sections can be written as

$$\hat{\sigma}_{\mathrm{bound},\,ij}(\hat{s}) = P_{ij}\,\zeta(3)\,\pi^2\overline{\alpha}_s^3\alpha_s^2\,\delta(\hat{s} - M^2) \tag{5.3.13}$$

[4]Our result for the charge conjugation of the $\mathbf{8_A}$ gluinonium ($(\tilde{g}\tilde{g})$, $\mathbf{8_A}$, $J^{PC} = 1^{--}$), or perhaps just the convention for defining the sign of C that would describe (5.3.12), differs from that of [225, 226, 227]. Note that our result (but not theirs) allows the coupling of this gluinonium to massless $q\bar{q}$ pairs (via the vector current $\overline{q}\gamma^\mu q$), which must be possible as we know explicitly from the diagrams.

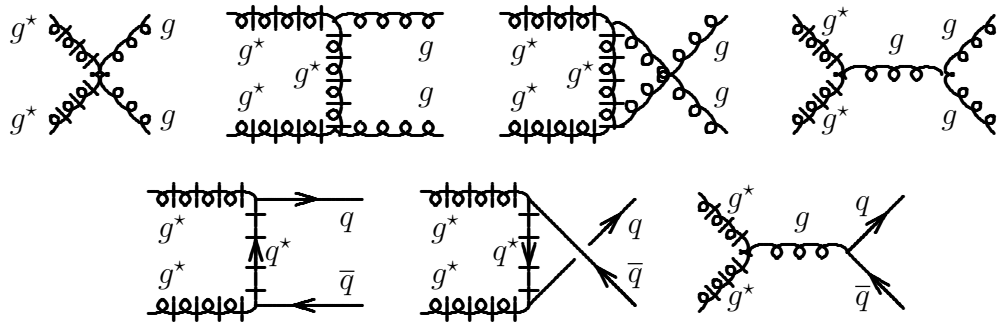

Figure 5.1: Diagrams for production or annihilation of a pair of KK gluons. For bound states, the diagrams with s channel gluon do not happen to contribute.

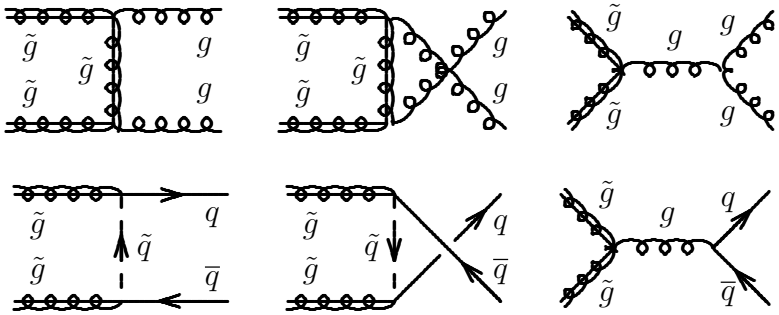

Figure 5.2: Diagrams for production or annihilation of a pair of gluinos.

where $\zeta(3) = \sum_{n=1}^{\infty} 1/n^3 \simeq 1.2$ takes into account the contributions of the radial excitations and the prefactors P_{ij} for producing the various bound states from partons i, j are presented in table 5.4 for KK gluonium and gluinonium. These results are based on the diagrams in figures 5.1 and 5.2 and factors such as (5.2.7). More details are given in appendix A. After convoluting (5.3.13) with the parton distribution functions as[5]

$$\sigma_{\text{bound}} = \frac{\zeta(3)\,\pi^2 \overline{\alpha}_s^3 \alpha_s^2}{s} \sum_{i,j} P_{ij} \int_{M^2/s}^1 \frac{dx}{x}\, f_{i/p}(x)\, f_{j/p}\left(\frac{M^2}{xs}\right) \tag{5.3.14}$$

[5]We are using NLO MSTW 2008 PDFs [228] evaluated at the scale $M/2$, and the center-of-mass energy $\sqrt{s} = 14$ TeV for the LHC.

Table 5.4: KK gluonium ($g^\star g^\star$) (UED), gluinonium ($\tilde{g}\tilde{g}$) (MSSM), and octetonium ($\phi\phi$) production cross section prefactors P_{ij} of (5.3.13). The different columns correspond to different values of the spin J of the bound state and its polarization (the projection J_z on the beam axis).

process	$J=0\,, J_z=0$	$J=1\,, \lvert J_z\rvert=1$	$J=2\,, \lvert J_z\rvert=2$	$J=2\,, \lvert J_z\rvert=1$
$gg \to (g^\star g^\star)_{\mathbf{1}}$	729/128		243/8	
$gg \to (g^\star g^\star)_{\mathbf{8_S}}$	729/512		243/32	
$gg \to (\tilde{g}\tilde{g})_{\mathbf{1}}$	243/64			
$gg \to (\tilde{g}\tilde{g})_{\mathbf{8_S}}$	243/256			
$gg \to (\phi\phi)_{\mathbf{1}}$	243/128			
$gg \to (\phi\phi)_{\mathbf{8_S}}$	243/512			
$q\bar{q} \to (g^\star g^\star)_{\mathbf{1}}$				$4\left(\frac{2m_{g^\star}^2}{m_{g^\star}^2+m_{q^\star}^2}\right)^2$
$q\bar{q} \to (g^\star g^\star)_{\mathbf{8_S}}$				$\frac{5}{4}\left(\frac{2m_{g^\star}^2}{m_{g^\star}^2+m_{q^\star}^2}\right)^2$
$q\bar{q} \to (\tilde{g}\tilde{g})_{\mathbf{8_A}}$		$\frac{9}{4}\left(\frac{m_{\tilde{q}^2}-m_{\tilde{g}}^2}{m_{\tilde{q}^2}+m_{\tilde{g}}^2}\right)^2$		

and multiplying by the appropriate branching ratios, we obtain the cross sections for dijet, $b\bar{b}$ and $t\bar{t}$ final states as shown in figure 5.3. We also show to what extent the results depend on the mass ratios $m_{q^\star}/m_{g^\star}$ or $m_{\tilde{q}/m_{\tilde{g}}}$ by varying them between 1 and ∞.[6] We see that the signals will typically be an order of magnitude larger for KK gluonia than for gluinonia of the same mass (except if the KK quarks are very heavy, in which case the $b\bar{b}$ and $t\bar{t}$ signals of KK gluonia disappear).

It is interesting to ask what creates this large difference in the cross sections. Unless the KK gluons (or gluinos) are heavier than about a TeV, production via the gg channel dominates due to its higher luminosity, so let us discuss it first and understand the order-of-

[6]In practice, the ratio must be somewhat larger than 1 in order for the annihilation rates to dominate, and the extreme limit of $m_{q^\star}/m_{g^\star} \to \infty$ is unphysical for UED (although it may be relevant for some other theory that does not contain KK quarks).

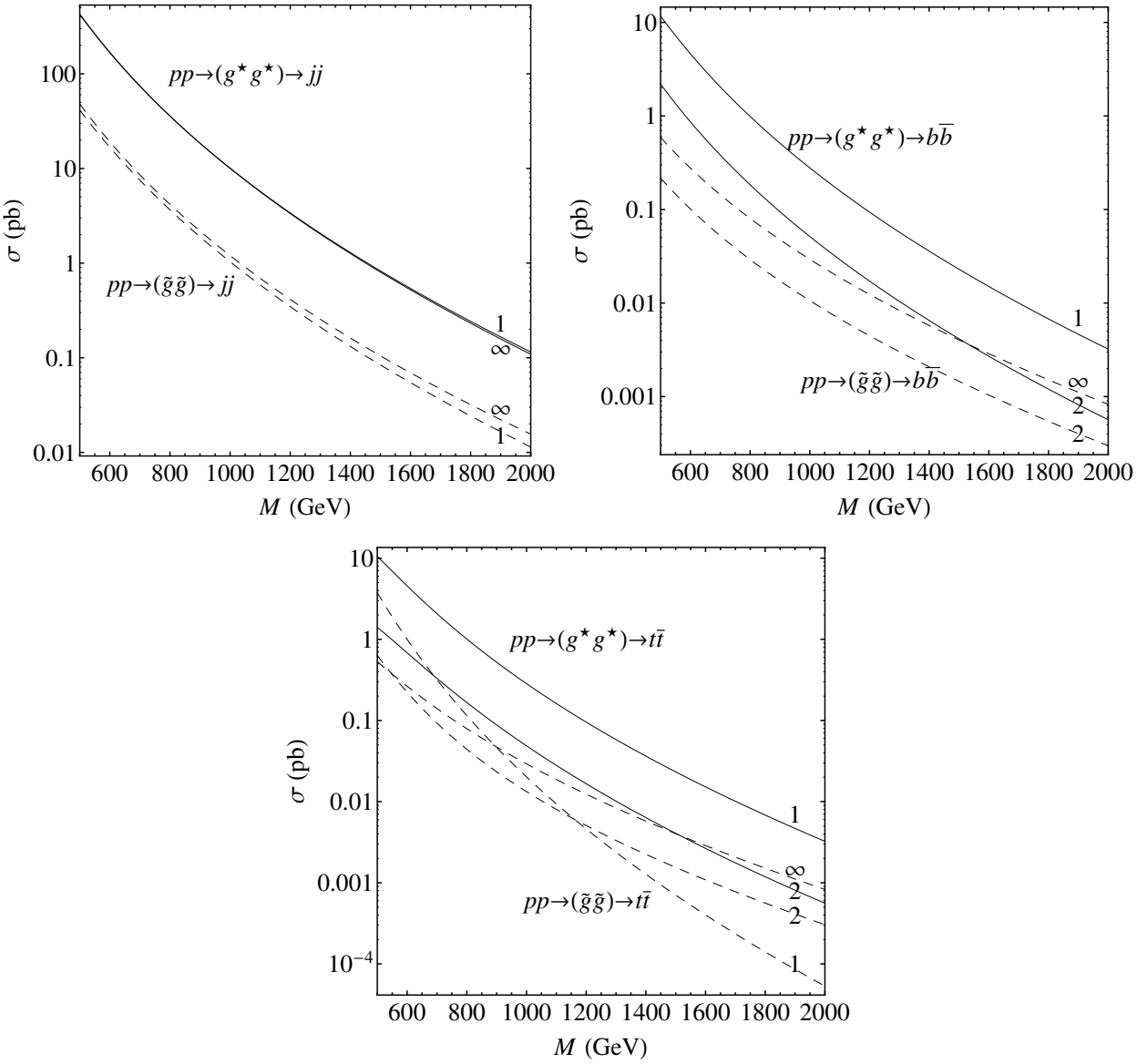

Figure 5.3: Dijet (top left), $b\bar{b}$ (top right) and $t\bar{t}$ (bottom) signals from KK gluonium annihilation (solid lines) vs. gluinonium annihilation (dashed lines) as a function of the resonance mass ($M = 2m_{g^\star}$ or $2m_{\tilde{g}}$) at the 14 TeV LHC. The different curves correspond to different ratios of $m_{q^\star}/m_{g^\star}$ or $m_{\tilde{q}/m_{\tilde{g}}}$ that are indicated next to them. The $b\bar{b}$ signal of $(\tilde{g}\tilde{g})$ vanishes for $m_{\tilde{q}=m_{\tilde{g}}}$, and the $b\bar{b}$ and $t\bar{t}$ signals of $(g^\star g^\star)$ vanish for $m_{q^\star}/m_{g^\star} \to \infty$.

magnitude difference seen already in the parton level expressions of table 5.4. The differences should be attributed to a large extent to the more numerous spin possibilities for the KK

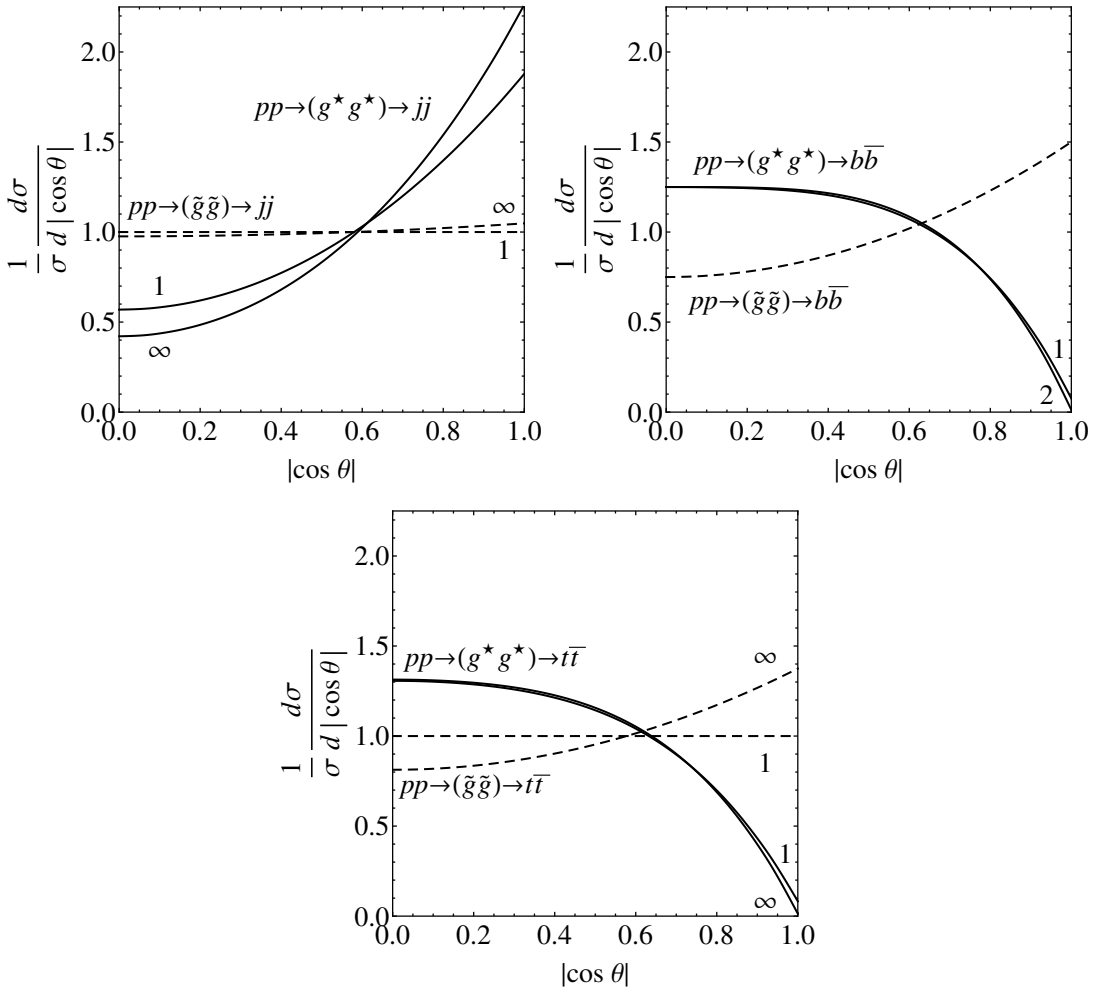

Figure 5.4: Angular distributions in annihilation of KK gluonia and gluinonia into di-jets (top left), $b\bar{b}$ (top right) and $t\bar{t}$ (bottom) at the LHC for $M = 800$ GeV (i.e., $m_{g^\star} = m_{\tilde{g}} = 400$ GeV). Here θ is the angle between the beam axis and the direction of motion of the annihilation products in the center-of-mass frame. The different curves correspond to different ratios of $m_{q^\star}/m_{g^\star}$ or $m_{\tilde{q}/m_{\tilde{g}}}$ that are indicated next to them (except for the $b\bar{b}$ signal of $(\tilde{g}\tilde{g})$ where there is no such dependence).

gluonia. According to table 5.4, in the gg channel (in both $\mathbf{1}$ and $\mathbf{8_S}$ representations), the parton-level production cross section for $J = 0$ KK gluonium is only a factor of 3/2 larger than that for $J = 0$ gluinonium. However, the KK gluonium can also be produced in $J = 2$ state, whose cross section (summed over the spin projections) is larger than that of the

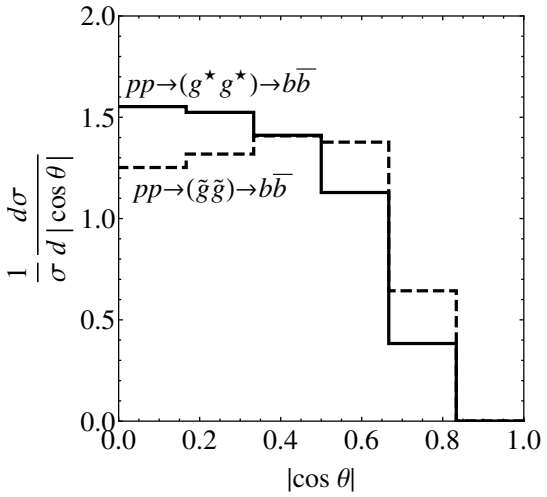

Figure 5.5: Simulated angular distributions in annihilation of KK gluonia and gluinonia into $b\bar{b}$ at the LHC.

($J = 0$) gluinonium by a factor of 8 (or larger than that of $J = 0$ KK gluonium by a factor of $16/3 \sim 5$). Overall, the gg channel produces 9.5 times more KK gluonium than gluinonium.[7] Note that these results are determined by gauge interactions alone, and therefore apply much more generally than to just UED and MSSM. In particular, the production diagrams do not involve any other new particles besides the KK gluons or gluinos.

In the $q\bar{q}$ channel, the comparison between KK gluonia and gluinonia is sensitive to the masses of the KK quarks (relative to the KK gluon) or squarks (relative to the gluino). If the KK quarks are very heavy the KK gluonium cross section goes to zero, while there is no such effect for the gluinonium. This is because the gluinonium can be produced via a diagram with an s channel gluon that does not involve squarks, while a similar diagram for

[7] In this case, this happens to be exactly the ratio of the near-threshold pair production cross sections (despite the fact that for the purposes of bound states we multiply this quantity by a different $|\psi(\mathbf{0})|^2$ for each of the attractive color representations and exclude the repulsive ones). In general, this does not need to be the case. For example, in the $q\bar{q}$ channel the ratio between bound state and near-threshold pair production cross section is 3 times bigger for the KK gluonia than for the gluinonia because the color representations in which KK gluon and gluino pairs are produced at threshold are different.

KK gluonium vanishes at threshold. On the other hand, the same s channel diagram of gluinonium interferes destructively with diagrams with t and u channel squarks, and this makes the gluinonium cross section vanish if the squarks are degenerate with the gluino, while there is no such effect for the KK gluonium. Note however that the presence of this effect for the gluinonium depends on the existence of squarks in MSSM, and thus will not be a general feature of new physics models with color-octet spin-1/2 particles. Similarly, the production of KK gluonia through the $q\overline{q}$ channel depends on the existence of KK quarks, and thus may not be present in some other model with color-octet spin-1 particles. Another difference between gluinonia and KK gluonia is that even though in both cases the bound states are produced with spin component ± 1 along the beam axis, it is an $\mathbf{8_A}$ ($J = 1$) state for gluinonium and $\mathbf{1}$ or $\mathbf{8_S}$ ($J = 2$) state for KK gluonium. The production of the $\mathbf{1}$ state (with its large color factor $(C_{\mathbf{1}}/C_{\mathbf{8}})^3 = 8$) in UED makes the cross section larger.

We also see from table 5.4 that KK gluonia will be produced predominantly in spin-2 states. If the angular distributions of the annihilation products can be measured, they can be used to distinguish the KK gluonium from the gluinonium (which is produced predominantly in spin-0 states, and also in the spin-1 state which is important for some of the annihilation channels). The angular distributions in the dijet, $b\overline{b}$ and $t\overline{t}$ channels are plotted in figure 5.4. The curves measured in experiment will be further affected by detector acceptances, effects of QCD radiation, mistakes in reconstruction, cuts, and uncertainties in modeling the QCD background which needs to be subtracted from the data. However, the remarkable differences between KK gluonium and gluinonium that we see in figure 5.4 will hopefully remain.

To simulate the effects of some of the experimental factors on the angular distributions, we generated events with PYTHIA, and the result (for example, for the $b\overline{b}$ channel) is shown

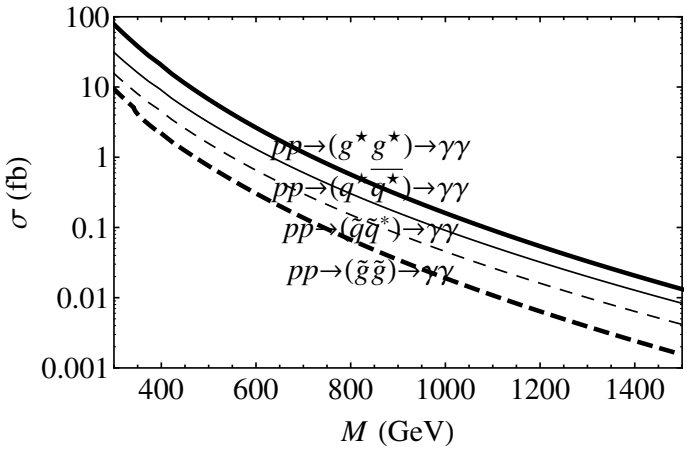

Figure 5.6: Diphoton annihilation signal of gluinonium (thick dashed line), KK gluonium (estimate; thick solid line), squarkonium (thin dashed line) and KK quarkonium (thin solid line) at the 14 TeV LHC as a function of the resonance mass. For gluinonium we assumed $m_{\tilde{q}=m_{\tilde{g}}}$ (and similarly for KK gluonium). For squarkonium and KK quarkonium we present the contribution of a single flavor and chirality, and we assumed the charges of the constituent particles to be $|Q| = 2/3$ (for $|Q| = 1/3$, the cross section is 16 times smaller).

in figure 5.5. The details of the simulation and the imposed cuts are the same as will be described in section 5.6 (except that the cut on $\cos\theta$ is not included and the p_T cut is relaxed to $p_T > 0.3M$).

Another channel we can look at is the annihilation of color-singlet KK gluonia or gluinonia into a pair of photons. Even though these processes can only proceed through loop diagrams because the KK gluons and gluinos are neutral, it is still interesting to consider this signal because the background in the diphoton channel is much more favorable than in the dijet, $b\bar{b}$ or $t\bar{t}$ channels. As long as the squarks are not much heavier than the gluino, the annihilation rate of the color-singlet gluinonium into $\gamma\gamma$ is $\sim 10^{-5}$ of its annihilation rate into gg (the exact expression from [227] is given in (A.2.38)). The relevant loop diagrams for KK gluonium have not been computed, but for our estimates we will assume that the diphoton branching ratio for spin-0 and spin-2 color-singlet KK gluonia is the same as for gluinonium. We expect

this to be correct up to an $O(1)$ factor since the relevant coupling constants and the gauge quantum numbers of the relevant particles are the same in both cases. The signal cross sections are shown in figure 5.6. The angular distributions in this channel may also be useful for discrimination since for gluinonia only the $J = 0$ state contributes, while for KK gluonia the contribution may be coming from both $J = 0$ and $J = 2$.

We can also compare the KK gluonia and gluinonia (which are bound states of spin-1 and spin-1/2 color octets) with bound states of scalar color-octets. Pairs of scalar color-octets ϕ will be produced by gluon fusion via the same diagrams as the KK gluons in figure 5.1, although in practice only the quartic vertex is relevant to bound states – "octetonia" ($\phi\phi$) in $\mathbf{1}$ and $\mathbf{8_S}$ color representations. Their production cross sections are included in table 5.4.[8] They are twice as small as the gluinonium cross sections. The octetonia decay rates are given in appendix A.3. Since the octetonia are scalars they will annihilate isotropically, and unless ϕ is charged under the electroweak group or interacts with some other particles, the only significant annihilation signal of octetonia will be gg dijets. It will be easy to distinguish them from bound states of spin-1 color-octets (like KK gluonia) because of the factor of ~ 20 difference in the cross section and the very different angular distributions. It will be more difficult to distinguish them from bound states of spin-1/2 color-octets (like gluinonia) because the angular distributions are also almost isotropic in the spin-1/2 case and the difference in the cross section is only a factor of 2. If the difference in the cross section is to be used, potential multiplicity of degenerate color-octets and higher order QCD corrections will be important. Part of the QCD corrections for gluinonium have been computed in [230, 227].

[8]The color-singlet result can be found in [229], and it agrees with ours.

Table 5.5: KK quarkonia ($q^\star\overline{q^\star}$) (UED) and squarkonia ($\tilde{q}\tilde{q}^*$) (MSSM) and their possible couplings to gluons, quarks and leptons. $P_{R,L} = (1 \pm \gamma^5)/2$. Antiparticle bound states, where relevant, are also present even if not listed in the table. In part of the spin-1 cases, the coupling is not to the bound state operator V_μ but to its derivative $\partial_\mu V_\nu$.

	color	J^{PC}	can couple to
$(q^\star_R\overline{q^\star_R}) + (q^\star_L\overline{q^\star_L})$	**1**	0^{-+}	$G^{\rho\sigma}\tilde{G}_{\rho\sigma}$, $i\bar{t}\gamma^5 t$
$(q^\star_R\overline{q^\star_R}) - (q^\star_L\overline{q^\star_L})$	**1**	0^{+-}	–
$(q^\star_L\overline{q^\star_R})$	**1**	0^{-+}	$i\bar{q}P_R q$, $i\bar{t}\gamma^5 t$
$(q^\star_R\overline{q^\star_R}) + (q^\star_L\overline{q^\star_L})$	**1**	1^{--}	$\bar{q}\gamma^\mu q$, $i\bar{t}\left[\gamma^\mu,\gamma^\nu\right]t$, $\bar{\ell}\gamma^\mu\ell$, $\bar{\ell}\gamma^\mu\gamma^5\ell$
$(q^\star_R\overline{q^\star_R}) - (q^\star_L\overline{q^\star_L})$	**1**	1^{++}	$\bar{q}\gamma^\mu\gamma^5 q$, $\bar{\ell}\gamma^\mu\ell$, $\bar{\ell}\gamma^\mu\gamma^5\ell$
$(q^\star_L\overline{q^\star_R})$	**1**	1^{--}	$i\bar{q}\left[\gamma^\mu,\gamma^\nu\right]P_R q$, $\bar{t}\gamma^\mu t$
$(\tilde{q}_R\tilde{q}^*_R) + (\tilde{q}_L\tilde{q}^*_L)$	**1**	0^{++}	$G^{\rho\sigma}G_{\rho\sigma}$, $\bar{t}t$
$(\tilde{q}_R\tilde{q}^*_R) - (\tilde{q}_L\tilde{q}^*_L)$	**1**	0^{--}	–
$(\tilde{q}_L\tilde{q}^*_R)$	**1**	0^{++}	$\bar{q}P_R q$, $\bar{t}t$

5.4 KK quarkonia vs. squarkonia

In this section we study bound states of fundamental-antifundamental pairs of KK quarks (spin 1/2) in UED and squarks (spin 0) in MSSM. Later in this section we will also look at bound states of spin 1 particles in the fundamental representation.

Table 5.5 classifies the KK quarkonia and squarkonia and their possible couplings to gluons and quarks (via the strong interactions) and leptons (via the electroweak interactions). The possible couplings to a pair of photons are like to a pair of gluons. The diagrams through which the various processes can be realized are shown in figures 5.7 and 5.8.

For both KK quarkonia and squarkonia, the dominant products of the gluon fusion channel are spin-0 bound states in which the KK quarks or squarks have same flavors and chiralities. These are also the only bound states that can annihilate into a pair of photons, which is the most promising detection channel as we discuss in the following. The angular

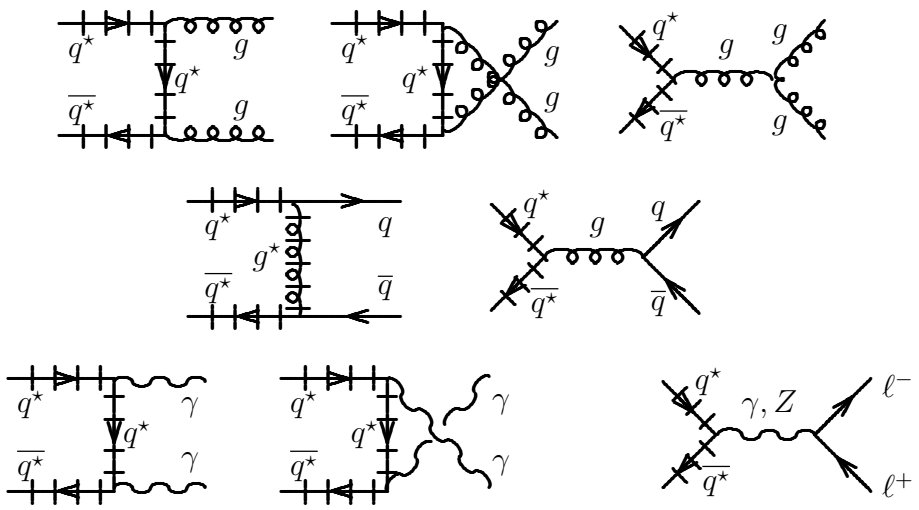

Figure 5.7: Diagrams for production or annihilation of a KK quark-KK antiquark pair. For bound states, the diagrams with s-channel gluon do not actually contribute.

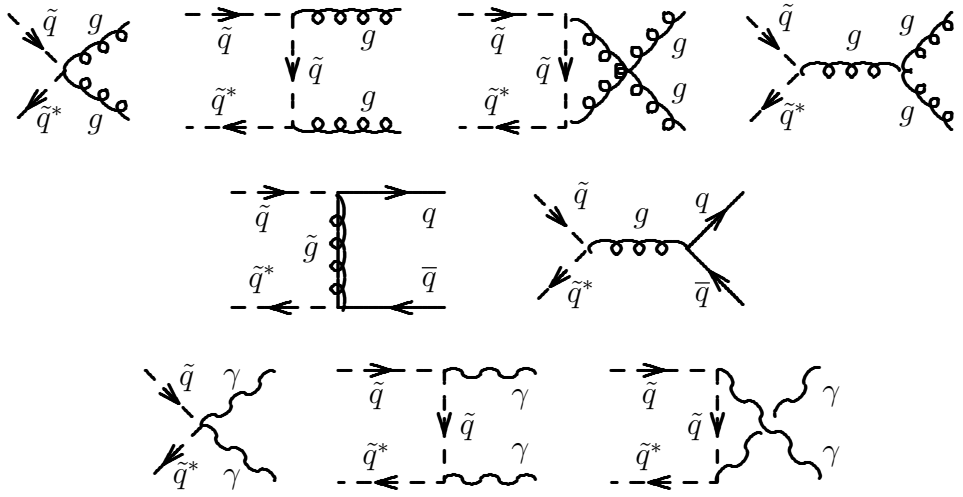

Figure 5.8: Diagrams for production or annihilation of a squark-antisquark pair. For bound states, only the first diagram in each row actually contributes.

distributions in the $\gamma\gamma$ channel will be isotropic in both UED and MSSM but the size of the cross section can still be used for discrimination.

In the $q\overline{q}$ fusion channel, the most interesting products are spin-1 bound states of KK quarks with same flavors and chiralities since they can annihilate into a pair of leptons,

Table 5.6: KK quarkonium ($q^\star\overline{q^\star}$) (UED) and squarkonium ($\tilde{q}\tilde{q}^*$) (MSSM) production cross section prefactors P_{ij} of (5.3.13). All the bound states are color-singlets. We use q and q' to refer to two different flavors of quarks (and similarly for KK quarks and squarks), while the notation $q^{(\prime)}$ means that the flavor can be either the same or different from that of q. All the numbers refer to a single choice of flavors and chiralities. For simplicity, we assumed the masses of the different flavors and chiralities of the KK quarks or squarks to be the same.

process	$J=0\,,J_z=0$	$J=1\,,\lvert J_z\rvert=1$	$J=1\,,J_z=0$
$gg\to(q_L^\star\overline{q_L^\star})$ or $(q_R^\star\overline{q_R^\star})$	$\dfrac{4}{81}$		
$gg\to(\tilde{q}_L\tilde{q}_L^*)$ or $(\tilde{q}_R\tilde{q}_R^*)$	$\dfrac{2}{81}$		
$q\overline{q}^{(\prime)}\to(q_L^\star\overline{q_L^\star}^{(\prime)})$ or $(q_R^\star\overline{q_R^\star}^{(\prime)})$ $q\overline{q}^{(\prime)}\to(q_L^\star\overline{q_R^\star}^{(\prime)})$ or $(q_R^\star\overline{q_L^\star}^{(\prime)})$	$\frac{64}{2187}\left(\frac{2m_{q^\star}^2}{m_{q^\star}^2+m_{g^\star}^2}\right)^2\left(4+\frac{m_{q^\star}^2}{m_{g^\star}^2}\right)^2$	$\frac{128}{2187}\left(\frac{2m_{q^\star}^2}{m_{q^\star}^2+m_{g^\star}^2}\right)^2\left(2+\frac{m_{q^\star}^2}{m_{g^\star}^2}\right)^2$	$\frac{64}{2187}\left(\frac{2m_{q^\star}^2}{m_{q^\star}^2+m_{g^\star}^2}\right)^2\left(\frac{m_{q^\star}^2}{m_{g^\star}^2}\right)^2$
$q\overline{q}^{(\prime)}\to(\tilde{q}_L\tilde{q}_R^{(\prime)*})$ or $(\tilde{q}_R\tilde{q}_L^{(\prime)*})$	$\dfrac{512}{2187}\left(\dfrac{2m_{\tilde{g}}m_{\tilde{q}}}{m_{\tilde{q}^2}+m_{\tilde{g}}^2}\right)^2$		

while there is no such process for squarkonia. A disadvantage of this production mechanism (which goes through the diagram with a t channel KK gluon from figure 5.7) is that it only has access to KK quarks of the flavors that are present in the colliding protons, so it will not be useful in the likely case that the lightest KK quark is a KK top. This leads us to consider also subleading production mechanisms which do not suffer from this problem. In particular, while spin-1 KK quarkonia cannot couple to a pair of gluons, they can be produced, similarly to J/ψ and Υ [231], in the process

$$gg \to g(q_\chi^\star \overline{q_\chi^\star})_{\mathbf{1},J=1}\,, \qquad \chi = L \text{ or } R \tag{5.4.15}$$

which is flavor-universal.

The gg and $\gamma\gamma$ KK quarkonium diagrams in figure 5.7 describe the same processes as one would have for heavy quarkonia (see [207] and references therein for the discussion of toponium and [232, 233] for quarkonia of new heavy quarks). The production mechanism (5.4.15) is also model-independent (it is determined by interactions with gluons). On the other hand, the $q\bar{q}$ channel is dominated by a diagram involving the KK gluon which does not exist for quarkonia. Another important difference is that the dominant annihilation process of spin-1 heavy quarkonia will be into pairs of longitudinal W bosons because of the quarks' large coupling to the Higgs which is responsible for their large masses [232].

The production cross sections for KK quarkonia and squarkonia are given by the expressions in appendices A.4 and A.5 and shown in table 5.6. Overall, the cross sections are about 2 orders of magnitude below those of gluinonia of the same mass. This is primarily due to the smaller color factors both in $|\psi(\mathbf{0})|^2 \propto C^3$ and in the short-distance matrix element. As a result, the dijet and $t\bar{t}$ annihilation channels, whose cross sections are included in figures 5.9

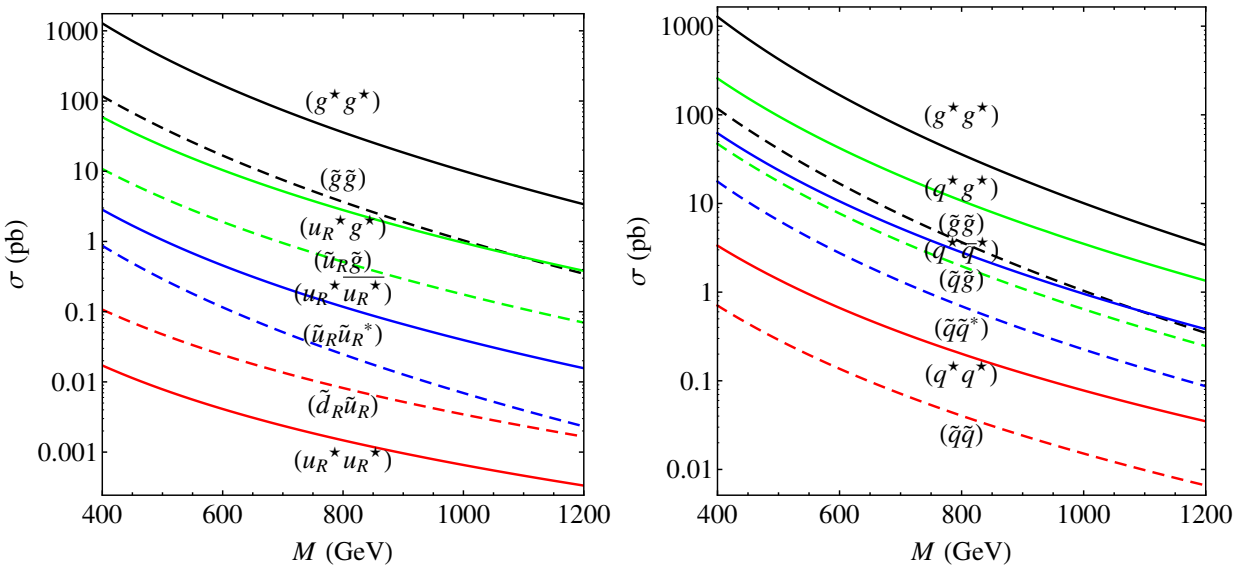

Figure 5.9: Dijet signal of the various bound states at the 14 TeV LHC as a function of the bound state mass ($M = 2m$), where all the particles are assumed to have the same mass m. The contributions of antiparticle bound states are included wherever relevant. On the left, we assume that the signal comes from particular flavors and chiralities of KK quarks or squarks and present several examples, while on the right we sum over all the possible combinations.

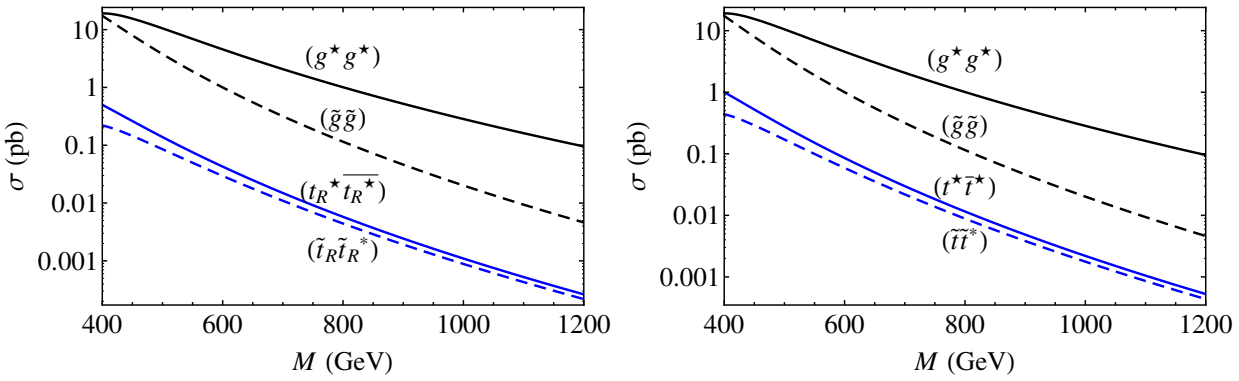

Figure 5.10: $t\bar{t}$ signal of the various bound states at the 14 TeV LHC as a function of the bound state mass ($M = 2m$), where all the particles are assumed to have the same mass m. For KK quarkonia and squarkonia, on the left we present examples of the contribution from KK tops and stops of a single chirality (the results for the other chirality are the same), while on the right we assume that both chiralities are close in mass and contribute.

and 5.10, are not promising.

However, the possibility of tree-level annihilation into $\gamma\gamma$ (which has low standard model background) is much more attractive despite the (α^2/α_s^2)-suppressed branching ratio of this mode. The cross section for the $\gamma\gamma$ signal is shown in figure 5.6 as a function of the bound state mass. The angular distributions in this channel are isotropic for both KK quarkonium and squarkonium but the signal will be twice larger in UED (when comparing equal KK quark and squark masses) due to the twice larger production cross section. This property can be used as a discriminator, although it may be important to take higher-order QCD corrections into account. Such corrections for the squarkonium (stoponium) have been studied in [234, 235]. Also, we have assumed the total annihilation rate of squarkonium to be dominated by gg, while in some cases annihilation into pairs of W, Z or Higgs bosons cannot be neglected [236, 237, 238, 217].

The cross sections for the dilepton annihilation channel of spin-1 KK quarkonia are shown in figure 5.11. The right plot refers to KK quarkonia produced through the subleading process (5.4.15) which has

$$\hat{\sigma}_{\text{bound}}\left(\hat{s}\right) = \frac{5\,\zeta(3)\,\pi}{243\,m_{q^\star}^2}\,\alpha_s^3\overline{\alpha}_s^3\,I\left(\frac{\hat{s}}{M^2}\right) \tag{5.4.16}$$

where as in [231]

$$I(\gamma) = \theta(\gamma-1)\left[\frac{2}{\gamma^2}\left(\frac{\gamma+1}{\gamma-1} - \frac{2\gamma\ln\gamma}{(\gamma-1)^2}\right) + \frac{2(\gamma-1)}{\gamma(\gamma+1)^2} + \frac{4\ln\gamma}{(\gamma+1)^3}\right] \tag{5.4.17}$$

On the other hand, squarkonia do not give rise to a dilepton signal.

While squarks and KK quarks are examples of spin-0 and spin-1/2 particles in the **3**

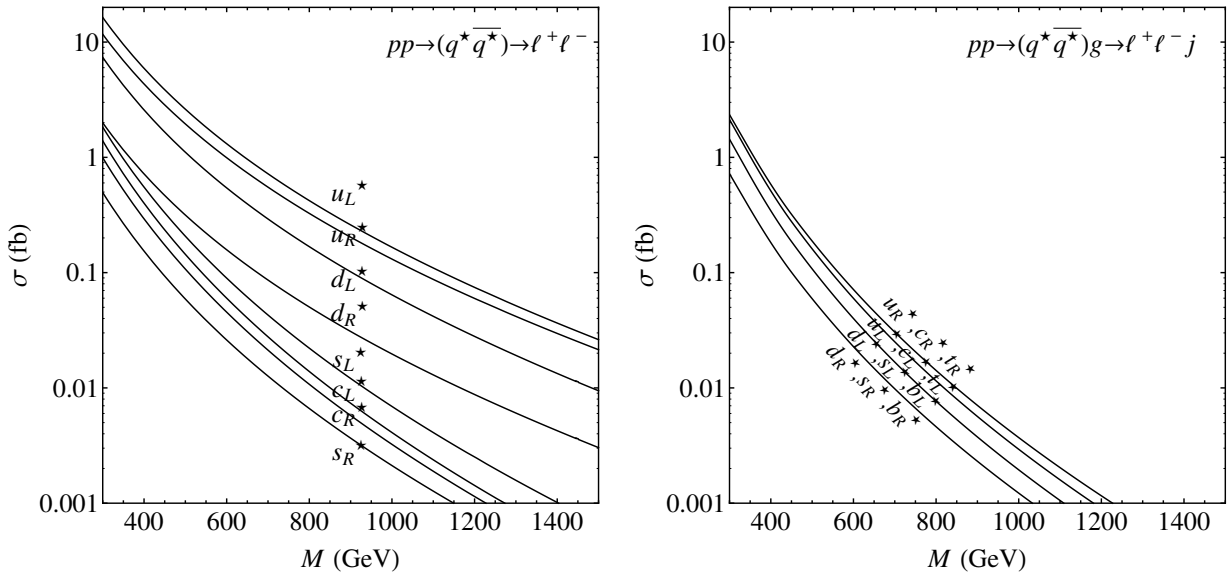

Figure 5.11: Dilepton annihilation signal of KK quarkonium at the 14 TeV LHC as a function of the resonance mass. The cross sections apply for any single flavor of leptons. Left: production via $q\overline{q} \to q^\star \overline{q^\star}$ (result independent of $m_{g^\star}$ unless $m_{g^\star} \gg m_{q^\star}$). Right: production via $gg \to q^\star \overline{q^\star} g$ for $m_{g^\star} = 2m_{q^\star}$ (for $m_{g^\star} = m_{q^\star}$ the branching ratios would be an order of magnitude smaller).

Table 5.7: Tripletonium production cross section prefactors P_{ij} of (5.3.13).

process	$J=0,\ J_z=0$	$J=2,\ \lvert J_z\rvert=2$
$gg \to (WW^*)$	2/27	32/81

representation, it may be interesting to consider also bound states of spin-1 particles in the same representation. Such vector color-triplets W^μ couple to gluons via

$$\mathcal{L} = -\frac{1}{2} W^*_{\mu\nu} W^{\mu\nu} - i g_s W^*_\mu T^a W_\nu G^{\mu\nu a} + m_W^2 W^*_\mu W^\mu \tag{5.4.18}$$

where $W_{\mu\nu} = D_\mu W_\nu - D_\nu W_\mu$ with $D_\mu = \partial_\mu - i g_s A^a_\mu T^a$ and $G^a_{\mu\nu}$ is the gluon field strength. The second term here is chosen such that tree-level unitarity in the production of vector pairs from gg is preserved at high energies, like in the situation when W^μ is a gauge boson

of an extended gauge group [239]. The W^μ particles may also couple to photons, which can be described by including the $-ieQA_\mu$ term in D_μ and adding an electromagnetic term analogous to the second term above. The diagrams coupling these vector particles to gluons or photons are the same as for squark-antisquark pairs, figure 5.8. The s-channel diagram does not actually contribute for the bound states. We do not consider production from $q\overline{q}$ since it would depend on the (model-dependent) couplings of the quarks to the vector bosons. We present the cross sections for the resulting bound states, "tripletonia", in table 5.7. The production cross section from gluons is an order of magnitude bigger than that of squarkonia and KK quarkonia. Furthermore, most of the tripletonia are produced with $J = 2$ rather than $J = 0$, which leads to different angular distributions of the annihilation products. More details are given in appendix A.6.

5.5 Di-KK quarks vs. di-squarks and KK quark-KK gluon vs. squark-gluino bound states

The possible diagrams for the remaining bound states are shown in figures 5.12, 5.13, 5.14 and 5.15. The resulting cross section prefactors are given in tables 5.8 and 5.9. For all of these bound states, the annihilation will be almost entirely into dijets, without any cleaner channels (even with a small branching ratio) to consider. Furthermore, the dijet signal (see figure 5.9) is typically even smaller than that of the gluinonium (whose signal we will analyze in more detail in the next section), and therefore cannot be seen on top of the QCD background in most scenarios. The only exception is if the mass spectrum of the model is very degenerate to the extent that signals from many different bound states merge into

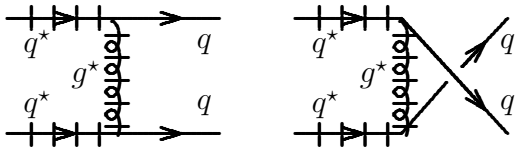

Figure 5.12: Diagrams for production or annihilation of a pair of KK quarks. The second diagram is relevant only if the flavors are equal.

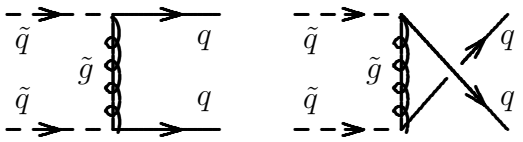

Figure 5.13: Diagrams for production or annihilation of a pair of squarks. The second diagram is relevant only if the flavors are equal.

Table 5.8: Di-KK quark ($q^\star q^\star$) (UED) and di-squark ($\tilde{q}\tilde{q}$) (MSSM) production cross section prefactors P_{ij} of (5.3.13). All the bound states are in the $\overline{\mathbf{3}}$ representation. All the numbers refer to a single flavor of that mass, and a single choice of the chiralities, and our notation assumes that $q' \neq q$. There also exist similar processes in which all the particles are replaced by their antiparticles. For simplicity, we assumed the masses of the different flavors and chiralities of the KK quarks or squarks to be the same.

process	$J=0,\ J_z=0$	$J=1,\ \lvert J_z\rvert=1$	$J=1,\ J_z=0$
$qq \to (q_L^\star q_L^\star)$ or $(q_R^\star q_R^\star)$	$\frac{2}{729}\left(\frac{2m_{q^\star}^2}{m_{q^\star}^2+m_{g^\star}^2}\right)^2\left(4+\frac{m_{q^\star}^2}{m_{g^\star}^2}\right)^2$		$\frac{4}{729}\left(\frac{2m_{q^\star}^2}{m_{q^\star}^2+m_{g^\star}^2}\right)^2\left(\frac{m_{q^\star}^2}{m_{g^\star}^2}\right)^2$
$qq' \to (q_L^\star q_L^{\star\prime})$ or $(q_R^\star q_R^{\star\prime})$			$\frac{2}{729}\left(\frac{2m_{q^\star}^2}{m_{q^\star}^2+m_{g^\star}^2}\right)^2\left(\frac{m_{q^\star}^2}{m_{g^\star}^2}\right)^2$
$qq \to (q_L^\star q_R^\star)$		$\frac{8}{729}\left(\frac{2m_{q^\star}^2}{m_{q^\star}^2+m_{g^\star}^2}\right)^2\left(2+\frac{m_{q^\star}^2}{m_{g^\star}^2}\right)^2$	
$qq' \to (q_L^\star q_R^{\star\prime})$ or $(q_R^\star q_L^{\star\prime})$		$\frac{4}{729}\left(\frac{2m_{q^\star}^2}{m_{q^\star}^2+m_{g^\star}^2}\right)^2\left(2+\frac{m_{q^\star}^2}{m_{g^\star}^2}\right)^2$	
$qq' \to (\tilde{q}_L\tilde{q}'_L)$ or $(\tilde{q}_R\tilde{q}'_R)$	$\frac{16}{729}\left(\frac{2m_{\tilde{g}}m_{\tilde{q}}}{m_{\tilde{g}}^2+m_{\tilde{q}^2}}\right)^2$		

one. This situation is exemplified in the right plot of figure 5.9 which sums over the flavors and chiralities of the KK quarks or squarks, which corresponds to the overly optimistic

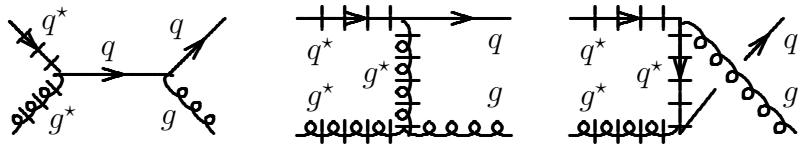

Figure 5.14: Diagrams for production or annihilation of a KK quark-KK gluon pair.

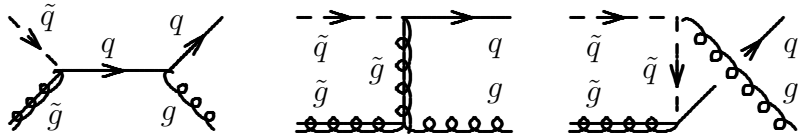

Figure 5.15: Diagrams for production or annihilation of a squark-gluino pair. For bound states, the last diagram does not actually contribute.

Table 5.9: KK quark-KK gluon ($q^\star g^\star$) (UED) and squark-gluino ($\tilde{q}\tilde{g}$) (MSSM) bound states production cross section prefactors P_{ij} of (5.3.13). All the numbers refer to a single flavor and chirality. There also exist similar processes in which all the particles are replaced by their antiparticles.

process	$J=\frac{3}{2},\ \lvert J_z\rvert=\frac{3}{2}$	$J=\frac{1}{2},\ \lvert J_z\rvert=\frac{1}{2}$
$qg\to(q^\star g^\star)_{\mathbf{3}}$	$\frac{3\,m_{q^\star}\left(m_{g^\star}+9m_{q^\star}\right)^2}{32\left(m_{g^\star}+m_{q^\star}\right)^3}$	$\frac{9\,m_{q^\star}^3\left(m_{g^\star}+9m_{q^\star}\right)^2}{64\left(m_{g^\star}+m_{q^\star}\right)^5}$
$qg\to(q^\star g^\star)_{\overline{\mathbf{6}}}$	$\frac{m_{q^\star}}{16\left(m_{g^\star}+m_{q^\star}\right)}$	$\frac{3\,m_{q^\star}^3}{32\left(m_{g^\star}+m_{q^\star}\right)^3}$
$qg\to(\tilde{q}\tilde{g})_{\mathbf{3}}$		$\frac{3\,m_{\tilde{g}}m_{\tilde{q}^2}\left(m_{\tilde{g}}+9m_{\tilde{q}}\right)^2}{32\left(m_{\tilde{g}}+m_{\tilde{q}}\right)^5}$
$qg\to(\tilde{q}\tilde{g})_{\overline{\mathbf{6}}}$		$\frac{m_{\tilde{g}}m_{\tilde{q}^2}}{16\left(m_{\tilde{g}}+m_{\tilde{q}}\right)^3}$

scenario in which all the flavors and chiralities are sufficiently long-lived and close in mass within $\sim 5\%$ so that the dijet signals of all their bound states merge into a single peak in the invariant mass distribution. Similarly, we may further sum the curves corresponding to different types of bound states. Even then, the dijet signal will be extremely challenging.

5.6 Detection prospects

We will now analyze to what extent the bound state signals discussed in the previous sections will be detectable at the LHC.[9] To that end, it is informative to consider the existing experimental constraints on the masses of the various UED and MSSM particles. Direct limits from the Tevatron Run I constrain the size of the extra dimension in UED as $1/R \gtrsim 300$ GeV [134, 245] (the KK modes masses are $m_1 \sim 1/R$). A much stronger limit can probably be obtained from the analysis of data available today. The most stringent indirect limit, $1/R \gtrsim 600$ GeV, arises from the inclusive radiative $\overline{B} \to X_s\gamma$ decay [246]. With the assumption that the Higgs is not much heavier than 115 GeV, the same limit is obtained from electroweak observables based on LEP data [247]. For the MSSM, the gluino mass is constrained by collider searches to $m_{\tilde{g}} \gtrsim 400$ GeV, and squarks are constrained to $m_{\tilde{q}\gtrsim 600}$ GeV, except for the sbottom (which can be lighter than 300 GeV) and the stop (which can even be under 200 GeV) [248, 249, 250, 251, 252, 253, 254]. It should be remembered though that MSSM and UED have multiple free parameters (the soft SUSY-breaking parameters in MSSM and the boundary terms in UED), and experimental bounds usually depend on certain arbitrary assumptions about them and thus apply in only part of the parameter space (for an example, see [255]). We therefore find it useful to consider also particles that are lighter than the bounds quoted above. Note also that many of our results do not depend on the full particle content of MSSM or UED and can be relevant to bound states in other models that are less constrained.

To simulate the bound state signals and the dominant standard model backgrounds we

[9] LHC signals of gluinonium have been also studied in [240, 241, 242, 243, 207] and squarkonium in [244, 238, 217, 235].

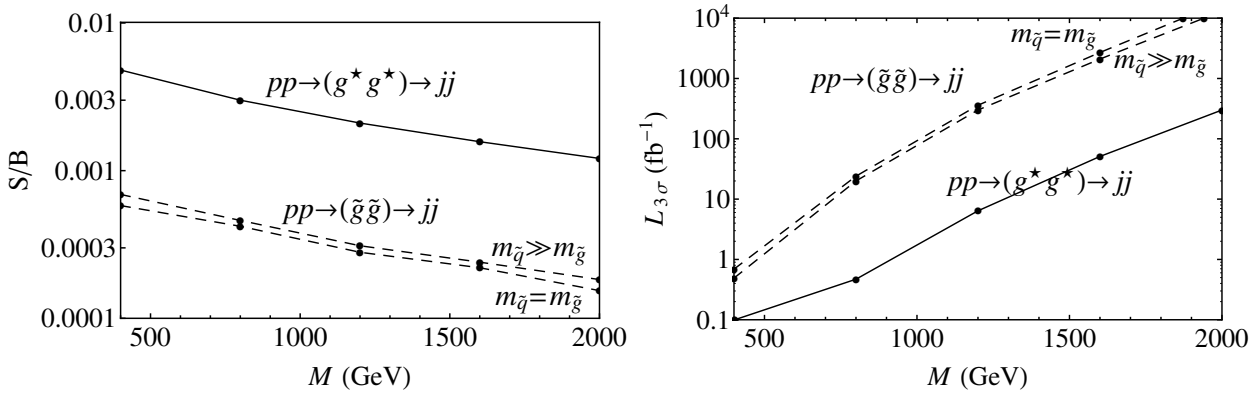

Figure 5.16: Dijet channel: signal-to-background ratio (left) and the luminosity required for 3σ significance (right) for gluinonium (dashed lines) and KK gluonium (solid line) at the 14 TeV LHC as a function of the resonance mass. For KK gluonium we assume $m_{q^\star} = m_{g^\star}$ while for gluinonium we present two cases.

used Pythia (version 8.120) [30, 256] with NLO MSTW 2008 PDFs [228] and SISCone jet algorithm (version 2.0.1) [257] with cone radius $R = 1$ (except for the $t\bar{t}$ analysis where we used $R = 0.5$), overlap parameter $f = 0.75$, no p_T threshold on stable cones, and an infinite number of passes. We selected several particles defined in Pythia and modified their coupling constants and branching ratios such that they would behave according to the bound state effective vertices from tables 5.3 and 5.5. For the purpose of simulation, we pretended all the bound states to be color singlets. We used the BSM Higgs for simulating spin-0 bound states, the Z' for spin-1 bound states (and Υ for simulating (5.4.15)), and the KK graviton for spin-2 bound states. We have simulated the backgrounds without any K-factors since our signals do not include higher-order QCD corrections either. Such corrections to the pair production processes, the bound state wavefunctions and the annihilation processes can be large and sometimes even change the cross section by a factor of ~ 2. Part of these corrections have already been computed for some of the MSSM bound states [230, 227, 234, 235] but none for UED. Our results will need to be re-examined once these corrections are known.

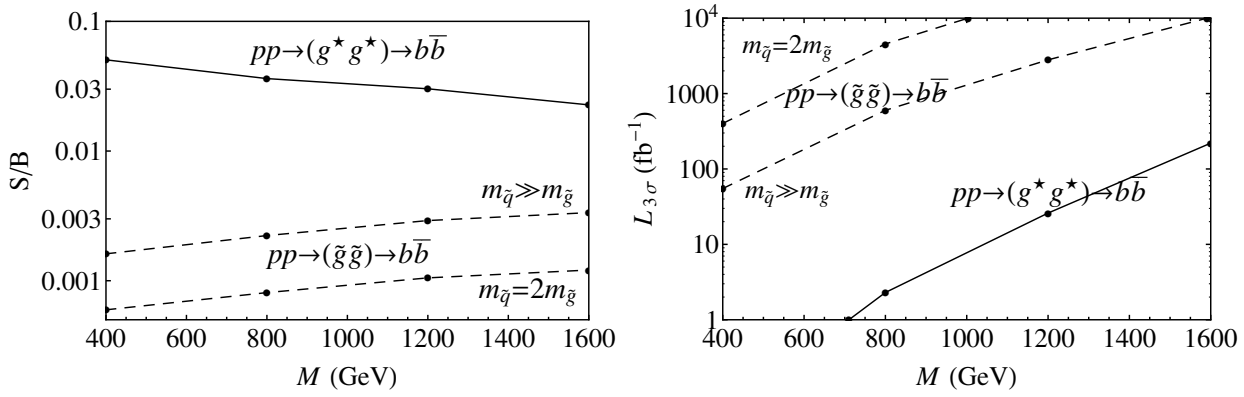

Figure 5.17: $b\bar{b}$ channel: signal-to-background ratio (left) and the luminosity required for 3σ significance (right) for gluinonium (dashed lines) and KK gluonium (solid line) at the 14 TeV LHC as a function of the resonance mass. For KK gluonium we assume $m_{q^\star} = m_{g^\star}$ while for gluinonium we present two cases.

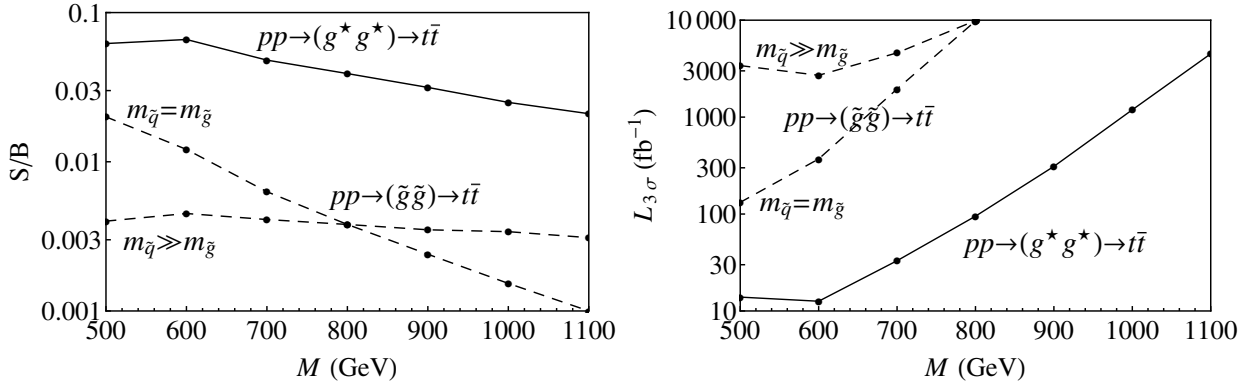

Figure 5.18: Semileptonic $t\bar{t}$ channel: signal-to-background ratio (left) and the luminosity required for 3σ significance (right) for gluinonium (dashed lines) and KK gluonium (solid line) at the 14 TeV LHC as a function of the resonance mass. For KK gluonium we assume $m_{q^\star} = m_{g^\star}$ while for gluinonium we present two cases.

In the analysis of the dijet channel, we require the two hardest jets within $|\eta| < 2.5$ to have $p_T > 2M/5$, the scattering angle in the partonic collision frame to satisfy $|\cos\theta| < 0.5$, and the dijet invariant mass to be within $\pm 15\%$ from the mass of the resonance. In the $b\bar{b}$ channel, we require two tagged jets and assume 60% tagging efficiency for b-jets, 1% mistag

rate for gluon and light quark jets and 15% mistag rate for c-jets. Based on [258, 259], we believe this level of b tagging performance will be realistic at least for resonances with $M \lesssim 1$ TeV. This leaves the standard model $b\bar{b}$ production as the dominant background. Besides the tagging efficiency factor, we use the same cuts as in the dijet channel. In the $t\bar{t}$ channel, we consider the standard model top production processes to be the background and use the procedure described in appendix C of [207] to reconstruct the 4-momenta of the two tops from their semileptonic decay products (which is the situation where one W from $t \to Wb$ decays leptonically and the other hadronically). We then count events in which the $t\bar{t}$ invariant mass is within $\pm 15\%$ from the mass of the resonance, the tops have $p_T > M/3$, and $|\cos\theta| < 0.5$.

The results for the dijet, $b\bar{b}$ and $t\bar{t}$ channels, respectively, are presented figures 5.16, 5.17 and 5.18. The dijet channel is unlikely to be realistic because of the very small signal-to-background ratio S/B (which implies high sensitivity to systematic errors in modeling the background). In the $b\bar{b}$ and $t\bar{t}$ channels the situation regarding S/B is more promising, especially for KK gluonium. As for the fluctuations in the background, the luminosity required for the statistical significance of the signal[10] is achievable for $m_{\tilde{g}} \lesssim 450$ GeV (if $m_{\tilde{q} \gg m_{\tilde{g}}}$) or $m_{g^\star} \lesssim 800$ GeV in the $b\bar{b}$ channel, and for $m_{\tilde{g}} \lesssim 300$ GeV (if $m_{\tilde{q} \sim m_{\tilde{g}}}$) or $m_{g^\star} \lesssim 500$ GeV in the $t\bar{t}$ channel.

In the diphoton channel we consider $q\bar{q} \to \gamma\gamma$ and $gg \to \gamma\gamma$ to be the dominant backgrounds.[11] We select events in which the two hardest photons within $|\eta| < 1.5$ have

[10] We compute the significance as $S/\sqrt{B}$, and present the value of integrated luminosity for which $S/\sqrt{B} = 3$.

[11] There will also be a contribution from γ+jet and dijet events in which jets are misidentified as photons. However, for the heavy resonances considered here, this background can be made subdominant by the tight photon identification criteria with only a mild reduction of the signal (see [260] for a recent study by CMS).

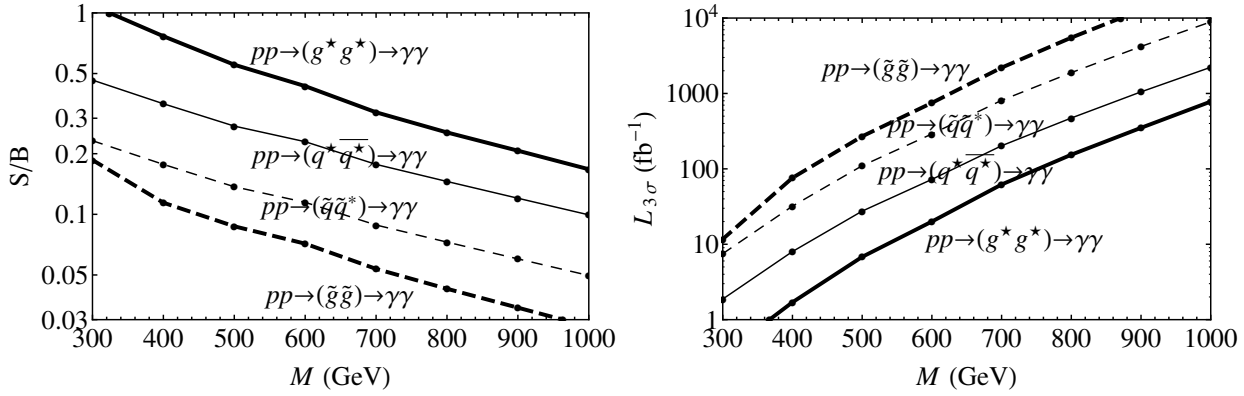

Figure 5.19: Diphoton channel: signal-to-background ratio (left) and the luminosity required for 3σ significance (right) for gluinonium (thick dashed line), KK gluonium (estimate; thick solid line), squarkonium (thin dashed line) and KK quarkonium (thin solid line) at the 14 TeV LHC as a function of the resonance mass. For gluinonium we assumed $m_{\tilde{q}=m_{\tilde{g}}}$ (and similarly for KK gluonium).

$p_T > 50$ GeV and look in the invariant mass window of $\pm 2\%$ around the mass of the resonance. The results are presented in figure 5.19. Since gluinonium is unlikely to be lighter than 600 GeV (corresponding to a 300 GeV gluino), the luminosity required to see its $\gamma\gamma$ signal is too high. On the other hand, for KK gluonium the signal is promising up to KK gluon masses of ~ 500 GeV. For squarkonium, the signal is viable for squark masses $\lesssim 350$ GeV. While typical squarks are expected to be at least as heavy as ~ 600 GeV, a stop can be much lighter. Luckily, the stop is also the squark that has the largest chance for being sufficiently long-lived so that stoponium will decay primarily by annihilation. Several models in which this happens were discussed in [217]. The stoponium $\gamma\gamma$ signal can thus be within the reach of the LHC. Similarly, a KK quark with mass $\lesssim 400$ GeV can have a viable $\gamma\gamma$ signal from KK quarkonium. Here we assumed that the KK quarks or squarks that form the bound state have charge $Q = 2/3$. For KK quarks or squarks with charge $Q = -1/3$ the cross sections will be 16 times smaller.

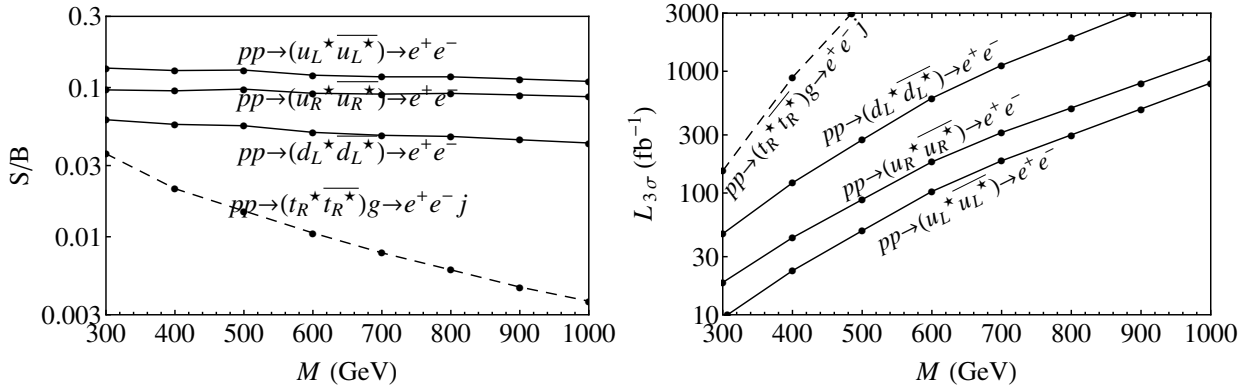

Figure 5.20: Dielectron channel: signal-to-background ratio (left) and the luminosity required for 3σ significance (right) for several examples of spin-1 KK quarkonia at the 14 TeV LHC as a function of the resonance mass. The solid curves correspond to the left plot of figure 5.11 and the dashed curves to the right plot.

In the dilepton channel, we focus on e^+e^- processes since they will have the best mass resolution. We include Drell-Yan processes as the background. We select events which include two electrons with $|\eta| < 2.5$ and $p_T > 60$ GeV and look in the invariant mass window of $\pm 2\%$ around the mass of the resonance. The resulting reach is shown in figure 5.20 for several cases of KK quarkonium. The signal is detectable for some KK quarkonia with KK quarks corresponding to the light quark flavors if $m_{q^\star} \lesssim 500$ GeV. On the other hand, for a perhaps more likely case that $t_R^\star$ is light, the e^+e^-+jet signal of $(t_R^\star\overline{t_R^\star})$ is much less promising, especially since for this case, as in the right plot of figure 5.11, we are already considering the more favorable situation of $m_{g^\star} = 2m_{q^\star}$ (rather than $m_{g^\star} \approx m_{q^\star}$).

5.7 Conclusions

In this chapter we have addressed all the possible S-wave QCD bound states of pairs of particles from the UED scenario and compared them with analogous bound states of

MSSM particles. KK gluonium and gluinonium were also compared with bound states of adjoint scalars, and KK quarkonium and squarkonium with bound states of color-triplet spin-1 particles.

We have found that if the KK gluon is sufficiently stable (which is likely to be the case if it is lighter than the KK quarks), its bound states signals at the LHC will have cross sections that are significantly larger than those of the gluinonium of the MSSM, mostly due to the larger number of spin states for KK gluonia. Besides the order-of-magnitude difference in the size of the cross sections, the angular distributions of the annihilation products can be used as a discriminator since KK gluonia will predominantly form with spin 2 (and some spin 0), while gluinonia will be mostly spin 0 (and some spin 1).

The diphoton signal of spin-0 KK quarkonium is twice as large as that of the squarkonium, and is potentially detectable if the constituent KK quarks are sufficiently stable and light. This difference in the cross section can help distinguish between KK quarks and squarks. Another potential discriminator is the dilepton annihilation signal of the vector KK quarkonium which might be measurable.

Despite the fact that bound state cross sections are very small, we found that in some cases the detection of the signal is realistic. For example, a 600 GeV KK gluon can give rise to a 1.2 TeV resonance in the $b\bar{b}$ channel, with $S/B \sim 3\%$ and 3σ significance reached at ~ 30 fb^{-1}. With even more luminosity, the angular distribution can hopefully be extracted and indicate the spin-2 nature of the bound state, confirming that the KK gluon has spin 1. Another example is a 400 GeV KK top whose bound state will appear as an 800 GeV resonance in the $\gamma\gamma$ channel with $S/B \sim 10\%$ and 3σ significance at ~ 600 fb^{-1}. Furthermore, many of our results remain valid for other models that contain pair-produced particles

with color representations and spins that our study has covered, but which can otherwise be slightly or completely different from the standard MSSM and UED scenarios and have weaker experimental bounds on the masses, which opens up additional possibilities.

Overall, our study has demonstrated how processes of bound state formation and annihilation, which are easy to compute for a given model and easy to reconstruct at the collider, provide additional channels for studying new particles at the LHC.

Appendix A

Cross sections, annihilation rates, angular distributions

In this appendix we give the expressions for the parton-level near-threshold pair-production cross section $\hat{\sigma}_0(\hat{s})$ which enters the calculation of the bound state production cross section (5.2.8). For UED processes, we used Feynman rules from [261, 134]. We separate the results by the color representation of the pair, its spin J, and the spin component J_z along the direction of motion of the first parton (where by, e.g., $|J_z| = 1$, we will refer to the sum of the contributions with $J_z = 1$ and $J_z = -1$ in cases when the two contributions are equal). We consider all the attractive color states and all the possible spins that can be produced from incoming quarks and/or gluons. We use q and q' to refer to two different flavors of quarks (and similarly for KK quarks and squarks), while the notation $q^{(\prime)}$ means that the flavor can be either the same or different from q. We use the subscript χ (as in $\tilde{q}_\chi$) to denote the chirality of the particle ($\chi = L$ or R) while $\not{\chi}$ refers to the other chirality. Our expressions for the cross sections refer to a single flavor and chirality choice for each of the two produced

particles (for squarks and KK quarks). Processes that are not listed have vanishing cross sections at threshold.

We also list the annihilation rates of the bound states into various final states and the corresponding angular distributions (where θ is the angle between the momenta of the annihilation products and the spin quantization axis, in the center-of-mass frame).

When a t quark appears as an annihilation product we take its mass m_t into account, but otherwise the masses of the quarks are set to zero. For simplicity, we assume that all the KK quarks have a common mass $m_{q^\star}$ and all the squarks have mass $m_{\tilde{q}}$.

A.1 KK gluonia

The cross sections for KK gluon pair production processes in the near-threshold limit, for the attractive color representations, are

$$\hat{\sigma}_0\left(gg \to g^\star g^\star\,;\,\mathbf{1},\,J=0\right) = \frac{27\pi\alpha_s^2\beta}{256m_{g^\star}^2} \tag{A.1.1}$$

$$\hat{\sigma}_0\left(gg \to g^\star g^\star\,;\,\mathbf{8_S},\,J=0\right) = \frac{27\pi\alpha_s^2\beta}{128m_{g^\star}^2} \tag{A.1.2}$$

$$\hat{\sigma}_0\left(gg \to g^\star g^\star\,;\,\mathbf{1},\,J=2,|J_z|=2\right) = \frac{9\pi\alpha_s^2\beta}{16m_{g^\star}^2} \tag{A.1.3}$$

$$\hat{\sigma}_0\left(gg \to g^\star g^\star\,;\,\mathbf{8_S},\,J=2,|J_z|=2\right) = \frac{9\pi\alpha_s^2\beta}{8m_{g^\star}^2} \tag{A.1.4}$$

$$\hat{\sigma}_0\left(q\overline{q} \to g^\star g^\star\,;\,\mathbf{1},\,J=2,|J_z|=1\right) = \left(\frac{2m_{g^\star}^2}{m_{g^\star}^2+m_{q^\star}^2}\right)^2 \frac{2\pi\alpha_s^2\beta}{27m_{g^\star}^2} \tag{A.1.5}$$

$$\hat{\sigma}_0\left(q\overline{q} \to g^\star g^\star\,;\,\mathbf{8_S},\,J=2,|J_z|=1\right) = \left(\frac{2m_{g^\star}^2}{m_{g^\star}^2+m_{q^\star}^2}\right)^2 \frac{5\pi\alpha_s^2\beta}{27m_{g^\star}^2} \tag{A.1.6}$$

The annihilation rates of the KK gluonia into the various final states are

$$\Gamma\left((g^\star g^\star)_{\mathbf{1},J=0} \to gg\right) = \frac{729}{8}\,\overline{\alpha}_s^3\alpha_s^2 m_{g^\star} \tag{A.1.7}$$

$$\Gamma\left((g^\star g^\star)_{\mathbf{8_S},J=0} \to gg\right) = \frac{729}{256}\,\overline{\alpha}_s^3\alpha_s^2 m_{g^\star} \tag{A.1.8}$$

$$\Gamma\left((g^\star g^\star)_{\mathbf{1},J=0} \to t\bar{t}\right) = \frac{3}{2}\frac{m_t^2}{m_{g^\star}^2}\left(1-\frac{m_t^2}{m_{g^\star}^2}\right)^{3/2}\left(\frac{2m_{g^\star}^2}{m_{g^\star}^2+m_{t^\star}^2-m_t^2}\right)^2\overline{\alpha}_s^3\alpha_s^2 m_{g^\star} \tag{A.1.9}$$

$$\Gamma\left((g^\star g^\star)_{\mathbf{8_S},J=0} \to t\bar{t}\right) = \frac{15}{256}\frac{m_t^2}{m_{g^\star}^2}\left(1-\frac{m_t^2}{m_{g^\star}^2}\right)^{3/2}\left(\frac{2m_{g^\star}^2}{m_{g^\star}^2+m_{t^\star}^2-m_t^2}\right)^2\overline{\alpha}_s^3\alpha_s^2 m_{g^\star} \tag{A.1.10}$$

$$\Gamma\left((g^\star g^\star)_{\mathbf{1},J=2} \to gg\right) = \frac{486}{5}\,\overline{\alpha}_s^3\alpha_s^2 m_{g^\star} \tag{A.1.11}$$

$$\Gamma\left((g^\star g^\star)_{\mathbf{8_S},J=2} \to gg\right) = \frac{243}{80}\,\overline{\alpha}_s^3\alpha_s^2 m_{g^\star} \tag{A.1.12}$$

$$\Gamma\left((g^\star g^\star)_{\mathbf{1},J=2} \to q\bar{q}\right) = \frac{18}{5}\left(\frac{2m_{g^\star}^2}{m_{g^\star}^2+m_{q^\star}^2}\right)^2\overline{\alpha}_s^3\alpha_s^2 m_{g^\star} \tag{A.1.13}$$

$$\Gamma\left((g^\star g^\star)_{\mathbf{8_S},J=2} \to q\bar{q}\right) = \frac{9}{64}\left(\frac{2m_{g^\star}^2}{m_{g^\star}^2+m_{q^\star}^2}\right)^2\overline{\alpha}_s^3\alpha_s^2 m_{g^\star} \tag{A.1.14}$$

$$\Gamma\left((g^\star g^\star)_{\mathbf{1},J=2} \to t\bar{t}\right) = \frac{18}{5}\left(1-\frac{m_t^2}{m_{g^\star}^2}\right)^{3/2}\left(1+\frac{2m_t^2}{3m_{g^\star}^2}\right)\left(\frac{2m_{g^\star}^2}{m_{g^\star}^2+m_{t^\star}^2-m_t^2}\right)^2\overline{\alpha}_s^3\alpha_s^2 m_{g^\star} \tag{A.1.15}$$

$$\Gamma\left((g^\star g^\star)_{\mathbf{8_S},J=2} \to t\bar{t}\right) = \frac{9}{64}\left(1-\frac{m_t^2}{m_{g^\star}^2}\right)^{3/2}\left(1+\frac{2m_t^2}{3m_{g^\star}^2}\right)\left(\frac{2m_{g^\star}^2}{m_{g^\star}^2+m_{t^\star}^2-m_t^2}\right)^2\overline{\alpha}_s^3\alpha_s^2 m_{g^\star} \tag{A.1.16}$$

The annihilation rates into $q\bar{q}$ should be further summed over the different quark flavors.

The angular distributions in annihilation of KK gluonia (in both $\mathbf{1}$ and $\mathbf{8_S}$ representations) into gg are given by

$$J=2, J_z=\pm 2: \qquad \frac{1}{\Gamma}\frac{d\Gamma}{\sin\theta\, d\theta} = \frac{5}{256}\left(35+28\cos 2\theta+\cos 4\theta\right) \tag{A.1.17}$$

$$J=2, J_z=\pm 1: \qquad \frac{1}{\Gamma}\frac{d\Gamma}{\sin\theta\, d\theta} = \frac{5}{16}\left(3+\cos 2\theta\right)\sin^2\theta \tag{A.1.18}$$

$$J=2, J_z=0: \qquad \frac{1}{\Gamma}\frac{d\Gamma}{\sin\theta\, d\theta} = \frac{15}{16}\sin^4\theta \tag{A.1.19}$$

In annihilation into $q\overline{q}$, for massless quarks we have

$$J=2, J_z=\pm 2: \qquad \frac{1}{\Gamma}\frac{d\Gamma}{\sin\theta\, d\theta} = \frac{5}{16}\left(3+\cos 2\theta\right)\sin^2\theta \tag{A.1.20}$$

$$J=2, J_z=\pm 1: \qquad \frac{1}{\Gamma}\frac{d\Gamma}{\sin\theta\, d\theta} = \frac{5}{16}\left(2+\cos 2\theta+\cos 4\theta\right) \tag{A.1.21}$$

$$J=2, J_z=0: \qquad \frac{1}{\Gamma}\frac{d\Gamma}{\sin\theta\, d\theta} = \frac{15}{16}\sin^2 2\theta \tag{A.1.22}$$

and for $t\bar{t}$

$$J=2, J_z=\pm 2: \quad \frac{1}{\Gamma}\frac{d\Gamma}{\sin\theta\, d\theta} = \frac{5}{16}\,\frac{1}{1+2m_t^2/3m_{g^\star}^2} \tag{A.1.23}$$

$$\times\left(3+\frac{m_t^2}{m_{g^\star}^2}+\left(1-\frac{m_t^2}{m_{g^\star}^2}\right)\cos 2\theta\right)\sin^2\theta \tag{A.1.24}$$

$$J=2, J_z=\pm 1: \quad \frac{1}{\Gamma}\frac{d\Gamma}{\sin\theta\, d\theta} = \frac{5}{16}\,\frac{1}{1+2m_t^2/3m_{g^\star}^2} \tag{A.1.25}$$

$$\times\left(2+\frac{m_t^2}{m_{g^\star}^2}+\cos 2\theta+\left(1-\frac{m_t^2}{m_{g^\star}^2}\right)\cos 4\theta\right) \tag{A.1.26}$$

$$J=2, J_z=0: \quad \frac{1}{\Gamma}\frac{d\Gamma}{\sin\theta\, d\theta} = \frac{15}{16}\,\frac{1}{1+2m_t^2/3m_{g^\star}^2} \tag{A.1.27}$$

$$\times\left(\sin^2 2\theta+\frac{11m_t^2}{18m_{g^\star}^2}+\frac{2m_t^2}{3m_{g^\star}^2}\cos 2\theta+\frac{m_t^2}{2m_{g^\star}^2}\cos 4\theta\right) \tag{A.1.28}$$

A.2 Gluinonia

The near-threshold production cross sections of attractive gluino pairs are

$$\hat{\sigma}_0\left(gg \to \tilde{g}\tilde{g}\,;\, \mathbf{1},\, J=0\right) = \frac{9\pi\alpha_s^2\beta}{128 m_{\tilde{g}}^2} \tag{A.2.29}$$

$$\hat{\sigma}_0\left(gg \to \tilde{g}\tilde{g}\,;\, \mathbf{8_S},\, J=0\right) = \frac{9\pi\alpha_s^2\beta}{64 m_{\tilde{g}}^2} \tag{A.2.30}$$

$$\hat{\sigma}_0\left(q\overline{q} \to \tilde{g}\tilde{g}\,;\, \mathbf{8_A},\, J=1,\, |J_z|=1\right) = \left(\frac{m_{\tilde{q}^2-m_{\tilde{g}}^2}}{m_{\tilde{q}^2+m_{\tilde{g}}^2}}\right)^2 \frac{\pi\alpha_s^2\beta}{3m_{\tilde{g}}^2} \tag{A.2.31}$$

The annihilation rates of the gluinonia are

$$\Gamma\left((\tilde{g}\tilde{g})_{\mathbf{1},J=0} \to gg\right) = \frac{243}{4}\overline{\alpha}_s^3\alpha_s^2 m_{\tilde{g}} \tag{A.2.32}$$

$$\Gamma\left((\tilde{g}\tilde{g})_{\mathbf{8_S},J=0} \to gg\right) = \frac{243}{128}\overline{\alpha}_s^3\alpha_s^2 m_{\tilde{g}} \tag{A.2.33}$$

$$\Gamma\left((\tilde{g}\tilde{g})_{\mathbf{1},J=0} \to t\bar{t}\right) = 9\,\frac{m_t^2}{m_{\tilde{g}}^2}\sqrt{1-\frac{m_t^2}{m_{\tilde{g}}^2}}\left(\frac{2m_{\tilde{g}}^2}{m_{\tilde{g}}^2+m_{\tilde{t}}^2-m_t^2}\right)^2 \overline{\alpha}_s^3\alpha_s^2 m_{\tilde{g}} \tag{A.2.34}$$

$$\Gamma\left((\tilde{g}\tilde{g})_{\mathbf{8_S},J=0} \to t\bar{t}\right) = \frac{45}{128}\,\frac{m_t^2}{m_{\tilde{g}}^2}\sqrt{1-\frac{m_t^2}{m_{\tilde{g}}^2}}\left(\frac{2m_{\tilde{g}}^2}{m_{\tilde{g}}^2+m_{\tilde{t}}^2-m_t^2}\right)^2 \overline{\alpha}_s^3\alpha_s^2 m_{\tilde{g}} \tag{A.2.35}$$

$$\Gamma\left((\tilde{g}\tilde{g})_{\mathbf{8_A},J=1} \to q\overline{q}\right) = \frac{27}{64}\left(\frac{m_{\tilde{q}^2-m_{\tilde{g}}^2}}{m_{\tilde{q}^2+m_{\tilde{g}}^2}}\right)^2 \overline{\alpha}_s^3\alpha_s^2 m_{\tilde{g}} \tag{A.2.36}$$

$$\Gamma\left((\tilde{g}\tilde{g})_{\mathbf{8_A},J=1} \to t\bar{t}\right) = \frac{27}{64}\left(1+\frac{m_t^2}{2m_{\tilde{g}}^2}\right)\sqrt{1-\frac{m_t^2}{m_{\tilde{g}}^2}}\left(\frac{m_{\tilde{t}}^2-m_{\tilde{g}}^2-m_t^2}{m_{\tilde{t}}^2+m_{\tilde{g}}^2-m_t^2}\right)^2 \overline{\alpha}_s^3\alpha_s^2 m_{\tilde{g}} \tag{A.2.37}$$

The branching ratio into $\gamma\gamma$ via loop diagrams is [227]

$$\frac{\Gamma\left((\tilde{g}\tilde{g})_{\mathbf{1},J=0} \to \gamma\gamma\right)}{\Gamma\left((\tilde{g}\tilde{g})_{\mathbf{1},J=0} \to gg\right)} = \frac{50\alpha^2}{81\pi^2}\left|\mathrm{Li}_2\left(-\frac{m_{\tilde{g}}^2}{m_{\tilde{q}^2}}\right) - \mathrm{Li}_2\left(\frac{m_{\tilde{g}}^2}{m_{\tilde{q}^2}}\right)\right|^2 = \frac{25\pi^2}{648}\alpha^2 \tag{A.2.38}$$

where in the last expression we substituted $m_{\tilde{q}=m_{\tilde{g}}}$.

The $J = 1$ $\mathbf{8_A}$ gluinonium has the following angular distributions in the annihilation into $q\overline{q}$ for massless quarks:

$$J = 1, J_z = \pm 1 : \qquad \frac{1}{\Gamma}\frac{d\Gamma}{\sin\theta\, d\theta} = \frac{3}{8}\left(1 + \cos^2\theta\right) \tag{A.2.39}$$

$$J = 1, J_z = 0 : \qquad \frac{1}{\Gamma}\frac{d\Gamma}{\sin\theta\, d\theta} = \frac{3}{4}\sin^2\theta \tag{A.2.40}$$

while for $t\bar{t}$:

$$J = 1, J_z = \pm 1 : \qquad \frac{1}{\Gamma}\frac{d\Gamma}{\sin\theta\, d\theta} = \frac{3}{8}\,\frac{1 + m_t^2/m_{\tilde{g}}^2}{1 + m_t^2/2m_{\tilde{g}}^2}\left(1 + \frac{1 - m_t^2/m_{\tilde{g}}^2}{1 + m_t^2/m_{\tilde{g}}^2}\,\cos^2\theta\right) \tag{A.2.41}$$

$$J = 1, J_z = 0 : \qquad \frac{1}{\Gamma}\frac{d\Gamma}{\sin\theta\, d\theta} = \frac{3}{4}\,\frac{1}{1 + m_t^2/2m_{\tilde{g}}^2}\left(\sin^2\theta + \frac{m_t^2}{m_{\tilde{g}}^2}\cos^2\theta\right) \tag{A.2.42}$$

A.3 Octetonia

The near-threshold production cross sections of attractive pairs of scalar color-octets are

$$\hat{\sigma}_0\left(gg \to \phi\phi\,;\, \mathbf{1}\right) = \frac{9\pi\alpha_s^2\beta}{256 m_\phi^2} \tag{A.3.43}$$

$$\hat{\sigma}_0\left(gg \to \phi\phi\,;\, \mathbf{8_S}\right) = \frac{9\pi\alpha_s^2\beta}{128 m_\phi^2} \tag{A.3.44}$$

The annihilation rates of the octetonia are

$$\Gamma\left((\phi\phi)_{\mathbf{1}} \to gg\right) = \frac{243}{8}\overline{\alpha}_s^3\alpha_s^2 m_\phi \tag{A.3.45}$$

$$\Gamma\left((\phi\phi)_{\mathbf{8_S}} \to gg\right) = \frac{243}{256}\overline{\alpha}_s^3\alpha_s^2 m_\phi \tag{A.3.46}$$

A.4 KK quarkonia

The near-threshold production cross sections of attractive KK quark-KK antiquark pairs are

$$\hat{\sigma}_0\left(gg \to q^\star_\chi \overline{q^\star_\chi};\, \mathbf{1},\, J=0\right) = \frac{\pi\alpha_s^2\beta}{96 m^2_{q^\star}} \tag{A.4.47}$$

$$\hat{\sigma}_0\left(q\overline{q}^{(\prime)} \to q^\star_\chi \overline{q^\star_\chi}^{(\prime)};\, \mathbf{1},\, J=0\right) = \left(\frac{2m^2_{q^\star}}{m^2_{q^\star}+m^2_{g^\star}}\right)^2 \left(4+\frac{m^2_{q^\star}}{m^2_{g^\star}}\right)^2 \frac{\pi\alpha_s^2\beta}{162 m^2_{q^\star}} \tag{A.4.48}$$

$$\hat{\sigma}_0\left(q\overline{q}^{(\prime)} \to q^\star_\chi \overline{q^\star_\chi}^{(\prime)};\, \mathbf{1},\, J=1, J_z=0\right) = \left(\frac{2m^2_{q^\star}}{m^2_{q^\star}+m^2_{g^\star}}\right)^2 \left(\frac{m^2_{q^\star}}{m^2_{g^\star}}\right)^2 \frac{\pi\alpha_s^2\beta}{162 m^2_{q^\star}} \tag{A.4.49}$$

$$\hat{\sigma}_0\left(q\overline{q}^{(\prime)} \to q^\star_L \overline{q^\star_L}^{(\prime)};\, \mathbf{1},\, J=1, J_z=-1\right) = \hat{\sigma}_0\left(q\overline{q}^{(\prime)} \to q^\star_R \overline{q^\star_R}^{(\prime)};\, \mathbf{1},\, J=1, J_z=1\right) \tag{A.4.50}$$

$$= \left(\frac{2m^2_{q^\star}}{m^2_{q^\star}+m^2_{g^\star}}\right)^2 \left(2+\frac{m^2_{q^\star}}{m^2_{g^\star}}\right)^2 \frac{\pi\alpha_s^2\beta}{81 m^2_{q^\star}} \tag{A.4.51}$$

The annihilation rates of the KK quarkonia are

$$\Gamma\left((q^\star_\chi \overline{q^\star_\chi})_{\mathbf{1},\, J=0} \to gg\right) = \frac{64}{81}\,\overline{\alpha}_s^3 \alpha_s^2 m_{q^\star} \tag{A.4.52}$$

$$\Gamma\left((t^\star_\chi \overline{t^\star_\chi})_{\mathbf{1},\, J=0} \to t\bar{t}\right) = \frac{16}{243}\frac{m_t^2}{m^2_{q^\star}}\sqrt{1-\frac{m_t^2}{m^2_{q^\star}}} \tag{A.4.53}$$

$$\times \left(\frac{2m^2_{q^\star}}{m^2_{g^\star}+m^2_{q^\star}-m_t^2}\right)^2 \left(2+\frac{m^2_{q^\star}}{m^2_{g^\star}}-\frac{m_t^2}{m^2_{g^\star}}\right)^2 \overline{\alpha}_s^3 \alpha_s^2 m_{q^\star} \tag{A.4.54}$$

$$\Gamma\left((q^\star_\chi \overline{q^\star_\chi}^{(\prime)})_{\mathbf{1},\, J=1} \to q\overline{q}^{(\prime)}\right) = \frac{64}{729}\left(\frac{2m^2_{q^\star}}{m^2_{g^\star}+m^2_{q^\star}}\right)^2 \left(2+\frac{m^2_{q^\star}}{m^2_{g^\star}}\right)^2 \overline{\alpha}_s^3 \alpha_s^2 m_{q^\star} \tag{A.4.55}$$

$$\Gamma\left((q^\star_\chi \overline{q^\star_\chi}^{(\prime)})_{\mathbf{1},\, J=0} \to q\overline{q}^{(\prime)}\right) = \frac{32}{243}\left(\frac{2m^2_{q^\star}}{m^2_{g^\star}+m^2_{q^\star}}\right)^2 \left(4+\frac{m^2_{q^\star}}{m^2_{g^\star}}\right)^2 \overline{\alpha}_s^3 \alpha_s^2 m_{q^\star} \tag{A.4.56}$$

$$\Gamma\left((q^\star_\chi \overline{q^\star_\chi}^{(\prime)})_{\mathbf{1},\, J=1} \to q\overline{q}^{(\prime)}\right) = \frac{32}{729}\left(\frac{2m^2_{q^\star}}{m^2_{g^\star}+m^2_{q^\star}}\right)^2 \left(\frac{m^2_{q^\star}}{m^2_{g^\star}}\right)^2 \overline{\alpha}_s^3 \alpha_s^2 m_{q^\star} \tag{A.4.57}$$

$$\Gamma\left((q_\chi^\star \overline{q_\chi^\star})_{\mathbf{1},\,J=0} \to \gamma\gamma\right) = \frac{32}{9}\,\overline{\alpha}_s^3\,Q^4\alpha^2 m_{q^\star} \tag{A.4.58}$$

The electroweak rates into fermions f (leptons or quarks) are

$$\Gamma\left((q_\chi^\star \overline{q_\chi^\star})_{\mathbf{1},\,J=1} \to f_\eta \overline{f}_\eta\right) = \frac{16}{27} n_c\,\overline{\alpha}_s^3 \left(\frac{\left(Q_\eta - T_\eta^3\right)\left(Q_\chi - T_\chi^3\right)}{\cos^2\theta_W} + \frac{T_\eta^3 T_\chi^3}{\sin^2\theta_W}\right)^2 \alpha^2 m_{q^\star} \tag{A.4.59}$$

where χ and η describe the chirality of the KK quark and the fermion, respectively, $n_c = 1$ for leptons and 3 for quarks, Q is the electric charge and T^3 is the weak isospin, and we assumed $m_Z^2 \ll (2m_{q^\star})^2$. More specifically, for annihilation into charged leptons

$$\Gamma\left((q_\chi^\star \overline{q_\chi^\star})_{\mathbf{1},\,J=1} \to \ell_\eta^+ \ell_\eta^-\right) = \frac{16}{27}\,\overline{\alpha}_s^3 c_{\chi\eta} \frac{\alpha^2}{\cos^4\theta_W} m_{q^\star} \tag{A.4.60}$$

with

$$c_{RR} = Q^2\,, \quad c_{RL} = \frac{Q^2}{4}\,, \quad c_{LR} = \left(Q - T^3\right)^2\,, \quad c_{LL} = \frac{1}{4}\left(Q - T^3 + T^3\cot^2\theta_W\right)^2 \tag{A.4.61}$$

where one should substitute $Q = 2/3$, $T^3 = 1/2$ for up-type KK quarks and $Q = -1/3$, $T^3 = -1/2$ for down-type KK quarks.

The angular distributions for $(q_L^\star \overline{q_L^\star}^{(\prime)})_{\mathbf{1},\,J=1} \to q\overline{q}^{(\prime)}$ are

$$J = 1, J_z = 1: \qquad \frac{1}{\Gamma}\frac{d\Gamma}{\sin\theta\, d\theta} = \frac{3}{2}\sin^4\frac{\theta}{2} \tag{A.4.62}$$

$$J = 1, J_z = -1: \qquad \frac{1}{\Gamma}\frac{d\Gamma}{\sin\theta\, d\theta} = \frac{3}{2}\cos^4\frac{\theta}{2} \tag{A.4.63}$$

$$J = 1, J_z = 0: \qquad \frac{1}{\Gamma}\frac{d\Gamma}{\sin\theta\, d\theta} = \frac{3}{4}\sin^2\theta \tag{A.4.64}$$

while for $(q_R^\star \overline{q_R^\star}^{(\prime)})_{\mathbf{1},\,J=1} \to q\overline{q}^{(\prime)}$ the same expressions hold for opposite signs of J_z. For both

$(q_L^\star \overline{q_R^\star}^{(\prime)})_{\mathbf{1},\,J=1} \to q\overline{q}^{(\prime)}$ and $(q_R^\star \overline{q_L^\star}^{(\prime)})_{\mathbf{1},\,J=1} \to q\overline{q}^{(\prime)}$,

$$J=1, J_z=\pm 1: \qquad \frac{1}{\Gamma}\frac{d\Gamma}{\sin\theta\, d\theta} = \frac{3}{4}\sin^2\theta \tag{A.4.65}$$

$$J=1, J_z=0: \qquad \frac{1}{\Gamma}\frac{d\Gamma}{\sin\theta\, d\theta} = \frac{3}{2}\cos^2\theta \tag{A.4.66}$$

For $(q_\chi^\star \overline{q_\chi^\star})_{\mathbf{1},\,J=1} \to \ell_R^+ \ell_R^-$:

$$J=1, J_z=1: \qquad \frac{1}{\Gamma}\frac{d\Gamma}{\sin\theta\, d\theta} = \frac{3}{2}\cos^4\frac{\theta}{2} \tag{A.4.67}$$

$$J=1, J_z=-1: \qquad \frac{1}{\Gamma}\frac{d\Gamma}{\sin\theta\, d\theta} = \frac{3}{2}\sin^4\frac{\theta}{2} \tag{A.4.68}$$

$$J=1, J_z=0: \qquad \frac{1}{\Gamma}\frac{d\Gamma}{\sin\theta\, d\theta} = \frac{3}{4}\sin^2\theta \tag{A.4.69}$$

while for $(q_\chi^\star \overline{q_\chi^\star})_{\mathbf{1},\,J=1} \to \ell_L^+ \ell_L^-$ the same expressions hold for opposite signs of J_z.

A.5 Squarkonia

The near-threshold production cross sections of attractive squark-antisquark pairs are

$$\hat{\sigma}_0\left(gg \to \tilde{q}_\chi \tilde{q}_\chi^*;\ \mathbf{1},\ J=0\right) = \frac{\pi\alpha_s^2\beta}{192 m_{\tilde{q}^2}} \tag{A.5.70}$$

$$\hat{\sigma}_0\left(q\overline{q}^{(\prime)} \to \tilde{q}_\chi \tilde{q}_\chi^{(\prime)*};\ \mathbf{1},\ J=0\right) = \left(\frac{2 m_{\tilde{g}} m_{\tilde{q}}}{m_{\tilde{q}^2+m_{\tilde{g}}^2}}\right)^2 \frac{4\pi\alpha_s^2\beta}{81 m_{\tilde{q}^2}} \tag{A.5.71}$$

The squarkonium annihilation rates are

$$\Gamma\left((\tilde{q}_\chi \tilde{q}_\chi^*)_{\mathbf{1},\,J=0} \to gg\right) = \frac{32}{81}\,\overline{\alpha}_s^3 \alpha_s^2 m_{\tilde{q}} \tag{A.5.72}$$

$$\Gamma\left((\tilde{t}_\chi \tilde{t}^*_\chi)_{\mathbf{1},\,J=0} \to t\bar{t}\right) = \frac{128}{243}\frac{m_t^2}{m_{\tilde{q}^2}\left(1-\frac{m_t^2}{m_{\tilde{q}^2}}\right)\sqrt{1-\frac{m_t^2}{m_{\tilde{q}^2}}\left(\frac{2m_{\tilde{q}^2}}{m_{\tilde{g}}^2+m_{\tilde{q}^2-m_t^2}}\right)^2}\,\overline{\alpha}_s^3\alpha_s^2 m_{\tilde{q}}} \tag{A.5.73}$$

$$\Gamma\left((\tilde{q}_\chi \tilde{q}^{(\prime)*}_\chi)_{\mathbf{1},\,J=0} \to q\bar{q}^{(\prime)}\right) = \frac{256}{243}\left(\frac{2m_{\tilde{g}}m_{\tilde{q}}}{m_{\tilde{g}}^2+m_{\tilde{q}^2}}\right)^2\overline{\alpha}_s^3\alpha_s^2 m_{\tilde{q}} \tag{A.5.74}$$

$$\Gamma\left((\tilde{q}_\chi \tilde{q}^*_\chi)_{\mathbf{1},\,J=0} \to \gamma\gamma\right) = \frac{16}{9}\,\overline{\alpha}_s^3\,Q^4\alpha^2 m_{\tilde{q}} \tag{A.5.75}$$

where Q is the electric charge of the squark.

A.6 Tripletonia

The near-threshold production cross sections of attractive pairs of vector color-triplets are

$$\hat{\sigma}_0\left(gg \to WW^*;\,\mathbf{1},\,J=2,|J_z|=2\right) = \frac{\pi\alpha_s^2\beta}{12m_W^2} \tag{A.6.76}$$

$$\hat{\sigma}_0\left(gg \to WW^*;\,\mathbf{1},\,J=0\right) = \frac{\pi\alpha_s^2\beta}{64m_W^2} \tag{A.6.77}$$

The annihilation rates of the tripletonia into gg are

$$\Gamma\left((WW^*)_{\mathbf{1},J=2} \to gg\right) = \frac{512}{405}\,\overline{\alpha}_s^3\alpha_s^2 m_W \tag{A.6.78}$$

$$\Gamma\left((WW^*)_{\mathbf{1},J=0} \to gg\right) = \frac{32}{27}\,\overline{\alpha}_s^3\alpha_s^2 m_W \tag{A.6.79}$$

If the vector bosons have electric charge Q they can annihilate into $\gamma\gamma$ with rates which can be obtained by the replacement

$$\alpha_s^2 \to \frac{9}{2}Q^4\alpha^2 \tag{A.6.80}$$

The angular distributions of the annihilation products (both gg and $\gamma\gamma$) are

$$J = 2, J_z = \pm 2 : \qquad \frac{1}{\Gamma}\frac{d\Gamma}{\sin\theta\, d\theta} = \frac{5}{256}\left(35 + 28\cos 2\theta + \cos 4\theta\right) \tag{A.6.81}$$

$$J = 2, J_z = \pm 1 : \qquad \frac{1}{\Gamma}\frac{d\Gamma}{\sin\theta\, d\theta} = \frac{5}{16}\left(3 + \cos 2\theta\right)\sin^2\theta \tag{A.6.82}$$

$$J = 2, J_z = 0 : \qquad \frac{1}{\Gamma}\frac{d\Gamma}{\sin\theta\, d\theta} = \frac{15}{16}\sin^4\theta \tag{A.6.83}$$

A.7 Di-KK quarks

The near-threshold production cross sections of attractive KK quark pairs are

$$\hat{\sigma}_0\left(qq \to q^\star_\chi q^\star_\chi\,;\, \overline{\mathbf{3}},\, J = 1, J_z = 0\right) = \left(\frac{2m^2_{q^\star}}{m^2_{q^\star} + m^2_{g^\star}}\right)^2 \left(\frac{m^2_{q^\star}}{m^2_{g^\star}}\right)^2 \frac{\pi\alpha_s^2\beta}{108 m^2_{q^\star}} \tag{A.7.84}$$

$$\hat{\sigma}_0\left(qq' \to q^\star_\chi q^{\star\prime}_\chi\,;\, \overline{\mathbf{3}},\, J = 1, J_z = 0\right) = \left(\frac{2m^2_{q^\star}}{m^2_{q^\star} + m^2_{g^\star}}\right)^2 \left(\frac{m^2_{q^\star}}{m^2_{g^\star}}\right)^2 \frac{\pi\alpha_s^2\beta}{216 m^2_{q^\star}} \tag{A.7.85}$$

$$\hat{\sigma}_0\left(qq' \to q^\star_\chi q^{\star\prime}_\chi\,;\, \overline{\mathbf{3}},\, J = 0\right) = \left(\frac{2m^2_{q^\star}}{m^2_{q^\star} + m^2_{g^\star}}\right)^2 \left(4 + \frac{m^2_{q^\star}}{m^2_{g^\star}}\right)^2 \frac{\pi\alpha_s^2\beta}{216 m^2_{q^\star}} \tag{A.7.86}$$

$$\hat{\sigma}_0\left(qq \to q^\star_L q^\star_R\,;\, \overline{\mathbf{3}},\, J = 1, |J_z| = 1\right) = \left(\frac{2m^2_{q^\star}}{m^2_{q^\star} + m^2_{g^\star}}\right)^2 \left(2 + \frac{m^2_{q^\star}}{m^2_{g^\star}}\right)^2 \frac{\pi\alpha_s^2\beta}{54 m^2_{q^\star}} \tag{A.7.87}$$

$$\hat{\sigma}_0\left(qq' \to q^\star_L q^{\star\prime}_R\,;\, \overline{\mathbf{3}},\, J = 1, J_z = -1\right) = \hat{\sigma}_0\left(qq' \to q^\star_R q^{\star\prime}_L\,;\, \overline{\mathbf{3}},\, J = 1, J_z = 1\right) \tag{A.7.88}$$

$$= \left(\frac{2m^2_{q^\star}}{m^2_{q^\star} + m^2_{g^\star}}\right)^2 \left(2 + \frac{m^2_{q^\star}}{m^2_{g^\star}}\right)^2 \frac{\pi\alpha_s^2\beta}{108 m^2_{q^\star}} \tag{A.7.89}$$

There are also processes in which the quarks and KK quarks are replaced by their antiparticles, which have the same cross sections for opposite signs of J_z.

The bound states annihilate into the same quark flavors from which they were produced.

The rates are

$$\Gamma\left((q^\star_\chi q^{\star\,(\prime)}_\chi)_{\overline{\mathbf{3}},\,J=1} \to q q^{(\prime)}\right) = \frac{1}{729}\left(\frac{2m^2_{q^\star}}{m^2_{q^\star}+m^2_{g^\star}}\right)^2\left(\frac{m^2_{q^\star}}{m^2_{g^\star}}\right)^2 \overline{\alpha}_s^3\alpha_s^2 m_{q^\star} \tag{A.7.90}$$

$$\Gamma\left((q^\star_\chi q^{\star\prime}_\chi)_{\overline{\mathbf{3}},\,J=0} \to q q^{\prime}\right) = \frac{1}{243}\left(\frac{2m^2_{q^\star}}{m^2_{q^\star}+m^2_{g^\star}}\right)^2\left(4+\frac{m^2_{q^\star}}{m^2_{g^\star}}\right)^2 \overline{\alpha}_s^3\alpha_s^2 m_{q^\star} \tag{A.7.91}$$

$$\Gamma\left((q^\star_\chi q^{\star\,(\prime)}_\chi)_{\overline{\mathbf{3}},\,J=1} \to q q^{(\prime)}\right) = \frac{2}{729}\left(\frac{2m^2_{q^\star}}{m^2_{q^\star}+m^2_{g^\star}}\right)^2\left(2+\frac{m^2_{q^\star}}{m^2_{g^\star}}\right)^2 \overline{\alpha}_s^3\alpha_s^2 m_{q^\star} \tag{A.7.92}$$

The angular distributions for $(q^\star_\chi q^{\star\,(\prime)}_\chi)_{\overline{\mathbf{3}},\,J=1} \to q q^{(\prime)}$ are

$$J=1, J_z=\pm 1: \qquad \frac{1}{\Gamma}\frac{d\Gamma}{\sin\theta\, d\theta} = \frac{3}{4}\sin^2\theta \tag{A.7.93}$$

$$J=1, J_z=0: \qquad \frac{1}{\Gamma}\frac{d\Gamma}{\sin\theta\, d\theta} = \frac{3}{2}\cos^2\theta \tag{A.7.94}$$

For $(q^\star_\chi q^\star_\chi)_{\overline{\mathbf{3}},\,J=1} \to qq$,

$$J=1, J_z=\pm 1: \qquad \frac{1}{\Gamma}\frac{d\Gamma}{\sin\theta\, d\theta} = \frac{3}{8}\left(1+\cos^2\theta\right) \tag{A.7.95}$$

$$J=1, J_z=0: \qquad \frac{1}{\Gamma}\frac{d\Gamma}{\sin\theta\, d\theta} = \frac{3}{4}\sin^2\theta \tag{A.7.96}$$

For $(q^\star_L q^{\star\prime}_R)_{\overline{\mathbf{3}},\,J=1} \to qq'$ (and for $(q^\star_R q^{\star\prime}_L)_{\overline{\mathbf{3}},\,J=1} \to qq'$ for opposite signs of J_z)

$$J=1, J_z=1: \qquad \frac{1}{\Gamma}\frac{d\Gamma}{\sin\theta\, d\theta} = \frac{3}{2}\sin^4\frac{\theta}{2} \tag{A.7.97}$$

$$J=1, J_z=-1: \qquad \frac{1}{\Gamma}\frac{d\Gamma}{\sin\theta\, d\theta} = \frac{3}{2}\cos^4\frac{\theta}{2} \tag{A.7.98}$$

$$J=1, J_z=0: \qquad \frac{1}{\Gamma}\frac{d\Gamma}{\sin\theta\, d\theta} = \frac{3}{4}\sin^2\theta \tag{A.7.99}$$

For the corresponding anti di-KK quarks, the angular distributions are the same for opposite

signs of J_z.

A.8 Di-squarks

The near-threshold production cross section for attractive squark pairs is

$$\hat{\sigma}_0\left(qq' \to \tilde{q}_\chi \tilde{q}'_\chi;\, \overline{\mathbf{3}},\, J=0\right) = \left(\frac{2m_{\tilde{g}} m_{\tilde{q}}}{m_{\tilde{g}}^2 + m_{\tilde{q}^2}}\right)^2 \frac{\pi \alpha_s^2 \beta}{27 m_{\tilde{q}^2}} \quad \text{(A.8.100)}$$

There are also processes in which the quarks and squarks are replaced by their antiparticles, which have the same cross section.

The annihilation rate of di-squarks is

$$\Gamma\left((\tilde{q}_\chi \tilde{q}'_\chi)_{\overline{\mathbf{3}},\, J=0} \to qq'\right) = \frac{8}{243}\left(\frac{2m_{\tilde{g}} m_{\tilde{q}}}{m_{\tilde{g}}^2 + m_{\tilde{q}^2}}\right)^2 \overline{\alpha}_s^3 \alpha_s^2 m_{\tilde{q}} \quad \text{(A.8.101)}$$

A.9 KK quark-KK gluon bound states

The near-threshold production cross sections for attractive KK quark-KK gluon pairs are

$$\hat{\sigma}_0\left(qg \to q^\star_R g^\star;\, \mathbf{3},\, J=\frac{3}{2}, J_z=\frac{3}{2}\right) = \frac{\left(m_{g^\star} + 9m_{q^\star}\right)^2}{288\, m_{g^\star}^2 m_{q^\star}\left(m_{g^\star} + m_{q^\star}\right)} \pi \alpha_s^2 \beta \quad \text{(A.9.102)}$$

$$\hat{\sigma}_0\left(qg \to q^\star_R g^\star;\, \mathbf{3},\, J=\frac{1}{2}, J_z=-\frac{1}{2}\right) = \frac{m_{q^\star}\left(m_{g^\star} + 9m_{q^\star}\right)^2}{192\, m_{g^\star}^2 \left(m_{g^\star} + m_{q^\star}\right)^3} \pi \alpha_s^2 \beta \quad \text{(A.9.103)}$$

$$\hat{\sigma}_0\left(qg \to q^\star_R g^\star;\, \overline{\mathbf{6}},\, J=\frac{3}{2}, J_z=\frac{3}{2}\right) = \frac{\left(m_{g^\star} + m_{q^\star}\right)}{16\, m_{g^\star}^2 m_{q^\star}} \pi \alpha_s^2 \beta \quad \text{(A.9.104)}$$

$$\hat{\sigma}_0\left(qg \to q^\star_R g^\star;\, \overline{\mathbf{6}},\, J=\frac{1}{2}, J_z=-\frac{1}{2}\right) = \frac{3\, m_{q^\star}}{32\, m_{g^\star}^2 \left(m_{g^\star} + m_{q^\star}\right)} \pi \alpha_s^2 \beta \quad \text{(A.9.105)}$$

Processes with $q_L^\star$ instead of $q_R^\star$ have the same cross sections for opposite signs of J_z. There are also processes in which the quark and KK quark are replaced by their antiparticles, which have the same cross sections for opposite signs of J_z.

The annihilation rates are

$$\Gamma\left((q^\star g^\star)_{\mathbf{3},\,J=3/2} \to qg\right) = \frac{3}{64}\,\overline{\alpha}_s^3\alpha_s^2\,\frac{m_{q^\star}\left(m_{g^\star}+9m_{q^\star}\right)^2}{\left(m_{g^\star}+m_{q^\star}\right)^2} \tag{A.9.106}$$

$$\Gamma\left((q^\star g^\star)_{\mathbf{3},\,J=1/2} \to qg\right) = \frac{9}{64}\,\overline{\alpha}_s^3\alpha_s^2\,\frac{m_{q^\star}^3\left(m_{g^\star}+9m_{q^\star}\right)^2}{\left(m_{g^\star}+m_{q^\star}\right)^4} \tag{A.9.107}$$

$$\Gamma\left((q^\star g^\star)_{\overline{\mathbf{6}},\,J=3/2} \to qg\right) = \frac{1}{64}\,\overline{\alpha}_s^3\alpha_s^2\,m_{q^\star} \tag{A.9.108}$$

$$\Gamma\left((q^\star g^\star)_{\overline{\mathbf{6}},\,J=1/2} \to qg\right) = \frac{3}{64}\,\overline{\alpha}_s^3\alpha_s^2\,\frac{m_{q^\star}^3}{\left(m_{g^\star}+m_{q^\star}\right)^2} \tag{A.9.109}$$

The angular distributions for $(q_R^\star g^\star) \to qg$ (in both $\mathbf{3}$ and $\overline{\mathbf{6}}$ representations) are

$$J=\frac{3}{2},\ J_z=+\frac{3}{2}: \qquad \frac{1}{\Gamma}\frac{d\Gamma}{\sin\theta\,d\theta} = 2\cos^6\frac{\theta}{2} \tag{A.9.110}$$

$$J=\frac{3}{2},\ J_z=+\frac{1}{2}: \qquad \frac{1}{\Gamma}\frac{d\Gamma}{\sin\theta\,d\theta} = 6\cos^4\frac{\theta}{2}\sin^2\frac{\theta}{2} \tag{A.9.111}$$

$$J=\frac{3}{2},\ J_z=-\frac{1}{2}: \qquad \frac{1}{\Gamma}\frac{d\Gamma}{\sin\theta\,d\theta} = 6\cos^2\frac{\theta}{2}\sin^4\frac{\theta}{2} \tag{A.9.112}$$

$$J=\frac{3}{2},\ J_z=-\frac{3}{2}: \qquad \frac{1}{\Gamma}\frac{d\Gamma}{\sin\theta\,d\theta} = 2\sin^6\frac{\theta}{2} \tag{A.9.113}$$

$$J=\frac{1}{2},\ J_z=+\frac{1}{2}: \qquad \frac{1}{\Gamma}\frac{d\Gamma}{\sin\theta\,d\theta} = \sin^2\frac{\theta}{2} \tag{A.9.114}$$

$$J=\frac{1}{2},\ J_z=-\frac{1}{2}: \qquad \frac{1}{\Gamma}\frac{d\Gamma}{\sin\theta\,d\theta} = \cos^2\frac{\theta}{2} \tag{A.9.115}$$

Processes with $q_L^\star$ instead of $q_R^\star$ have the same angular distributions for opposite signs of J_z. For the corresponding anti KK quark-KK gluon bound states, the angular distributions are

again the same for opposite signs of J_z.

A.10 Squark-gluino bound states

The near-threshold production cross sections for attractive squark-gluino pairs are

$$\hat{\sigma}_0\left(qg \to \tilde{q}_R\tilde{g}\,;\,\mathbf{3},\,J=\frac{1}{2},J_z=-\frac{1}{2}\right) = \frac{\left(m_{\tilde{g}}+9m_{\tilde{q})^2}\right.}{288\,m_{\tilde{g}}\left(m_{\tilde{g}}+m_{\tilde{q}}\right)^3}\,\pi\alpha_s^2\beta \qquad \text{(A.10.116)}$$

$$\hat{\sigma}_0\left(qg \to \tilde{q}_R\tilde{g}\,;\,\overline{\mathbf{6}},\,J=\frac{1}{2},J_z=-\frac{1}{2}\right) = \frac{1}{16\,m_{\tilde{g}}\left(m_{\tilde{g}}+m_{\tilde{q}}\right)}\,\pi\alpha_s^2\beta \qquad \text{(A.10.117)}$$

Processes with $\tilde{q}_L$ instead of $\tilde{q}_R$ have the same cross sections for opposite signs of J_z. There are also processes in which the quark and squark are replaced by their antiparticles, which have the same cross sections for opposite signs of J_z.

The annihilation rates are

$$\Gamma\left((\tilde{q}\tilde{g})_{\mathbf{3},\,J=1/2} \to qg\right) = \frac{3}{32}\,\overline{\alpha}_s^3\alpha_s^2\,\frac{m_{\tilde{g}}m_{\tilde{q}^2\left(m_{\tilde{g}}+9m_{\tilde{q}}\right)^2}}{\left(m_{\tilde{g}}+m_{\tilde{q}}\right)^4} \qquad \text{(A.10.118)}$$

$$\Gamma\left((\tilde{q}\tilde{g})_{\overline{\mathbf{6}},\,J=1/2} \to qg\right) = \frac{1}{32}\,\overline{\alpha}_s^3\alpha_s^2\,\frac{m_{\tilde{g}}m_{\tilde{q}^2}}{\left(m_{\tilde{g}}+m_{\tilde{q}}\right)^2} \qquad \text{(A.10.119)}$$

The angular distributions for $(\tilde{q}_R\tilde{g}) \to qg$ (in both $\mathbf{3}$ and $\overline{\mathbf{6}}$ representations) are

$$J_z=\frac{1}{2}: \qquad \frac{1}{\Gamma}\frac{d\Gamma}{\sin\theta\,d\theta} = \sin^2\frac{\theta}{2} \qquad \text{(A.10.120)}$$

$$J_z=-\frac{1}{2}: \qquad \frac{1}{\Gamma}\frac{d\Gamma}{\sin\theta\,d\theta} = \cos^2\frac{\theta}{2} \qquad \text{(A.10.121)}$$

The angular distributions for $(\tilde{q}_L\tilde{g}) \to qg$ are the same for opposite signs of J_z. For the corresponding anti squark-gluino bound states, the angular distributions are the same, again

for opposite signs of J_z.

Bibliography

[1] P. Langacker, "Structure of the standard model," arXiv:hep-ph/0304186 [hep-ph].

[2] **ATLAS Collaboration** Collaboration, "Observation of an Excess of Events in the Search for the Standard Model Higgs boson with the ATLAS detector at the LHC,".

[3] **CMS Collaboration** Collaboration, S. Chatrchyan *et al.*, "Observation of a new boson at a mass of 125 GeV with the CMS experiment at the LHC," *Phys.Lett.* **B716** (2012) 30–61, arXiv:1207.7235 [hep-ex].

[4] H. Murayama, "Physics Beyond the Standard Model and Dark Matter," arXiv:0704.2276 [hep-ph].

[5] S. P. Martin, "A Supersymmetry primer," arXiv:hep-ph/9709356 [hep-ph].

[6] T. G. Rizzo, "Introduction to Extra Dimensions," *AIP Conf.Proc.* **1256** (2010) 27–50, arXiv:1003.1698 [hep-ph].

[7] S. D. Ellis, A. Hornig, T. S. Roy, D. Krohn, and M. D. Schwartz, "Qjets: A Non-Deterministic Approach to Tree-Based Jet Substructure," *Phys.Rev.Lett.* **108** (2012) 182003, arXiv:1201.1914 [hep-ph].

[8] D. Kahawala, D. Krohn, and M. J. Strassler, "Measuring the Bottom-Quark Forward-Central Asymmetry at the LHC," *JHEP* **1201** (2012) 069, arXiv:1108.3301 [hep-ph].

[9] M. R. Buckley, B. Echenard, D. Kahawala, and L. Randall, "Stable Colored Particles R-SUSY Relics or Not?," *JHEP* **1101** (2011) 013, arXiv:1008.2756 [hep-ph].

[10] D. Kahawala and Y. Kats, "Distinguishing spins at the LHC using bound state signals," *JHEP* **1109** (2011) 099, arXiv:1103.3503 [hep-ph].

[11] G. P. Salam, "Towards Jetography," *Eur.Phys.J.* **C67** (2010) 637–686, arXiv:0906.1833 [hep-ph].

[12] A. Altheimer, S. Arora, L. Asquith, G. Brooijmans, J. Butterworth, *et al.*, "Jet Substructure at the Tevatron and LHC: New results, new tools, new benchmarks," *J.Phys.* **G39** (2012) 063001, arXiv:1201.0008 [hep-ph].

[13] J. Shelton, "TASI Lectures on Jet Substructure," arXiv:1302.0260 [hep-ph].

[14] T. Plehn and M. Spannowsky, "Top Tagging," *J.Phys.* **G39** (2012) 083001, arXiv:1112.4441 [hep-ph].

[15] M. Cacciari, G. P. Salam, and G. Soyez, "The Anti-k(t) jet clustering algorithm," *JHEP* **0804** (2008) 063, arXiv:0802.1189 [hep-ph].

[16] Y. L. Dokshitzer, G. Leder, S. Moretti, and B. Webber, "Better jet clustering algorithms," *JHEP* **9708** (1997) 001, arXiv:hep-ph/9707323 [hep-ph].

[17] M. Wobisch and T. Wengler, "Hadronization corrections to jet cross-sections in deep inelastic scattering," arXiv:hep-ph/9907280 [hep-ph].

[18] S. Catani, Y. L. Dokshitzer, M. Seymour, and B. Webber, "Longitudinally invariant K_t clustering algorithms for hadron hadron collisions," *Nucl.Phys.* **B406** (1993) 187–224.

[19] S. D. Ellis and D. E. Soper, "Successive combination jet algorithm for hadron collisions," *Phys.Rev.* **D48** (1993) 3160–3166, arXiv:hep-ph/9305266 [hep-ph].

[20] W. Giele and E. N. Glover, "Probabilistic jet algorithms," arXiv:hep-ph/9712355 [hep-ph].

[21] D. E. Soper and M. Spannowsky, "Combining subjet algorithms to enhance ZH detection at the LHC," *JHEP* **1008** (2010) 029, arXiv:1005.0417 [hep-ph].

[22] Y. Cui, Z. Han, and M. D. Schwartz, "W-jet Tagging: Optimizing the Identification of Boosted Hadronically-Decaying W Bosons," *Phys.Rev.* **D83** (2011) 074023, arXiv:1012.2077 [hep-ph].

[23] J. Gallicchio, J. Huth, M. Kagan, M. D. Schwartz, K. Black, *et al.*, "Multivariate discrimination and the Higgs + W/Z search," *JHEP* **1104** (2011) 069, arXiv:1010.3698 [hep-ph].

[24] D. E. Soper and M. Spannowsky, "Finding physics signals with shower deconstruction," *Phys.Rev.* **D84** (2011) 074002, arXiv:1102.3480 [hep-ph].

[25] D. E. Soper and M. Spannowsky, "Finding top quarks with shower deconstruction," arXiv:1211.3140 [hep-ph].

[26] M. Gouzevitch, A. Oliveira, J. Rojo, R. Rosenfeld, G. Salam, *et al.*, "Scale-invariant resonance tagging in multijet events and new physics in Higgs pair production," arXiv:1303.6636 [hep-ph].

[27] I. Volobouev, "Multiresolution jet reconstruction with FFTJet," *J.Phys.Conf.Ser.* **293** (2011) 012028.

[28] S. D. Ellis, C. K. Vermilion, and J. R. Walsh, "Recombination Algorithms and Jet Substructure: Pruning as a Tool for Heavy Particle Searches," *Phys.Rev.* **D81** (2010) 094023, arXiv:0912.0033 [hep-ph].

[29] J. Alwall, M. Herquet, F. Maltoni, O. Mattelaer, and T. Stelzer, "MadGraph 5 : Going Beyond," *JHEP* **1106** (2011) 128, arXiv:1106.0522 [hep-ph].

[30] T. Sjostrand, S. Mrenna, and P. Z. Skands, "PYTHIA 6.4 Physics and Manual," *JHEP* **0605** (2006) 026, arXiv:hep-ph/0603175 [hep-ph].

[31] M. Cacciari, G. P. Salam, and G. Soyez, "FastJet User Manual," *Eur.Phys.J.* **C72** (2012) 1896, arXiv:1111.6097 [hep-ph].

[32] M. Cacciari, G. P. Salam, and G. Soyez, "The Catchment Area of Jets," *JHEP* **0804** (2008) 005, arXiv:0802.1188 [hep-ph].

[33] S. D. Ellis, A. Hornig, T. S. Roy, D. Krohn, and M. D. Schwartz, "The Statistical Properties of Qjets," *In preparation* .

[34] J. M. Butterworth, A. R. Davison, M. Rubin, and G. P. Salam, "Jet substructure as a new Higgs search channel at the LHC," *Phys.Rev.Lett.* **100** (2008) 242001, arXiv:0802.2470 [hep-ph].

[35] **ATLAS Collaboration** Collaboration, G. Aad *et al.*, "Search for pair-produced massive coloured scalars in four-jet final states with the ATLAS detector in proton-proton collisions at $\sqrt{s} = 7$ TeV," arXiv:1210.4826 [hep-ex].

[36] **CMS Collaboration** Collaboration, S. Chatrchyan *et al.*, "Search for pair-produced dijet resonances in four-jet final states in pp collisions at sqrt(s) = 7 TeV," arXiv:1302.0531 [hep-ex].

[37] M. Cacciari and G. P. Salam, "Dispelling the N^3 myth for the k_t jet-finder," *Phys.Lett.* **B641** (2006) 57–61, arXiv:hep-ph/0512210 [hep-ph].

[38] Y.-T. Chien *In preparation* .

[39] D. E. Kaplan, K. Rehermann, M. D. Schwartz, and B. Tweedie, "Top Tagging: A Method for Identifying Boosted Hadronically Decaying Top Quarks," *Phys.Rev.Lett.* **101** (2008) 142001, arXiv:0806.0848 [hep-ph].

[40] T. Plehn, G. P. Salam, and M. Spannowsky, "Fat Jets for a Light Higgs," *Phys.Rev.Lett.* **104** (2010) 111801, arXiv:0910.5472 [hep-ph].

[41] J. Gallicchio and M. D. Schwartz, "Seeing in Color: Jet Superstructure," *Phys.Rev.Lett.* **105** (2010) 022001, arXiv:1001.5027 [hep-ph].

[42] A. Hook, M. Jankowiak, and J. G. Wacker, "Jet Dipolarity: Top Tagging with Color Flow," *JHEP* **1204** (2012) 007, arXiv:1102.1012 [hep-ph].

[43] J. Gallicchio and M. D. Schwartz, "Quark and Gluon Tagging at the LHC," *Phys.Rev.Lett.* **107** (2011) 172001, arXiv:1106.3076 [hep-ph].

[44] J. Gallicchio and M. D. Schwartz, "Quark and Gluon Jet Substructure," arXiv:1211.7038 [hep-ph].

[45] D. Krohn, L. Randall, and L.-T. Wang, "On the Feasibility and Utility of ISR Tagging," arXiv:1101.0810 [hep-ph].

[46] **CDF Collaboration** Collaboration CDF note 103098, http://www-cdf.fnal.gov/physics/new/top/2011/DilAfb/.

[47] **CDF Collaboration** Collaboration, T. Aaltonen *et al.*, "Evidence for a Mass Dependent Forward-Backward Asymmetry in Top Quark Pair Production," *Phys.Rev.D* (2011) , arXiv:1101.0034 [hep-ex].

[48] **CDF Collaboration** Collaboration, T. Aaltonen *et al.*, "Forward-Backward Asymmetry in Top Quark Production in ppbar Collisions at sqrts=1.96 TeV," *Phys.Rev.Lett.* **101** (2008) 202001, arXiv:0806.2472 [hep-ex].

[49] **D0 Collaboration** Collaboration, V. Abazov *et al.*, "First measurement of the forward-backward charge asymmetry in top quark pair production," *Phys.Rev.Lett.* **100** (2008) 142002, arXiv:0712.0851 [hep-ex].

[50] **D0 Collaboration** Collaboration, V. M. Abazov *et al.*, "Forward-backward asymmetry in top quark-antiquark production," arXiv:1107.4995 [hep-ex].

[51] "Measurement of the charge asymmetry in top quark pair production," Tech. Rep. CMS-PAS-TOP-11-014, CERN, Geneva, 2011.

[52] "Measurement of the charge asymmetry in top quark pair production in pp collisions at sqrts=7 tev using the atlas detector," Tech. Rep. ATLAS-CONF-2011-106, CERN, Geneva, Aug, 2011.

[53] Y. Bai, J. L. Hewett, J. Kaplan, and T. G. Rizzo, "LHC Predictions from a Tevatron Anomaly in the Top Quark Forward-Backward Asymmetry," *JHEP* **1103** (2011) 003, arXiv:1101.5203 [hep-ph].

[54] F. del Aguila, J. de Blas, P. Langacker, and M. Perez-Victoria, "Impact of extra particles on indirect Z' limits," arXiv:1104.5512 [hep-ph].

[55] G. F. Giudice, B. Gripaios, and R. Sundrum, "Flavourful Production at Hadron Colliders," arXiv:1105.3161 [hep-ph].

[56] A. Djouadi, G. Moreau, and F. Richard, "Forward-backward asymmetries of the bottom and top quarks in warped extra-dimensional models: LHC predictions from the LEP and Tevatron anomalies," arXiv:1105.3158 [hep-ph].

[57] R. Barcelo, A. Carmona, M. Masip, and J. Santiago, "Gluon excitations in t tbar production at hadron colliders," arXiv:1105.3333 [hep-ph].

[58] C.-H. Chen, S. S. Law, and R.-H. Li, "Rare B decays and Tevatron top-pair asymmetry," arXiv:1104.1497 [hep-ph].

[59] A. E. Nelson, T. Okui, and T. S. Roy, "A unified, flavor symmetric explanation for the t-tbar asymmetry and Wjj excess at CDF," arXiv:1104.2030 [hep-ph].

[60] X.-P. Wang, Y.-K. Wang, B. Xiao, J. Xu, and S.-h. Zhu, "New Color-Octet Vector Boson Revisit," arXiv:1104.1917 [hep-ph].

[61] C. Degrande, J.-M. Gerard, C. Grojean, F. Maltoni, and G. Servant, "An Effective approach to same sign top pair production at the LHC and the forward-backward asymmetry at the Tevatron," arXiv:1104.1798 [hep-ph].

[62] S. Jung, A. Pierce, and J. D. Wells, "Top quark asymmetry and dijet resonances," arXiv:1104.3139 [hep-ph].

[63] G. Zhu, "B physics constraints on a flavor symmetric scalar model to account for the ttbar asymmetry and Wjj excess at CDF," arXiv:1104.3227 [hep-ph].

[64] P. J. Fox, J. Liu, D. Tucker-Smith, and N. Weiner, "An Effective Z'," arXiv:1104.4127 [hep-ph].

[65] D.-W. Jung, P. Ko, and J. S. Lee, "A Possible Common Origin of the Top Forward-backward Asymmetry and the CDF Dijet Resonance," arXiv:1104.4443 [hep-ph].

[66] J. Shu, K. Wang, and G. Zhu, "A Revisit to Top Quark Forward-Backward Asymmetry," arXiv:1104.0083 [hep-ph].

[67] A. Rajaraman, Z. Surujon, and T. M. Tait, "Asymmetric Leptons for Asymmetric Tops," arXiv:1104.0947 [hep-ph].

[68] J. Aguilar-Saavedra and M. Perez-Victoria, "No like-sign tops at Tevatron: Constraints on extended models and implications for the t tbar asymmetry," arXiv:1104.1385 [hep-ph].

[69] M. R. Buckley, D. Hooper, J. Kopp, and E. Neil, "Light Z' Bosons at the Tevatron," arXiv:1103.6035 [hep-ph].

[70] S. Jung, A. Pierce, and J. D. Wells, "Top quark asymmetry from a non-Abelian horizontal symmetry," `arXiv:1103.4835 [hep-ph]`.

[71] S. Casagrande, "Indirect tests of the Randall-Sundrum model," `arXiv:1103.4131 [hep-ph]`.

[72] Z. Ligeti, M. Schmaltz, and G. M. Tavares, "Explaining the t tbar forward-backward asymmetry without dijet or flavor anomalies," `arXiv:1103.2757 [hep-ph]`.

[73] C. Grojean, E. Salvioni, and R. Torre, "A weakly constrained W' at the early LHC," `arXiv:1103.2761 [hep-ph]`.

[74] K. Blum, C. Delaunay, O. Gedalia, Y. Hochberg, S. J. Lee, *et al.*, "Implications of the CDF $t\bar{t} Forward - BackwardAsymmetryforBoostedTopPhysics,'' arXiv : 1102.3133[hep - ph]$.

[75] R. Foot, "Top quark forward-backward asymmetry from SU(N_c) color," `arXiv:1103.1940 [hep-ph]`.

[76] E. Barreto, Y. Coutinho, and J. Sa Borges, "Top quark forward-backward asymmetry from the $3-3-1$ model," *Phys.Rev.* **D83** (2011) 054006, `arXiv:1103.1266 [hep-ph]`.

[77] A. R. Zerwekh, "The Axigluon, a Four-Site Model and the Top Quark Forward-Backward Asymmetry at the Tevatron," `arXiv:1103.0956 [hep-ph]`.

[78] G. Isidori and J. F. Kamenik, "Forward-Backward t tbar Asymmetry from Anomalous Stop Pair Production," `arXiv:1103.0016 [hep-ph]`.

[79] K. M. Patel and P. Sharma, "Forward-backward asymmetry in top quark production from light colored scalars in SO(10) model," *JHEP* **1104** (2011) 085, `arXiv:1102.4736 [hep-ph]`.

[80] B. Grinstein, A. L. Kagan, M. Trott, and J. Zupan, "Forward-backward asymmetry in t anti-t production from flavour symmetries," `arXiv:1102.3374 [hep-ph]`.

[81] V. Barger, W.-Y. Keung, and C.-T. Yu, "Tevatron Asymmetry of Tops in a W',Z' Model," *Phys.Lett.* **B698** (2011) 243–250, `arXiv:1102.0279 [hep-ph]`.

[82] J. Shelton and K. M. Zurek, "A Theory for Maximal Flavor Violation," `arXiv:1101.5392 [hep-ph]`.

[83] C. Delaunay, O. Gedalia, S. J. Lee, G. Perez, and E. Ponton, "Extraordinary Phenomenology from Warped Flavor Triviality," `arXiv:1101.2902 [hep-ph]`.

[84] K. Cheung and T.-C. Yuan, "Top Quark Forward-Backward Asymmetry in the Large Invariant Mass Region," *Phys. Rev.* **D83** (2011) 074006, arXiv:1101.1445 [hep-ph].

[85] Y. Cui, Z. Han, and M. D. Schwartz, "Top condensation as a motivated explanation of the top forward-backward asymmetry," arXiv:1106.3086 [hep-ph].

[86] G. M. Tavares and M. Schmaltz, "Explaining the t-tbar asymmetry with a light axigluon," arXiv:1107.0978 [hep-ph].

[87] J. Aguilar-Saavedra and M. Perez-Victoria, "Shaping the top asymmetry," arXiv:1107.2120 [hep-ph].

[88] J. F. Kamenik, J. Shu, and J. Zupan, "Review of new physics effects in t-tbar production," arXiv:1107.5257 [hep-ph].

[89] CMS Collaboration, "Search for Same-Sign Top-Quark Pair Production at sqrt(s) = 7 TeV and Limits on Flavour Changing Neutral Currents in the Top Sector," arXiv:1106.2142 [hep-ex].

[90] M. I. Gresham, I.-W. Kim, and K. M. Zurek, "On Models of New Physics for the Tevatron Top A_{FB}," arXiv:1103.3501 [hep-ph].

[91] M. I. Gresham, I.-W. Kim, and K. M. Zurek, "Tevatron Top A_{FB} Versus LHC Top Physics," arXiv:1107.4364 [hep-ph].

[92] Y.-k. Wang, B. Xiao, and S.-h. Zhu, "One-side Forward-backward Asymmetry in Top Quark Pair Production at CERN Large Hadron Collider," *Phys.Rev.* **D82** (2010) 094011, arXiv:1008.2685 [hep-ph].

[93] J. L. Hewett, J. Shelton, M. Spannowsky, T. M. Tait, and M. Takeuchi, "A^t_{FB} Meets LHC," arXiv:1103.4618 [hep-ph].

[94] B. Xiao, Y.-K. Wang, Z.-Q. Zhou, and S.-h. Zhu, "Edge Charge Asymmetry in Top Pair Production at the LHC," arXiv:1101.2507 [hep-ph].

[95] B. Bhattacherjee, S. S. Biswal, and D. Ghosh, "Top quark forward-backward asymmetry at Tevatron and its implications at the LHC," arXiv:1102.0545 [hep-ph].

[96] J. Aguilar-Saavedra and M. Perez-Victoria, "Asymmetries in t tbar production: LHC versus Tevatron," arXiv:1105.4606 [hep-ph].

[97] E. L. Berger, Q.-H. Cao, C.-R. Chen, and H. Zhang, "Top Quark Polarization As A Probe of Models with Extra Gauge Bosons," arXiv:1103.3274 [hep-ph].

[98] R. M. Godbole, K. Rao, S. D. Rindani, and R. K. Singh, "On measurement of top polarization as a probe of $t\bar{t}$ production mechanisms at the LHC," *JHEP* **1011** (2010) 144, arXiv:1010.1458 [hep-ph].

[99] J. Cao, L. Wu, and J. M. Yang, "New physics effects on top quark spin correlation and polarization at the LHC: a comparative study in different models," arXiv:1011.5564 [hep-ph].

[100] D.-W. Jung, P. Ko, and J. S. Lee, "Longitudinal top polarization as a probe of a possible origin of forward-backward asymmetry of the top quark at the Tevatron," arXiv:1011.5976 [hep-ph].

[101] D. Choudhury, R. M. Godbole, S. D. Rindani, and P. Saha, "Top polarization, forward-backward asymmetry and new physics," arXiv:1012.4750 [hep-ph].

[102] W. Bernreuther and Z.-G. Si, "Distributions and correlations for top quark pair production and decay at the Tevatron and LHC.," *Nucl.Phys.* **B837** (2010) 90–121, arXiv:1003.3926 [hep-ph].

[103] K. Melnikov and M. Schulze, "NLO QCD corrections to top quark pair production and decay at hadron colliders," *JHEP* **0908** (2009) 049, arXiv:0907.3090 [hep-ph].

[104] D. Krohn, T. Liu, J. Shelton, and L.-T. Wang, "A Polarized View of the Top Asymmetry," arXiv:1105.3743 [hep-ph].

[105] Y. Bai and Z. Han, "Improving the Top Quark Forward-Backward Asymmetry Measurement at the LHC," arXiv:1106.5071 [hep-ph].

[106] M. I. Gresham, I.-W. Kim, and K. M. Zurek, "Searching for Top Flavor Violating Resonances," arXiv:1102.0018 [hep-ph].

[107] N. Craig, C. Kilic, and M. J. Strassler, "LHC Charge Asymmetry as Constraint on Models for the Tevatron Top Anomaly," arXiv:1103.2127 [hep-ph].

[108] J. Cao, L. Wang, L. Wu, and J. M. Yang, "Top quark forward-backward asymmetry, FCNC decays and like-sign pair production as a joint probe of new physics," arXiv:1101.4456 [hep-ph].

[109] E. Alvarez, L. Da Rold, J. I. S. Vietto, and A. Szynkman, "Phenomenology of a light gluon resonance in top-physics at Tevatron and LHC," arXiv:1107.1473 [hep-ph].

[110] E. L. Berger, Q.-H. Cao, C.-R. Chen, C. S. Li, and H. Zhang, "Top Quark Forward-Backward Asymmetry and Same-Sign Top Quark Pairs," *Phys.Rev.Lett.* **106** (2011) 201801, arXiv:1101.5625 [hep-ph].

[111] M. J. Strassler, "A Note on Measuring Charm and Bottom Forward-Backward Asymmetries at the Tevatron," `arXiv:1102.0736 [hep-ph]`.

[112] L. Sehgal and M. Wanninger, "FORWARD - BACKWARD ASYMMETRY IN TWO JET EVENTS: SIGNATURE OF AXIGLUONS IN PROTON - ANTI-PROTON COLLISIONS," *Phys.Lett.* **B200** (1988) 211.

[113] J. Alwall *et al.*, "MadGraph/MadEvent v4: The New Web Generation," *JHEP* **09** (2007) 028, `arXiv:0706.2334 [hep-ph]`.

[114] J. Pumplin *et al.*, "New generation of parton distributions with uncertainties from global QCD analysis," *JHEP* **07** (2002) 012, `arXiv:hep-ph/0201195`.

[115] J. H. Kuhn and G. Rodrigo, "Charge asymmetry in hadroproduction of heavy quarks," *Phys.Rev.Lett.* **81** (1998) 49–52, `arXiv:hep-ph/9802268 [hep-ph]`.

[116] M. Cacciari, G. Salam, and G. Soyez, "FastJet." http://fastjet.fr/.

[117] **The ATLAS Collaboration** Collaboration, G. Aad *et al.*, "Expected Performance of the ATLAS Experiment - Detector, Trigger and Physics," `arXiv:0901.0512 [hep-ex]`.

[118] S. Weinberg, "Implications of Dynamical Symmetry Breaking," *Phys. Rev.* **D13** (1976) 974–996.

[119] S. Weinberg, "Implications of Dynamical Symmetry Breaking: An Addendum," *Phys. Rev.* **D19** (1979) 1277–1280.

[120] L. Susskind, "Dynamics of Spontaneous Symmetry Breaking in the Weinberg- Salam Theory," *Phys. Rev.* **D20** (1979) 2619–2625.

[121] G. 't Hooft, (ed.) *et al.*, "Recent developments in gauge theories. proceedings, nato advanced study institute, cargese, france, august 26 - september 8, 1979," *Nato Advanced Study Institutes Series: Series B* (1979) .

[122] M. Weinstein, "CONSERVED CURRENTS, THEIR COMMUTATORS AND THE SYMMETRY STRUCTURE OF RENORMALIZABLE THEORIES OF ELECTROMAGNETIC, WEAK AND STRONG INTERACTIONS," *Phys. Rev.* **D8** (1973) 2511.

[123] J. Wess and B. Zumino, "Supergauge Transformations in Four-Dimensions," *Nucl. Phys.* **B70** (1974) 39–50.

[124] I. Antoniadis, "A Possible new dimension at a few TeV," *Phys. Lett.* **B246** (1990) 377–384.

[125] I. Antoniadis and K. Benakli, "Limits on extra dimensions in orbifold compactifications of superstrings," *Phys. Lett.* **B326** (1994) 69–78, arXiv:hep-th/9310151.

[126] N. Arkani-Hamed, S. Dimopoulos, and G. R. Dvali, "Phenomenology, astrophysics and cosmology of theories with sub-millimeter dimensions and TeV scale quantum gravity," *Phys. Rev.* **D59** (1999) 086004, arXiv:hep-ph/9807344.

[127] N. Arkani-Hamed, S. Dimopoulos, and G. R. Dvali, "The hierarchy problem and new dimensions at a millimeter," *Phys. Lett.* **B429** (1998) 263–272, arXiv:hep-ph/9803315.

[128] I. Antoniadis, N. Arkani-Hamed, S. Dimopoulos, and G. R. Dvali, "New dimensions at a millimeter to a Fermi and superstrings at a TeV," *Phys. Lett.* **B436** (1998) 257–263, arXiv:hep-ph/9804398.

[129] L. Randall and R. Sundrum, "A large mass hierarchy from a small extra dimension," *Phys. Rev. Lett.* **83** (1999) 3370–3373, arXiv:hep-ph/9905221.

[130] L. Randall and R. Sundrum, "An alternative to compactification," *Phys. Rev. Lett.* **83** (1999) 4690–4693, arXiv:hep-th/9906064.

[131] T. Appelquist, H.-C. Cheng, and B. A. Dobrescu, "Bounds on universal extra dimensions," *Phys. Rev.* **D64** (2001) 035002, arXiv:hep-ph/0012100.

[132] T. Appelquist and H.-U. Yee, "Universal extra dimensions and the Higgs boson mass," *Phys. Rev.* **D67** (2003) 055002, arXiv:hep-ph/0211023.

[133] H.-C. Cheng, K. T. Matchev, and M. Schmaltz, "Radiative corrections to Kaluza-Klein masses," *Phys. Rev.* **D66** (2002) 036005, arXiv:hep-ph/0204342.

[134] C. Macesanu, C. D. McMullen, and S. Nandi, "Collider implications of universal extra dimensions," *Phys. Rev.* **D66** (2002) 015009, arXiv:hep-ph/0201300.

[135] J. L. Feng, A. Rajaraman, and F. Takayama, "Graviton cosmology in universal extra dimensions," *Phys. Rev.* **D68** (2003) 085018, arXiv:hep-ph/0307375.

[136] N. R. Shah and C. E. M. Wagner, "Gravitons and Dark Matter in Universal Extra Dimensions," *Phys. Rev.* **D74** (2006) 104008, arXiv:hep-ph/0608140.

[137] W. D. Goldberger, Y. Nomura, and D. Tucker-Smith, "Warped supersymmetric grand unification," *Phys. Rev.* **D67** (2003) 075021, arXiv:hep-ph/0209158.

[138] Y. Nomura and D. Tucker-Smith, "Spectrum of TeV particles in warped supersymmetric grand unification," *Phys. Rev.* **D68** (2003) 075003, arXiv:hep-ph/0305214.

[139] Y. Nomura, D. Tucker-Smith, and B. Tweedie, "Warped supersymmetric unification with non-unified superparticle spectrum," *Phys. Rev.* **D71** (2005) 075004, arXiv:hep-ph/0403170.

[140] Y. Nomura and D. Tucker-Smith, "Matter unification in warped supersymmetric SO(10)," *Nucl. Phys.* **B698** (2004) 92–110, arXiv:hep-ph/0403171.

[141] C. Friberg, E. Norrbin, and T. Sjostrand, "QCD aspects of leptoquark production at HERA," *Phys. Lett.* **B403** (1997) 329–334, arXiv:hep-ph/9704214.

[142] P. Fishbane, S. Meshkov, and P. Ramond, "STANDARD MODEL CONSTRAINTS ON FERMIONS," *Phys. Lett.* **B134** (1984) 81.

[143] P. M. Fishbane, S. Meshkov, R. E. Norton, and P. Ramond, "CHIRAL FERMIONS BEYOND THE STANDARD MODEL," *Phys. Rev.* **D31** (1985) 1119.

[144] R. Barbieri, T. Gregoire, and L. J. Hall, "Mirror world at the Large Hadron Collider," arXiv:hep-ph/0509242.

[145] H.-J. He, N. Polonsky, and S.-f. Su, "Extra families, Higgs spectrum and oblique corrections," *Phys. Rev.* **D64** (2001) 053004, arXiv:hep-ph/0102144.

[146] T. Banks and M. Karliner, "PRODUCTION OF MIRROR FERMIONS NEAR THE Z0 PEAK," *Nucl. Phys.* **B281** (1987) 399.

[147] N. Polonsky and S.-f. Su, "Low-energy limits of theories with two supersymmetries," *Phys. Rev.* **D63** (2001) 035007, arXiv:hep-ph/0006174.

[148] D. G. E. Walker, "Dark Matter Stabilization Symmetries and Long-Lived Particles at the Large Hadron Collider," arXiv:0907.3142 [hep-ph].

[149] M. Fairbairn *et al.*, "Stable massive particles at colliders," *Phys. Rept.* **438** (2007) 1–63, arXiv:hep-ph/0611040.

[150] M. Drees and X. Tata, "Signals for heavy exotics at hadron colliders and supercolliders," *Phys. Lett.* **B252** (1990) 695–702.

[151] A. Arvanitaki, S. Dimopoulos, A. Pierce, S. Rajendran, and J. G. Wacker, "Stopping gluinos," *Phys. Rev.* **D76** (2007) 055007, arXiv:hep-ph/0506242.

[152] **D0** Collaboration, V. M. Abazov *et al.*, "Search for stopped gluinos from $p\overline{p}$ collisions at $\sqrt{s} = 1.96$-TeV," *Phys. Rev. Lett.* **99** (2007) 131801, arXiv:0705.0306 [hep-ex].

[153] **CMS** Collaboration, M. Kazana, "Search for heavy stable charged particles in CMS," *PoS* **EPS-HEP2009** (2009) 438.

[154] ATLAS-CONF-2010-071, "Background studies to searches for long-lived stopped particles decaying out-of-time with lhc collisions.," 2010.

[155] W. Kilian, T. Plehn, P. Richardson, and E. Schmidt, "Split supersymmetry at colliders," *Eur. Phys. J.* **C39** (2005) 229–243, arXiv:hep-ph/0408088.

[156] H. Baer, K.-m. Cheung, and J. F. Gunion, "A Heavy gluino as the lightest supersymmetric particle," *Phys. Rev.* **D59** (1999) 075002, arXiv:hep-ph/9806361.

[157] A. Mafi and S. Raby, "An analysis of a Heavy Gluino LSP at CDF : The Heavy Gluino Window," *Phys. Rev.* **D62** (2000) 035003, arXiv:hep-ph/9912436.

[158] A. Mafi and S. Raby, "A solution to the mu problem in the presence of a heavy gluino LSP," *Phys. Rev.* **D63** (2001) 055010, arXiv:hep-ph/0009202.

[159] S. Raby, "Gauge-mediated SUSY breaking with a gluino LSP," *Phys. Lett.* **B422** (1998) 158–162, arXiv:hep-ph/9712254.

[160] S. Raby, "Gauge mediated SUSY breaking at an intermediate scale," *Phys. Rev.* **D56** (1997) 2852–2860, arXiv:hep-ph/9702299.

[161] H. K. Dreiner, "An introduction to explicit R-parity violation," arXiv:hep-ph/9707435.

[162] E. L. Berger and Z. Sullivan, "Lower limits on R parity violating couplings in supersymmetry," *Phys. Rev. Lett.* **92** (2004) 201801, arXiv:hep-ph/0310001.

[163] G. R. Farrar and P. Fayet, "Bounds on r Hadron Production from Calorimetry Experiments," *Phys. Lett.* **B79** (1978) 442.

[164] G. R. Farrar and P. Fayet, "Phenomenology of the Production, Decay, and Detection of New Hadronic States Associated with Supersymmetry," *Phys. Lett.* **B76** (1978) 575–579.

[165] **ALEPH** Collaboration, A. Heister *et al.*, "Search for scalar quarks in e^+e^- collisions at $\sqrt{s}$ up to 209-GeV," *Phys. Lett.* **B537** (2002) 5–20, arXiv:hep-ex/0204036.

[166] **CDF** Collaboration, D. E. Acosta *et al.*, "Search for the supersymmetric partner of the top quark in dilepton events from $p\overline{p}$ collisions at $\sqrt{s} = 1.8$ TeV," *Phys. Rev. Lett.* **90** (2003) 251801, arXiv:hep-ex/0302009.

[167] ALEPH, DELPHI, L3, and OPAL, "LEP2 SUSY Working Group," 2002.

[168] **ATLAS** Collaboration, P. Mermod, "Discovery Potential of R-hadrons with the ATLAS Detector at the LHC," *AIP Conf. Proc.* **1200** (2010) 750–753, arXiv:0909.1911 [hep-ex].

[169] P. F. Smith *et al.*, "A SEARCH FOR ANOMALOUS HYDROGEN IN ENRICHED D-2 O, USING A TIME-OF-FLIGHT SPECTROMETER," *Nucl. Phys.* **B206** (1982) 333–348.

[170] A. Arvanitaki, C. Davis, P. W. Graham, A. Pierce, and J. G. Wacker, "Limits on split supersymmetry from gluino cosmology," *Phys. Rev.* **D72** (2005) 075011, arXiv:hep-ph/0504210.

[171] M. Kawasaki, K. Kohri, and T. Moroi, "Big-bang nucleosynthesis and hadronic decay of long-lived massive particles," *Phys. Rev.* **D71** (2005) 083502, arXiv:astro-ph/0408426.

[172] **EGRET** Collaboration, P. Sreekumar *et al.*, "EGRET observations of the extragalactic gamma ray emission," *Astrophys. J.* **494** (1998) 523–534, arXiv:astro-ph/9709257.

[173] A. J. Barr, "Using lepton charge asymmetry to investigate the spin of supersymmetric particles at the LHC," *Phys. Lett.* **B596** (2004) 205–212, arXiv:hep-ph/0405052.

[174] A. J. Barr, "Measuring slepton spin at the LHC," *JHEP* **02** (2006) 042, arXiv:hep-ph/0511115.

[175] M. Battaglia, A. Datta, A. De Roeck, K. Kong, and K. T. Matchev, "Contrasting supersymmetry and universal extra dimensions at the CLIC multi-TeV e+ e- collider," *JHEP* **07** (2005) 033, arXiv:hep-ph/0502041.

[176] J. M. Smillie and B. R. Webber, "Distinguishing Spins in Supersymmetric and Universal Extra Dimension Models at the Large Hadron Collider," *JHEP* **10** (2005) 069, arXiv:hep-ph/0507170.

[177] L.-T. Wang and I. Yavin, "Spin Measurements in Cascade Decays at the LHC," *JHEP* **04** (2007) 032, arXiv:hep-ph/0605296.

[178] A. Alves and O. Eboli, "Unravelling the sbottom spin at the CERN LHC," *Phys. Rev.* **D75** (2007) 115013, arXiv:0704.0254 [hep-ph].

[179] M. R. Buckley, H. Murayama, W. Klemm, and V. Rentala, "Discriminating spin through quantum interference," *Phys. Rev.* **D78** (2008) 014028, arXiv:0711.0364 [hep-ph].

[180] M. R. Buckley, S. Y. Choi, K. Mawatari, and H. Murayama, "Determining Spin through Quantum Azimuthal-Angle Correlations," *Phys. Lett.* **B672** (2009) 275–279, arXiv:0811.3030 [hep-ph].

[181] M. R. Buckley, B. Heinemann, W. Klemm, and H. Murayama, "Quantum Interference Effects Among Helicities at LEP-II and Tevatron," *Phys. Rev.* **D77** (2008) 113017, arXiv:0804.0476 [hep-ph].

[182] H. Murayama and V. Rentala, "Randall-Sundrum graviton spin determination using azimuthal angular dependence," arXiv:0904.4561 [hep-ph].

[183] B. C. Allanach, C. M. Harris, M. A. Parker, P. Richardson, and B. R. Webber, "Detecting exotic heavy leptons at the Large Hadron Collider," *JHEP* **08** (2001) 051, arXiv:hep-ph/0108097.

[184] S. Kuhlmann, "CTEQ5 parton distributions and ongoing studies," *Nucl. Phys. Proc. Suppl.* **79** (1999) 108–110.

[185] D. Milstead, "Scattering of Heavy Stable Exotic Hadrons," arXiv:0909.2563 [hep-ph].

[186] A. C. Kraan, "Interactions of heavy stable hadronizing particles," *Eur. Phys. J.* **C37** (2004) 91–104, arXiv:hep-ex/0404001.

[187] R. Mackeprang and A. Rizzi, "Interactions of coloured heavy stable particles in matter," *Eur. Phys. J.* **C50** (2007) 353–362, arXiv:hep-ph/0612161.

[188] Y. R. de Boer, A. B. Kaidalov, D. A. Milstead, and O. I. Piskounova, "Interactions of Heavy Hadrons using Regge Phenomenology and the Quark Gluon String Model," *J. Phys.* **G35** (2008) 075009, arXiv:0710.3930 [hep-ph].

[189] **GEANT4** Collaboration, S. Agostinelli *et al.*, "GEANT4: A simulation toolkit," *Nucl. Instrum. Meth.* **A506** (2003) 250–303.

[190] R. Mackeprang and D. Milstead, "An Updated Description of Heavy-Hadron Interactions," *Eur. Phys. J.* **C66** (2010) 493–501, arXiv:0908.1868 [hep-ph].

[191] R. Mackeprang, "Signatures of long-lived colored sparticles," *AIP Conf. Proc.* **1200** (2010) 746–749, arXiv:0909.5104 [hep-ph].

[192] M. S. Chanowitz and S. R. Sharpe, "SPECTRUM OF GLUINO BOUND STATES," *Phys. Lett.* **B126** (1983) 225.

[193] F. Buccella, G. R. Farrar, and A. Pugliese, "R BARYON MASSES," *Phys. Lett.* **B153** (1985) 311.

[194] **UKQCD** Collaboration, M. Foster and C. Michael, "The mass spectrum of a static adjoint particle," *Nucl. Phys. Proc. Suppl.* **63** (1998) 724–726, arXiv:hep-lat/9709051.

[195] **UKQCD** Collaboration, M. Foster and C. Michael, "Hadrons with a heavy colour-adjoint particle," *Phys. Rev.* **D59** (1999) 094509, arXiv:hep-lat/9811010.

[196] S. J. Gates, Jr. and O. Lebedev, "Searching for supersymmetry in hadrons," *Phys. Lett.* **B477** (2000) 216–222, arXiv:hep-ph/9912362.

[197] A. Datta, K. Kong, and K. T. Matchev, "Discrimination of supersymmetry and universal extra dimensions at hadron colliders," *Phys. Rev.* **D72** (2005) 096006, arXiv:hep-ph/0509246. Erratum *ibid.* **D72** (2005) 119901.

[198] A. Alves, O. Eboli, and T. Plehn, "It's a gluino," *Phys. Rev.* **D74** (2006) 095010, arXiv:hep-ph/0605067.

[199] C. Athanasiou, C. G. Lester, J. M. Smillie, and B. R. Webber, "Distinguishing spins in decay chains at the Large Hadron Collider," *JHEP* **08** (2006) 055, arXiv:hep-ph/0605286.

[200] C. Athanasiou, C. G. Lester, J. M. Smillie, and B. R. Webber, "Addendum to 'Distinguishing spins in decay chains at the Large Hadron Collider'," arXiv:hep-ph/0606212.

[201] C. Kilic, L.-T. Wang, and I. Yavin, "On the existence of angular correlations in decays with heavy matter partners," *JHEP* **05** (2007) 052, arXiv:hep-ph/0703085.

[202] C. Csáki, J. Heinonen, and M. Perelstein, "Testing gluino spin with three-body decays," *JHEP* **10** (2007) 107, arXiv:0707.0014 [hep-ph].

[203] M. Burns, K. Kong, K. T. Matchev, and M. Park, "A general method for model-independent measurements of particle spins, couplings and mixing angles in cascade decays with missing energy at hadron colliders," *JHEP* **10** (2008) 081, arXiv:0808.2472 [hep-ph].

[204] O. Gedalia, S. J. Lee, and G. Perez, "Spin determination via third generation cascade decays," *Phys. Rev.* **D80** (2009) 035012, arXiv:0901.4438 [hep-ph].

[205] H.-C. Cheng, Z. Han, I.-W. Kim, and L.-T. Wang, "Missing momentum reconstruction and spin measurements at hadron colliders," *JHEP* **11** (2010) 122, arXiv:1008.0405 [hep-ph].

[206] G. Moortgat-Pick, K. Rolbiecki, and J. Tattersall, "Early spin determination at the LHC?," *Phys.Lett.* **B699** (2011) 158, arXiv:1102.0293 [hep-ph].

[207] Y. Kats and M. D. Schwartz, "Annihilation decays of bound states at the LHC," *JHEP* **04** (2010) 016, arXiv:0912.0526 [hep-ph].

[208] C. D. Carone, J. M. Conroy, M. Sher, and I. Turan, "Universal extra dimensions and Kaluza-Klein bound states," *Phys. Rev.* **D69** (2004) 074018, arXiv:hep-ph/0312055.

[209] N. Fabiano and O. Panella, "Threshold production of metastable bound states of Kaluza Klein excitations in universal extra dimensions," *Phys. Rev.* **D81** (2010) 115001, arXiv:0804.3917 [hep-ph].

[210] D. Hooper and S. Profumo, "Dark matter and collider phenomenology of universal extra dimensions," *Phys. Rept.* **453** (2007) 29, arXiv:hep-ph/0701197.

[211] H.-C. Cheng, K. T. Matchev, and M. Schmaltz, "Bosonic supersymmetry? Getting fooled at the CERN LHC," *Phys. Rev.* **D66** (2002) 056006, arXiv:hep-ph/0205314.

[212] G. Servant and T. M. P. Tait, "Is the lightest Kaluza-Klein particle a viable dark matter candidate?," *Nucl. Phys.* **B650** (2003) 391, arXiv:hep-ph/0206071.

[213] H.-C. Cheng, J. L. Feng, and K. T. Matchev, "Kaluza-Klein dark matter," *Phys. Rev. Lett.* **89** (2002) 211301, arXiv:hep-ph/0207125.

[214] H. Georgi, A. K. Grant, and G. Hailu, "Brane couplings from bulk loops," *Phys. Lett.* **B506** (2001) 207, arXiv:hep-ph/0012379.

[215] M. S. Carena, T. M. P. Tait, and C. E. M. Wagner, "Branes and orbifolds are opaque," *Acta Phys. Polon.* **B33** (2002) 2355, arXiv:hep-ph/0207056.

[216] T. Flacke, A. Menon, and D. J. Phalen, "Non-minimal universal extra dimensions," *Phys. Rev.* **D79** (2009) 056009, arXiv:0811.1598 [hep-ph].

[217] S. P. Martin, "Diphoton decays of stoponium at the Large Hadron Collider," *Phys. Rev.* **D77** (2008) 075002, arXiv:0801.0237 [hep-ph].

[218] E. De Pree and M. Sher, "Kaluza-Klein mesons in universal extra dimensions," *Phys. Rev.* **D72** (2005) 097701, arXiv:hep-ph/0507313.

[219] M. Beneke, P. Falgari, and C. Schwinn, "Soft radiation in heavy-particle pair production: all-order colour structure and two-loop anomalous dimension," *Nucl. Phys.* **B828** (2010) 69, arXiv:0907.1443 [hep-ph].

[220] M. E. Peskin and D. V. Schroeder, *An Introduction to Quantum Field Theory.* Westview Press, 1995. See Section 5.3.

[221] V. A. Novikov *et al.*, "Charmonium and gluons," *Phys. Rept.* **41** (1978) 1.

[222] I. V. Tyutin and B. B. Lokhvitskii, "Charge conjugation of non-Abelian gauge fields," *Sov. Phys. J.* **25** (1982) 346. [Izv. Vys. Uch. Zav. Fiz. **4** (1982) 62].

[223] N. V. Smolyakov, "Furry theorem for non-abelian gauge Lagrangians," *Theor. Math. Phys.* **50** (1982) 225. [Teor. Mat. Fiz. **50** (1982) 344].

[224] C. P. Burgess and G. D. Moore, *The Standard Model: A Primer*. Cambridge University Press, 2007.

[225] J. T. Goldman and H. Haber, "Gluinonium: The hydrogen atom of supersymmetry," *Physica* **15D** (1985) 181.

[226] W.-Y. Keung and A. Khare, "Two-gluino bound states," *Phys. Rev.* **D29** (1984) 2657.

[227] M. R. Kauth, J. H. Kühn, P. Marquard, and M. Steinhauser, "Gluinonia: Energy levels, production and decay," *Nucl. Phys.* **B831** (2010) 285, `arXiv:0910.2612 [hep-ph]`.

[228] A. D. Martin, W. J. Stirling, R. S. Thorne, and G. Watt, "Parton distributions for the LHC," *Eur. Phys. J.* **C63** (2009) 189, `arXiv:0901.0002 [hep-ph]`.

[229] C. Kim and T. Mehen, "Color octet scalar bound states at the LHC," *Phys. Rev.* **D79** (2009) 035011, `arXiv:0812.0307 [hep-ph]`.

[230] K. Hagiwara and H. Yokoya, "Bound-state effects on gluino-pair production at hadron colliders," *JHEP* **10** (2009) 049, `arXiv:0909.3204 [hep-ph]`.

[231] V. D. Barger and A. D. Martin, "Quarkonium production at $p\overline{p}$ colliders," *Phys. Rev.* **D31** (1985) 1051.

[232] V. D. Barger *et al.*, "Superheavy quarkonium production and decays: A new Higgs signal," *Phys. Rev.* **D35** (1987) 3366. Erratum *ibid.* **D38** (1988) 1632.

[233] E. Arik, O. Çakır, S. A. Çetin, and S. Sultansoy, "Fourth generation pseudoscalar quarkonium production and observability at hadron colliders," *Phys. Rev.* **D66** (2002) 116006, `arXiv:hep-ph/0208169`.

[234] S. P. Martin and J. E. Younkin, "Radiative corrections to stoponium annihilation decays," *Phys. Rev.* **D80** (2009) 035026, `arXiv:0901.4318 [hep-ph]`.

[235] J. E. Younkin and S. P. Martin, "QCD corrections to stoponium production at hadron colliders," *Phys. Rev.* **D81** (2010) 055006, `arXiv:0912.4813 [hep-ph]`.

[236] M. Herrero, A. Méndez, and T. Rizzo, "Production of heavy squarkonium at high energy pp colliders," *Phys.Lett.* **B200** (1988) 205.

[237] V. D. Barger and W.-Y. Keung, "Stoponium decays to Higgs bosons," *Phys.Lett.* **B211** (1988) 355.

[238] M. Drees and M. M. Nojiri, "Production and decay of scalar top squarkonium bound states," *Phys.Rev.* **D49** (1994) 4595, arXiv:hep-ph/9312213.

[239] G. V. Borisov, Y. F. Pirogov, and K. R. Rudakov, "Pair production of exotic particles at $(\overline{p})p$ colliding beams," *Z. Phys.* **C36** (1987) 217.

[240] E. Chikovani, V. Kartvelishvili, R. Shanidze, and G. Shaw, "Bound states of two gluinos at the Tevatron and CERN LHC," *Phys. Rev.* **D53** (1996) 6653, arXiv:hep-ph/9602249.

[241] K. Cheung and W.-Y. Keung, "Split supersymmetry, stable gluino, and gluinonium," *Phys. Rev.* **D71** (2005) 015015, arXiv:hep-ph/0408335.

[242] E. Bouhova-Thacker, V. Kartvelishvili, and A. Small, "Search for gluino-gluino bound states," *Nucl. Phys. Proc. Suppl.* **133** (2004) 122.

[243] E. Bouhova-Thacker, V. Kartvelishvili, and A. Small, "Search for gluino-gluino bound states with ATLAS," *Nucl. Phys. Proc. Suppl.* **152** (2006) 300.

[244] M. Drees and M. M. Nojiri, "Proposed new signal for scalar top-squark bound-state production," *Phys.Rev.Lett.* **72** (1994) 2324, arXiv:hep-ph/9310209.

[245] C. Lin, "A search for universal extra dimensions in the multi-lepton channel from $p\overline{p}$ collisions at $\sqrt{s} = 1.8$ TeV,". FERMILAB-THESIS-2005-69.

[246] U. Haisch and A. Weiler, "Bound on minimal universal extra dimensions from $\overline{B} \to X_s\gamma$," *Phys. Rev.* **D76** (2007) 034014, arXiv:hep-ph/0703064.

[247] I. Gogoladze and C. Macesanu, "Precision electroweak constraints on universal extra dimensions revisited," *Phys. Rev.* **D74** (2006) 093012, arXiv:hep-ph/0605207.

[248] J. L. Feng, J.-F. Grivaz, and J. Nachtman, "Searches for supersymmetry at high-energy colliders," *Rev. Mod. Phys.* **82** (2010) 699, arXiv:0903.0046 [hep-ex].

[249] **CMS** Collaboration, "Search for supersymmetry in pp collisions at 7 TeV in events with jets and missing transverse energy," *Phys.Lett.* **B698** (2011) 196, arXiv:1101.1628 [hep-ex].

[250] **ATLAS** Collaboration, "Search for supersymmetry using final states with one lepton, jets, and missing transverse momentum with the ATLAS detector in $\sqrt{s} = 7$ TeV pp collisions," arXiv:1102.2357 [hep-ex].

[251] **ATLAS** Collaboration, "Search for squarks and gluinos using final states with jets and missing transverse momentum with the ATLAS detector in $\sqrt{s} = 7$ TeV proton-proton collisions," arXiv:1102.5290 [hep-ex].

[252] **CMS** Collaboration, "Search for supersymmetry in pp collisions at $\sqrt{s} = 7$ TeV in events with two photons and missing transverse energy," `arXiv:1103.0953 [hep-ex]`.

[253] **CMS** Collaboration, "Search for physics beyond the Standard Model in opposite-sign dilepton events at $\sqrt{s} = 7$ TeV," `arXiv:1103.1348 [hep-ex]`.

[254] **ATLAS** Collaboration, "Search for stable hadronising squarks and gluinos with the ATLAS experiment at the LHC," `arXiv:1103.1984 [hep-ex]`.

[255] J. Alwall, M.-P. Le, M. Lisanti, and J. G. Wacker, "Searching for directly decaying gluinos at the Tevatron," *Phys. Lett.* **B666** (2008) 34, `arXiv:0803.0019 [hep-ph]`.

[256] T. Sjöstrand, S. Mrenna, and P. Skands, "A Brief Introduction to PYTHIA 8.1," *Comput. Phys. Commun.* **178** (2008) 852, `arXiv:0710.3820 [hep-ph]`.
See also http://home.thep.lu.se/ torbjorn/Pythia.html.

[257] G. P. Salam and G. Soyez, "A Practical Seedless Infrared-Safe Cone jet algorithm," *JHEP* **0705** (2007) 086, `arXiv:0704.0292 [hep-ph]`.

[258] **ATLAS** Collaboration, G. Aad *et al.*, "Performance of the ATLAS b-tagging algorithms,". ATL-PHYS-PUB-2009-018 (2009).

[259] **CMS** Collaboration, "Algorithms for b jet identification in CMS,". CMS PAS BTV-09-001 (2009).

[260] **CMS** Collaboration, "Search for Randall-Sundrum gravitons decaying into two photons in 7 TeV pp collisions with the CMS detector,". CMS PAS EXO-10-019 (2011).

[261] D. A. Dicus, C. D. McMullen, and S. Nandi, "Collider implications of Kaluza-Klein excitations of the gluons," *Phys. Rev.* **D65** (2002) 076007, `arXiv:hep-ph/0012259`.